Solvothermal Synthesis of Porous Nanomaterials with Precisely Controlled Crystal Structure

Yoshitaka KUMABE

Student ID Number: 1226001

A dissertation submitted to the Engineering Course,

Department of Engineering, Graduate School of Engineering,

Kochi University of Technology,

Kochi, Japan

For the degree of

Doctor of Engineering

Assessment Committee:

Supervisor: Professor Kazuya KOBIRO
Co-Supervisor: Professor Nagatoshi NISHIWAKI
Co-Supervisor: Associate Professor Masataka OHTANI
Professor Hisao MAKINO
Assistant Professor Akitaka ITO

March 2021

Abstract

Porous materials having accessible pores and a large surface area are promising functional materials such as gas storage and separation, energy storage, drug delivery, catalysis, and catalyst supports. In particular, metal oxides are intriguing materials because of their intrinsic properties of semi-conductive behavior, catalytic activity, high temperature stability, durability, easiness of handling, and cost. In order to improve the performance of materials, it is extremely important to control the size, morphology, crystallinity, and stoichiometry according to the specific application. Therefore, considerable effort has been devoted to developing new methods for the synthesis of porous materials. Among them, hydrothermal and solvothermal methods have received much attention because of their simplicity, low cost, and ability to make new porous nanomaterials. In this thesis, solvothermal conditions for controlling the morphology and crystal structure of porous nanomaterials are focused.

Submicron-sized Nb_2O_5 porous spheres with a high specific surface area (300 m^2/g) and nano concave–convex surfaces were synthesized *via* a rapid one-pot single-step alcothermal reaction. Prolonged reaction time or high reaction temperatures resulted in a morphology change of Nb_2O_5 from amorphous sphere to rod crystals with hexagonal crystal phase. A similar alcothermal reaction yielded TiO_2–Nb_2O_5 composites porous spheres, whose Ti : Nb molar ratio was controlled by changing the precursor solution component ratios. A simple thermal treatment of amorphous TiO_2–Nb_2O_5 porous sphere consisting of 1 : 2 (molar ratio) Ti : Nb at 600 °C for 2 h induced crystal phase transfer from amorphous to monoclinic crystal phase of submicron-sized $TiNb_2O_7$ porous spheres with a specific surface area of 50 m^2/g.

Ultrafine TiO_2 nanocrystals were synthesized using a rapid heating, one-pot solvothermal method. These nanocrystals are extremely small with a narrow size distribution (3.0 ± 0.4 nm). The detailed structural analysis by using transmission electron microscopy reveals periodic alignment of the resultant TiO_2 nanocrystals with hexagonal symmetry due to

their size uniformity. The drop-casting deposition and calcination of these nanocrystals are also enable to convert into mesoporous thin layer films with nano convex-concave surface. The resultant transparent mesoporous thin layer exhibits not only anti-reflection properties but also high photocatalytic activity.

A new Ti-based nanocrystals were synthesized by a hydrothermal reaction using squaric acid as an additive. Urchin-like nanocrystals and hexagonal plates were obtained from low and high concentrations of the precursor, respectively. The obtained hexagonal plates could be a new MOF consisting of titanium ions and squarate ligands. On the other hand, the obtained urchin-like nanocrystals showed a rutile-type TiO_2 phase and a high specific surface area (122 m^2/g). The urchin-like rutile-type TiO_2 nanocrystals resulted in highly efficient dispersion of Ru. The Ru/TiO_2 catalyst prepared from the urchin-like rutile-type TiO_2 nanocrystals afforded higher activity in CO_2 methanation reaction.

Table of Contents

CHAPTER I

CHAPTER II

CHAPTER III

CHAPTER IV

Chapter I.

General Introduction

1–1. Porous materials

Compared to atoms in the bulk, different physical and chemical properties of atoms exposed at solid surface are the driving force for many chemical reactions. There are two representative approaches to increase the number of surface atoms on solids: to decrease the particle size and to form pore network within the solids (Figure 1–1). Therefore, porous materials having accessible pores and large surface areas, including activated carbon, silica, zeolites, metal oxides, and metal–organic frameworks (MOFs), are promising functional materials for gas storage and separation, energy storage, drug delivery, catalysis, and catalyst supports.[1] Much effort has been paid to utilize these porous materials in many research and industrial fields.[2–8] In particular, metal oxides are intriguing materials because of their intrinsic properties of semi-conductive behavior, catalytic activity, high temperature stability, durability, easiness of handling, and costs.[9]

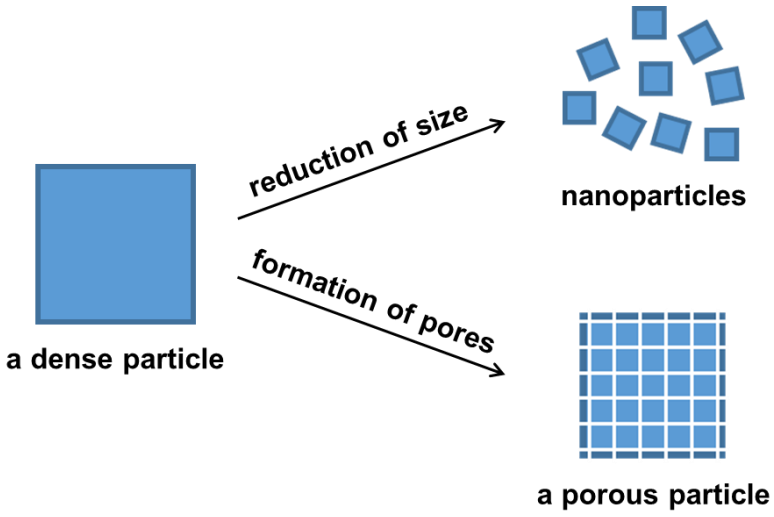

Figure 1–1. Schematic illustration of the approaches to increase the number of surface atoms of solids.

1–2. Synthesis of porous materials

To obtain porous materials, several methods, including solution combustion,[10] dealloying,[11] electrochemical deposition,[12] spray pyrolysis,[13] chemical precipitation method,[14] sol–gel method,[15] as well as hydrothermal and solvothermal methods,[16] have been developed. In particular, hydrothermal and solvothermal methods have received much attention because of their simplicity, low cost, and ability to make new nanomaterials.

Hydrothermal and solvothermal syntheses are generally defined as a process in a closed reaction vessel inducing a decomposition or a chemical reaction between precursors in the presence of a solvent at temperatures above their boiling points.[17] When water is used as a solvent, it is called “hydrothermal synthesis,” and when organic solvents are used instead of water, it is called “solvothermal synthesis.” In addition, when alcohols are used as a solvent, it is sometimes called "alcothermal synthesis."[18] and especially when glycols are used as a solvent, it is called "glycothermal synthesis."[19]

A precursor solution consisting of metal compounds and additives such as organic acids, organic bases, and surfactants in an appropriate solvent is treated at an elevated temperature in a pressurized vessel (Figure 1–2). Hydrothermal and solvothermal syntheses exploits that by increasing temperature and pressure changes the fundamental properties of the solvent used. Physical properties of solvents such as ionic product, density, thermal conductivity, viscosity, heat capacity, and dielectric constant are easily fundable by changing their temperatures and pressures, which is one of the most important parameters as the synthetic solvents. For example, dielectric constants of the solvents drop rapidly as temperature increases. This drop effects on the solubility of polar and ionic species which are often used in the synthesis of inorganic nanoparticles. In addition, ionic species precipitate as the dielectric constant decreases.

Hydrothermal and solvothermal syntheses allow the robustly and readily control of the

size, morphology, stoichiometry, and crystallinity of metal oxide nanoparticles and products with nanostructures. These properties can be altered by changing certain synthetic parameters, including solvent, additive, metal compound, reaction temperature, reaction time, heating rate, and pressure. Thus, this method has the advantages such as high reproducibility, simple procedure, and easy scale-up. Concerning on the reaction scale, it is also possible to extend from batch type reactors to flow type ones for the mass production. Due to these advantages, hydrothermal and solvothermal syntheses have been widely used in the field of inorganic nanoparticle synthesis (Figure 1–3).

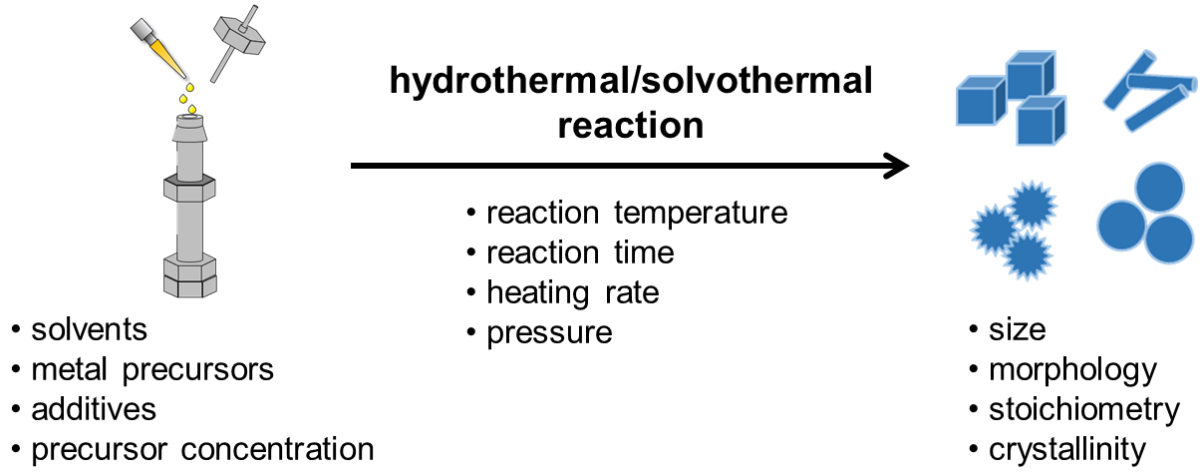

Figure 1–2. Schematic illustration of hydrothermal and solvothermal syntheses.

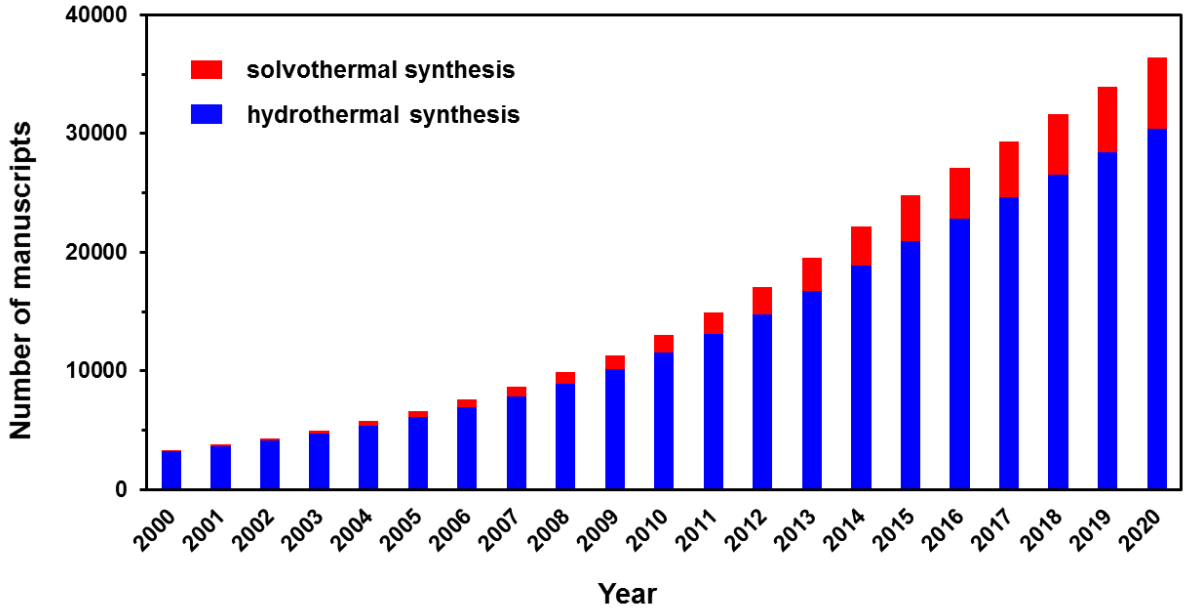

Figure 1–3. Number of papers relating the topics of "solvothermal synthesis" and "hydrothermal synthesis." Based on topic search performed in SciFinder.

1–3. Hydrothermal and solvothermal syntheses using supercritical fluids

The use of supercritical fluids to replace the conventional reaction media has attracted more attention in the synthesis of inorganic nanoparticle, since it is a new method that can speed up the process while maintaining high controllability.[20,21] The supercritical state is achieved when both the temperature and the pressure of the solvents exceed their critical points (Table 1–1).[22] Distinct from fluids in liquid or gas phase, supercritical fluids display interesting physicochemical properties such as solvation behavior, dielectric properties, and rather low viscosity. These properties abruptly change around their critical points. When the temperature and pressure of a precursor solution exceeds the critical point, the low dielectric property of the solvent leads to precipitation of nanoparticles. Rapid formation of numerous particle nuclei results in quite small homogeneous particles with a narrow size distribution can be obtained. Nanoparticles with desired properties will be obtained by tuning the synthetic conditions. Furthermore, since the supercritical state is achieved through changes in temperature and pressure, the system can be easily tuned to the optimal set points that will yield the desired nanoparticle features.

Table 1–1. Critical temperatures, pressures, and densities of the solvents.

Solvent	T_c (°C)	P_c (MPa)	ρ_c (Kg/m^3)
water	374	22.06	322
methanol	239	8.10	276
ethanol	241	6.27	273
1-propanol	264	5.17	274
2-propanol	235	4.76	273
1-butanol	290	4.42	270
1-pentanol	313	3.88	270
1-hexanol	338	3.51	268
ammonia	132	11.33	225
1-hexane	235	3.03	233
cyclohexane	280	4.08	271
toluene	319	4.14	292
1-octane	296	2.50	235

1–4. One-pot solvothermal synthesis of porous spheres

In connection with solvothermal synthesis, Wang P. *et al.* synthesized TiO_2 with porous spherical morphologies *via* an ultimately simple one-pot solvothermal route using methanol (Figure 1–4).[23] The obtained porous spheres were composed of numerous few nm-sized primary particles, resulting in a spherical secondary morphology with a few hundred nm size in diameter. In addition, the porous spheres with micro- and meso-pores have a large surface area (>200 m^2/g) and nano concave–convex surface structure. These porous spheres were named mesoporously architected roundly integrated metal oxides (MARIMOs). The synthetic approach was quite versatile yielding porous spheres such as SiO_2, ZnO, ZrO_2, and CeO_2 under similar solvothermal conditions.[24–26] In particular, preparation of composite MARIMOs, including CeO_2–ZrO_2, Al_2O_3–TiO_2, ZnO–TiO_2, SiO_2–TiO_2, Co/Mn oxide, Ni/Mn oxide, and Co/Mn/Fe oxide, were also succeeded with high homogeneity and controllable stoichiometry (Figure 1–5).[27–30] Interestingly, solid or hollow TiO_2 MARIMOs and TiO_2 assemblies with a cheek-brush morphology were obtained by changing the additives (Figure 1–6).[31] The obtained MARIMOs can be useful materials as oxidation catalysts in the electrochemical water oxidation reaction and catalyst supports in CO oxidation and CO_2 methanation.[25,26,30,32]

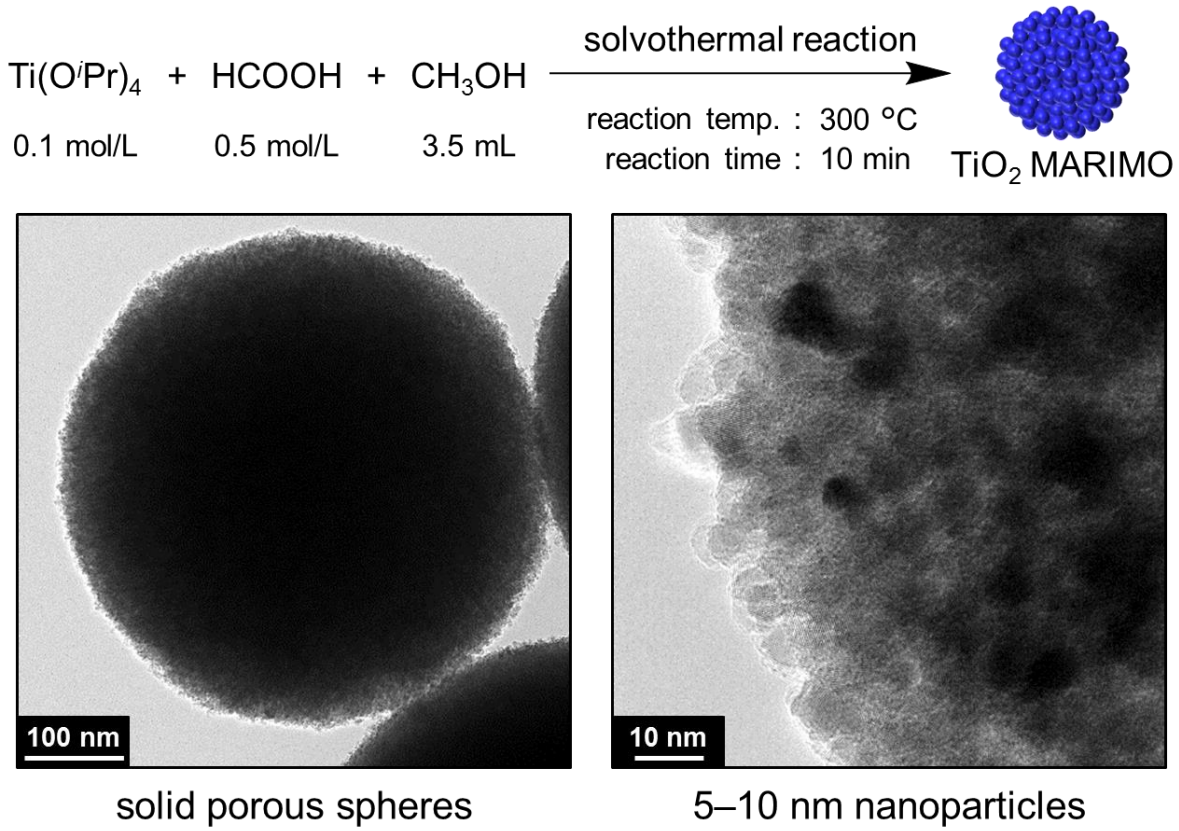

Figure 1–4. Schematic illustration of synthesis of TiO_2 MARIMO: its TEM and HR-TEM images.

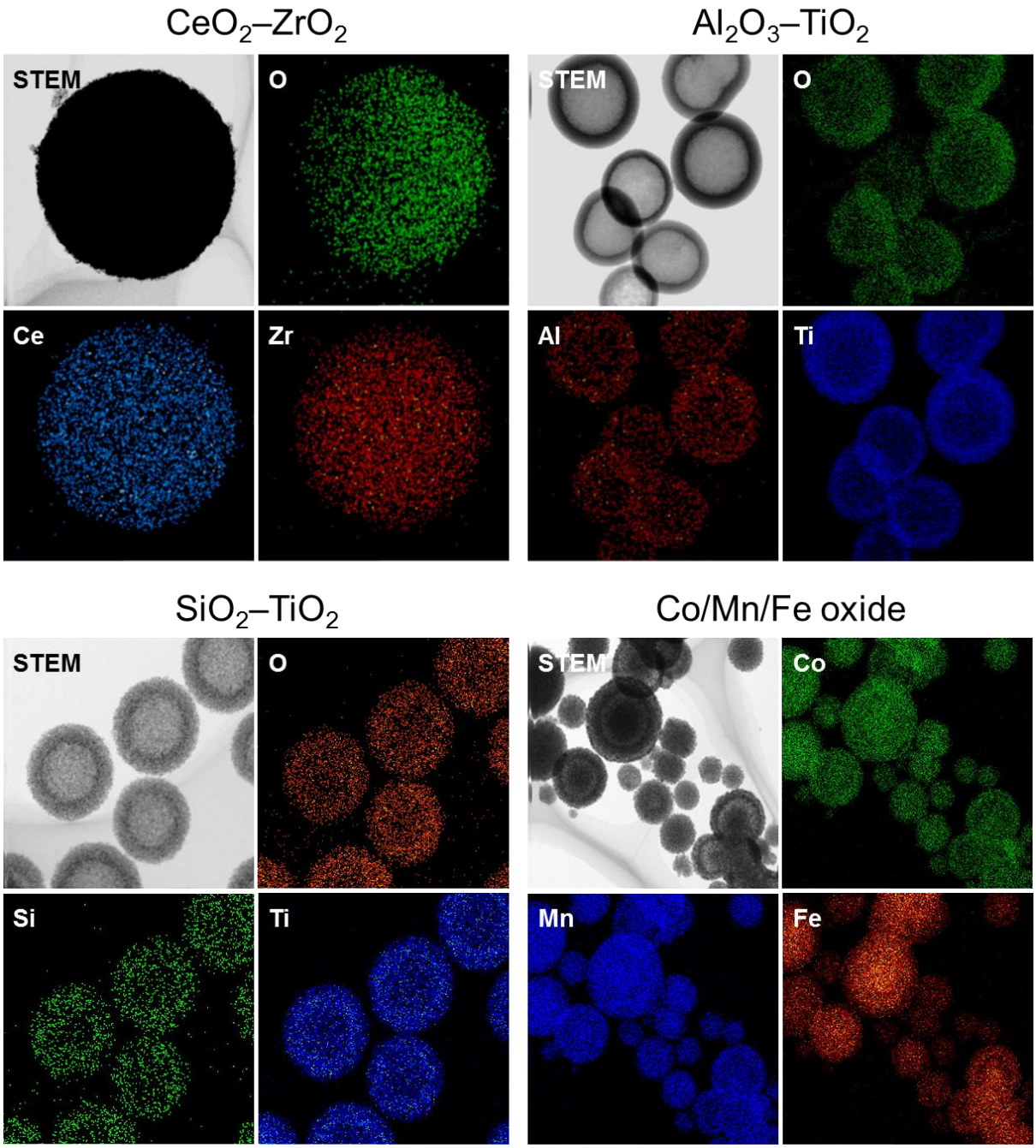

Figure 1–5. EDX mapping images of composite MARIMOs

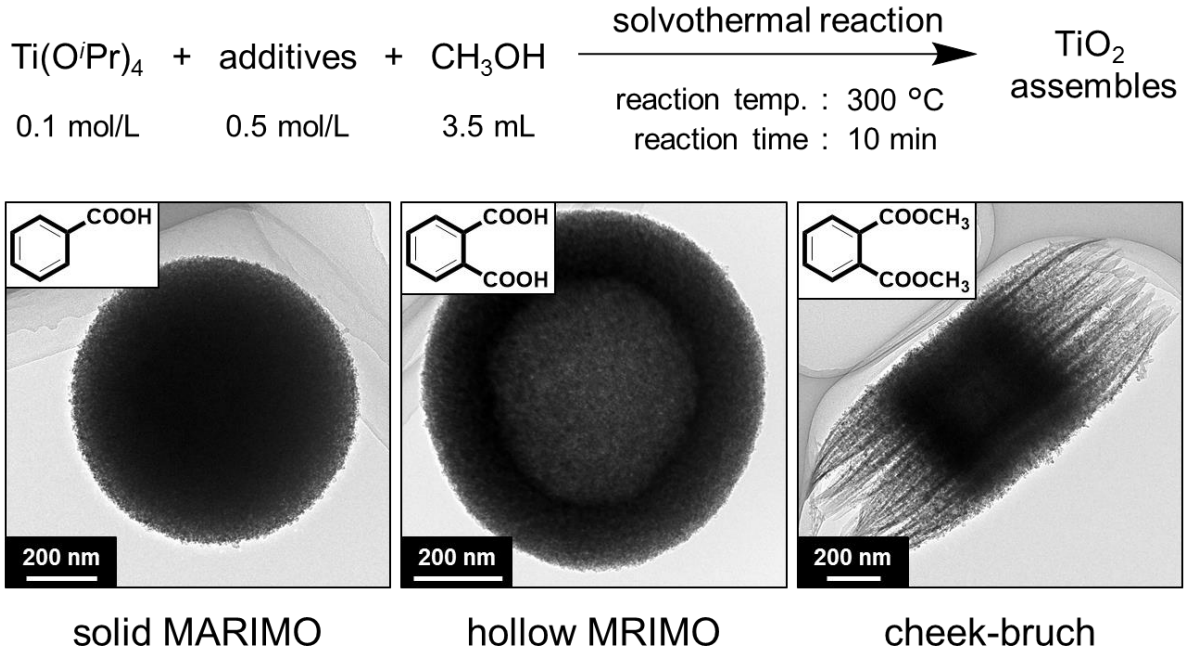

Figure 1–6. Morphological control of TiO_2 assembles by using different additives.

The key factor to yield such MARIMOs is to control hydrolysis rate of metal precursors in the precursor solutions under solvothermal conditions. In solvothermal synthesis in methanol, methanol condenses under high temperature and high pressure to yield water which subsequently reacts (eqn [1]–[3]) with metal salt (MA_n) to form metal oxide nanoparticles.

$$2CH_3OH \longrightarrow CH_3OCH_3 + H_2O \quad [1]$$

$$MA_n + nH_2O \longrightarrow M(OH)_n + nHA \quad [2]$$

$$M(OH)_n \longrightarrow MO_{\frac{n}{2}} + \frac{n}{2}H_2O \quad [3]$$

Therefore, crystal growth is suppressed and controlled to yield uniform nanoparticles. In addition, additives such as carboxylic acids, glycols, and acetylacetone coordinate to the metal ion to slow down or regulate the hydrolysis rate of the metal precursor. However, there are still many unclear points about the effect of the combination of metal precursors, additives, and solvents on morphology and crystal structure of the produced particles. In this paper, solvothermal conditions for controlling the crystal structure of the nanoparticles are focused.

1–4. Dissertation outline

This dissertation consists of five chapters. The first Chapter I describes a general introduction of the research containing dissertation outline. Chapter II explains a new aspect of the solvothermal synthesis of Nb_2O_5, TiO_2–Nb_2O_5 composites, and $TiNb_2O_7$ porous spheres. Chapter III discusses an ultimately simple synthetic method of size and crystal structure controlled metal oxide nanocrystals by a one-pot solvothermal method using oleic acid and their conversion into transparent mesoporous thin layer films. The last Chapter IV describes selective synthesis of Ti-based nanocrystals *via* hydrothermal method using squaric acid.

References

1. Valtchev, V.; Tosheva, L. Porous nanosized particles: preparation, properties, and applications. *Chem. Rev.* **2013**, *113*, 6734–6760.
2. Stark, W. J.; Stoessel, P. R.; Wohlleben, W.; Hafner, A. Industrial applications of nanoparticles. *Chem. Soc. Rev.* **2015**, *44*, 5793–5805.
3. Yu, S. H.; Lee, S. H.; Lee, D. J.; Sung, Y. E.; Hyeon, T. Conversion reaction-based oxide nanomaterials for lithium ion battery anodes. *Small* **2016**, *12*, 2146–2172.
4. Lim, S. A. and Ahmed, M. U. Electrochemical immunosensors and their recent nanomaterial-based signal amplification strategies: a review. *RSC Adv.* **2016**, *6*, 24995–25014.
5. Zhou, M.; Wang, H.; Guo, S. Towards high-efficiency nanoelectrocatalysts for oxygen reduction through engineering advanced carbon nanomaterials. *Chem. Soc. Rev.* **2016**, *45*, 1273–1307.
6. Abdelbasir, S. M.; Shalan A. E. An overview of nanomaterials for industrial wastewater treatment. *Korean J. Chem. Eng.* **2019**, *36*, 1209–1225.
7. Sharma, D.; Hussain, C. M. Smart nanomaterials in pharmaceutical analysis. *Arabian J. Chem.* **2020**, *13*, 3319–3343.
8. Jain, P.; Patidar, B.; Bhawsar, J. Potential of nanoparticles as a corrosion inhibitor: a review. *J. Bio Tribo Corros.* **2020**, *6*, 43.
9. Boyjoo, Y.; Wang, M.; Pareek, V. K.; Liu, J.; Jaroniec, M. Synthesis and applications of porous non-silica metal oxide submicrospheres. *Chem. Soc. Rev.* **2016**, *45*, 6013–6047.
10. Varma, A.; Mukasyan, A.; Rogachev, A.; Manukyan, K. V. Solution combustion synthesis of nanoscale materials. *Chem. Rev.* **2016**, *116*, 14493–14586.
11. Qiu, H.-J.; Peng, L.; Li, X.; Xu, H. T.; Wang, Y. Using Corrosion to fabricate various

nanoporous metal structures. *Corros. Sci.* **2015**, *92*, 16–31.

12. Lahiri, A.; Endres, F. Review-electrodeposition of nanostructured materials from aqueous, organic and ionic liquid electrolytes for Li-ion and Na-ion batteries: a comparative review. *J. Electrochem. Soc.* **2017**, *164*, 597–612.
13. Leng, J.; Wang, Z.; Wang, J.; Wu, H.-H.; Yan, G.; Li, X.; Guo, H.; Liu, Y.; Zhang, Q.; Guo, Z. Advances in nanostructures fabricated via spray pyrolysis and their applications in energy storage and conversion. *Chem. Soc. Rev.* **2019**, *48*, 3015–3072.
14. Huang, Y. X.; Xie, M.; Wang, Z. H.; Jiang, Y.; Yao, Y.; Li, S. J.; Li, Z. H.; Li, L.; Wu, F.; Chen, R. J. A chemical precipitation method preparing hollow–core–shell heterostructures based on the prussian blue analogs as cathode for sodium-ion batteries. *Small* **2018**, *14*, 1801246.
15. Danks, A. E.; Hall, S. R.; Schnepp, Z. The evolution of 'sol–gel' chemistry as a technique for materials synthesis. *Mater. Horiz.* **2016**, *3*, 91–112.
16. Xu, B.; Wang, X. Solvothermal synthesis of monodisperse nanocrystals. *Dalton Trans.* **2012**, *41*, 4719–4725.
17. Slostowski, C.; Marre, S.; Babot, O.; Toupance, T.; Aymonier, C. Near- and supercritical alcohols as solvents and surface modifiers for the continuous synthesis of cerium oxide nanoparticles. *Langmuir* **2012**, *28*, 16656–16663.
18. Demazeau, G. Review. solvothermal processes: definition, key factors governing the involved chemical reactions and new trends. *Z. Naturforschung B* **2010**, *65*, 999–1006.
19. Inoue, M. Glycothermal synthesis of metal oxides. *J. Phys.: Condens. Matter* **2004**, *16*, S1291–S1303.
20. Lane, M. K. M.; Zimmerman, J. B. Controlling metal oxide nanoparticle size and shape with supercritical fluid synthesis. *Green Chem.* **2019**, *21*, 3769–3781.
21. Xu, Y.; Musumeci, V.; Aymonier, C. Chemistry in supercritical fluids for the synthesis of

metal nanomaterials. *React. Chem. Eng.* **2019**, *4*, 2030–2054.

22. Aymonier, C.; Philippot, G.; Erriguible, A.; Marre, S. Playing with chemistry in supercritical solvents and the associated technologies for advanced materials by design. *J. Supercrit. Fluids* **2018**, *134*, 184–196.
23. Wang, P.; Kobiro, K. Ultimately simple one-pot synthesis of spherical mesoporous TiO_2 nanoparticles in supercritical methanol. *Chem. Lett.* **2012**, *41*, 264–266.
24. Wang, P.; Ueno, K.; Takigawa, H.; Kobiro, K. Versatility of one-pot, single-step synthetic approach for spherical porous (metal) oxide nanoparticles using supercritical alcohols. *J. Supercrit. Fluids* **2013**, *78*, 124–131.
25. Kan, K.; Yamamoto, E.; Ohtani, M.; Kobiro, K. Solvothermal synthesis of monodisperse porous zirconia spheres with large surface area. *Eur. J. Inorg. Chem.* **2020**, 4435–4441.
26. Taniguchi, A.; Kumabe, Y.; Kan, K.; Ohtani, M.; Kobiro, K. Ce^{3+} -enriched spherical porous ceria with an enhanced oxygen storage capacity. *RSC Adv.* **2021**, *11*, 5609–5617.
27. Pradeep, E. K. C.; Habu, T.; Tooriyama, H.; Ohtani, M.; Kobiro, K. Ultra-simple synthetic approach to the fabrication of CeO_2–ZrO_2 mixed nanoparticles into homogeneous, domain, and core–shell structures in mesoporous spherical morphologies using supercritical alcohols. *J. Supercrit. Fluids* **2015**, *97*, 217–223.
28. Pradeep, E. K. C.; Ohtani, M.; Kobiro, K. A simple synthetic approach to Al_2O_3–TiO_2 and ZnO–TiO_2 mesoporous hollow composite assemblies consisting of homogeneously mixed primary particles at the nano level. *Eur. J. Inorg. Chem.* **2015**, 5621–5627.
29. Nguyen, H. T. T.; Habu, T.; Ohtani, M.; Kobiro, K. One-step direct synthesis of SiO_2–TiO_2 composite nanoparticle assemblies with a hollow spherical morphology. *Eur. J. Inorg. Chem.* **2017**, 3017–3023.
30. Ohtani, M.; Muraoka, T.; Okimoto, Y.; Kobiro, K. Rapid one-pot solvothermal batch synthesis of porous nano-crystal assemblies composed of multiple transition-metal

elements. *Inorg. Chem.* **2017**, *56*, 11546–11551.

31. Duriyasart, F.; Hamauzu, H.; Ohtani, M.; Kobiro, K. Three-dimensionally branched titanium dioxide with cheek-brush morphology: synthesis and its application to polymer composites. *ChemistrySelect* **2016**, *1*, 5121–5128.
32. Duriyasart, F.; Irizawa, A.; Hayashi, K.; Ohtani, M.; Kobiro, K. Sintering-resistant metal catalysts supported on concave-convex surface of TiO_2 nanoparticle assemblies. *ChemCatChem* **2018**, *10*, 3392–3396.

Chapter II.

Porous niobia spheres with large surface area: alcothermal synthesis and controlling of their composition and phase transition behavior

2–1. Introduction

Porous materials, including activated carbon, silica, metal oxides, zeolites, and metal–organic frameworks (MOFs), are promising functional materials because of their large surface area that can be used to adsorb several materials and achieve material storage-release for material transfer. These unique properties allow for applications such as gas storage and separation, catalysis, and catalyst supports.[1] In particular, metal oxides are intriguing because of their intrinsic high-temperature stability and durability.[2]

To obtain porous materials, several methods, including solution combustion,[3] dealloying,[4] electrochemical deposition,[5] spray pyrolysis,[6] sol–gel method,[7] as well as hydrothermal and solvothermal methods,[8] have been developed. In particular, the solvothermal method using high-temperature non-aqueous solvents as reaction media is a novel approach to prepare size-, morphology-, and stoichiometry-controlled metal oxides. In this context, a unique one-pot and single-step solvothermal method was developed to afford SiO_2, TiO_2, ZnO, ZrO_2, and CeO_2 with porous spherical morphologies, where numerous few nm-sized primary particles aggregate to yield a spherical secondary morphology with a few hundred nm in diameter.[9] These porous spheres were named Mesoporously Architected Roundly Integrated Metal Oxides (MARIMOs). The large surface areas of MARIMOs with micro- and meso-pores and nano concave–convex surface structure impart their unique abilities. Both solid and hollow MARIMOs can be obtained with TiO_2. In addition, composite MARIMOs, including CeO_2–

ZrO_2,[10] Al_2O_3–TiO_2,[11] ZnO–TiO_2,[11] SiO_2–TiO_2,[12] Co/Mn oxide,[13] Ni/Mn oxide,[13] and Co/Mn/Fe oxide[13] have been prepared via the solvothermal method with tightly controllable stoichiometry. Thus, solvothermal method is a versatile approach for obtaining metal oxides with a porous spherical structure, large surface area, and nano concave–convex surface structure.

Nb_2O_5 has been used as a photocatalyst,[14,15] solid acid,[16] catalyst support,[17,18] and anode material for lithium and sodium ion batteries.[19] Several preparation methods are available for these materials.[20] For example, Li C. C. *et al.* prepared monodisperse glycolated niobium oxide spheres *via* a simple antisolvent precipitation approach. Mesoporous niobium oxide spheres with a large surface area of 312 m^2/g were obtained by hydrothermal treatment.[21] Li L. *et al.* synthesized Nb_2O_5 hollow nanospheres by heating a water solution of niobium oxalate and sodium dihydrogen phosphate dihydrate at 220 °C for 48 h.[22] Dai Z. F. *et al.* prepared monodispersed Nb_2O_5 microspheres *via* a facile one-pot solvothermal route using an isopropyl alcohol solution of niobium pentachloride and tetrabutyl ammonium hydroxide at 200 °C for 24 h.[23] However, simpler preparation methods should be developed for further acceleration of their practical uses. Thus, niobium oxide and variants of MARIMOs with large surface area were prepared herein using a facile synthesis method for Nb_2O_5, TiO_2–Nb_2O_5 composite, and $TiNb_2O_7$ MARIMOs.

2–2. Experiment

2–2–1. Materials

Methanol, formic acid, niobium(V) ethoxide [$Nb(OEt)_5$], and titanium tetraisopropoxide [$Ti(O^iPr)_4$] were obtained from FUJIFIM Wako Pure Chemical Corporation. All reagents were used as received unless otherwise noted.

2–2–2. Synthetic procedure

Synthesis of Nb_2O_5 MARIMO. First, $Nb(OEt)_5$ (88 µL,0.35 mmol) was added to a solution of formic acid (67 µL, 1.75 mmol) in methanol (3.5 mL) under vigorous stirring. The resultant precursor solution was transferred to an SUS-316 stainless steel tubular reactor with a 10 mL inner volume and the reactor was then sealed with an SUS-316 screw cap. The sealed reactor was heated to 300 °C at a rate of 5.4 °C/min and the temperature was maintained at 300 °C for 10 min. The reaction was quenched by placing the reactor in an ice-water bath. The obtained precipitates were centrifuged, washed several times with methanol, and dried under vacuum to afford a powdery product.

Synthesis of TiO_2–Nb_2O_5 composite MARIMOs. Aliquots of $Ti(O^iPr)_4$ and $Nb(OEt)_5$ were added to a solution of formic acid (67 µL, 1.75 mmol) in methanol (3.5 mL) under vigorous stirring. Similar treatments of the solution as the above mentioned Nb_2O_5 MARIMO synthesis yielded the TiO_2–Nb_2O_5 composite MARIMO powdery products.

Formation of $TiNb_2O_7$ MARIMO *via* crystallization of the amorphous TiO_2–Nb_2O_5 composite MARIMO. First, $Ti(O^iPr)_4$ (174 µL, 0.58 mmol) and $Nb(OEt)_5$ (293 µL, 1.17 mmol) was added to a solution of formic acid (333 µL, 8.75 mmol) in methanol (17.5 mL) under vigorous stirring. The resultant precursor solution was sealed in a Teflon-lined autoclave with a 50 mL inner volume. The sealed autoclave was heated to 200 °C at a rate of 5.4 °C/min

and the temperature was maintained at 200 °C for 3 h. After cooling at room temperature, the precipitates were centrifuged, washed several times with methanol, and dried under vacuum to afford a powdery amorphous TiO_2–Nb_2O_5 composite MARIMO. The obtained product was calcined in air at 600 °C for 2 h at 2 °C/min heating rate to yield the final product.

2–2–3. Characterization methods

Transmission electron microscopy. The transmission electron microscopy (TEM) images were obtained using a JEOL JEM-2100F microscope. The specimens were prepared as follows: samples were dispersed in methanol; 10 μL of the resultant dispersion was drop-casted onto a carbon-coated copper microgrid (Okenshoji, Japan); and the solvent was evaporated under atmospheric pressure. Energy-dispersive X-ray (EDX) mappings and line-scan plots for the STEM images were obtained using an Oxford INCA X-max 80 EDX spectrometer.

Scanning electron microscopy. Scanning electron microscopy (SEM) was performed using a Hitachi SU8020 FE-SEM. The specimens were prepared by drop-casting the sample dispersion on a silicon wafer.

X-ray diffraction measurements. X-ray diffraction (XRD) patterns were recorded using a Rigaku SmartLab diffractometer with graphite-monochromatized Cu Kα radiation (X-ray wavelength: 1.5418 Å) in steps of 0.02° over the 2θ range of 10−80°. The powdery samples were placed on a non-refractive silicon holder (Overseas X-Ray Service, Japan). The average TiO_2 crystalline sizes were estimated from the obtained (101) peaks using the Scherrer equation.

Thermogravimetric-differential thermal analysis. Thermogravimetric-differential thermal analysis (TG-DTA) was performed using a HITACHI STA7200RV instrument. The samples were placed on an open platinum sample pan and the experiments were conducted in air at a 2 °C/min heating rate.

Nitrogen adsorption-desorption isotherm measurements. Nitrogen adsorption-desorption isotherms were obtained using a Belsorp Mini II instrument (BEL Corp.). The specific surface areas were determined using Brunauer–Emmett–Teller (BET) multipoint method with BELMaster7 software. The average pore size distributions were calculated using Barrett–Joyner–Halenda (BJH) method from the nitrogen adsorption isotherm data.

2–3. Results and discussion

2–3–1. Synthesis and morphology changes of Nb_2O_5 MARIMO

Nb_2O_5 MARIMO was prepared according to a similar method reported previously (Table 2–1, entry 1).[9] Simple heating of a methanol solution of $Nb(OEt)_5$ and formic acid at 300 °C for 10 min afforded Nb_2O_5 MARIMO in high yield (>90%). The SEM images revealed that the obtained Nb_2O_5 MARIMO was perfectly monodispersed (Figure 2–1a-i), and their shape was approximately spherical with a diameter of 630 ± 50 nm (Figures 2–1a-ii, 2–1b-i, and 2–2, red line). Also, the obtained Nb_2O_5 MARIMO was composed of many amounts of a few nm sized primary particles (Figure 2–1b-ii). The formation mechanism of Nb_2O_5 MARIMO was expected to be similar to a proposed mechanism in our previous report.[9] In the initial steps of the reaction, primitive niobium alkoxide oligomers are formed in high-temperature methanol and interconnected *via* surface interactions with carboxyl groups. As the further heating reaction of precursor mixture proceeds, niobium alkoxide oligomers react with the water, which generated by esterification of formic acid and methanol and/or dehydration condensation of methanol, to form Nb_2O_5. The pore structures are formed by gaseous products, such as CO_2 and hydrocarbons generated by decomposition of alkoxide and formic acid, trapped inside the sphere. The Nb_2O_5 MARIMO obtained without formic acid was polydisperse and obtained in low yield (<40%; Figure 2–3a). In addition, when the solvent was changed to water, spherical shapes were not formed (Figure 2–3b). From the results of the control experiment, the combination of $Nb(OEt)_5$, formic acid, and methanol is essential for the formation of a spherical morphology and high yield.

Table 2–1. Molar ratios of Ti and Nb, specific surface area, pore size, and TiO_2 crystalline size of the prepared MARIMOs.

Entry	Sample name of MARIMO[a]	Molar ration of Ti and Nb		Specific surface area[c] [m^2/g]	Pore size[d] [nm]	TiO_2 crystalline size[e] [nm]
		Precursor solution	Product[b]			
1	Nb_2O_5	0 : 100	–	302	3.3	–
2	TiO_2–Nb_2O_5-75	25 : 75	21.7 : 78.3	274	5.9	34.7
3	TiO_2–Nb_2O_5-50	50 : 50	50.1 : 49.9	200	8.9	13.6
4	TiO_2–Nb_2O_5-25	75 : 25	74.3 : 25.7	250	3.4	10.0
5	TiO_2	100 : 0	–	234	3.6	9.6

[a] Denotes the atomic% of Nb to total number of Nb and Ti atoms. [b] Evaluated by STEM/EDX analysis. [c] BET method. [d] BJH plot. [e] Estimated using the Scherrer equation.

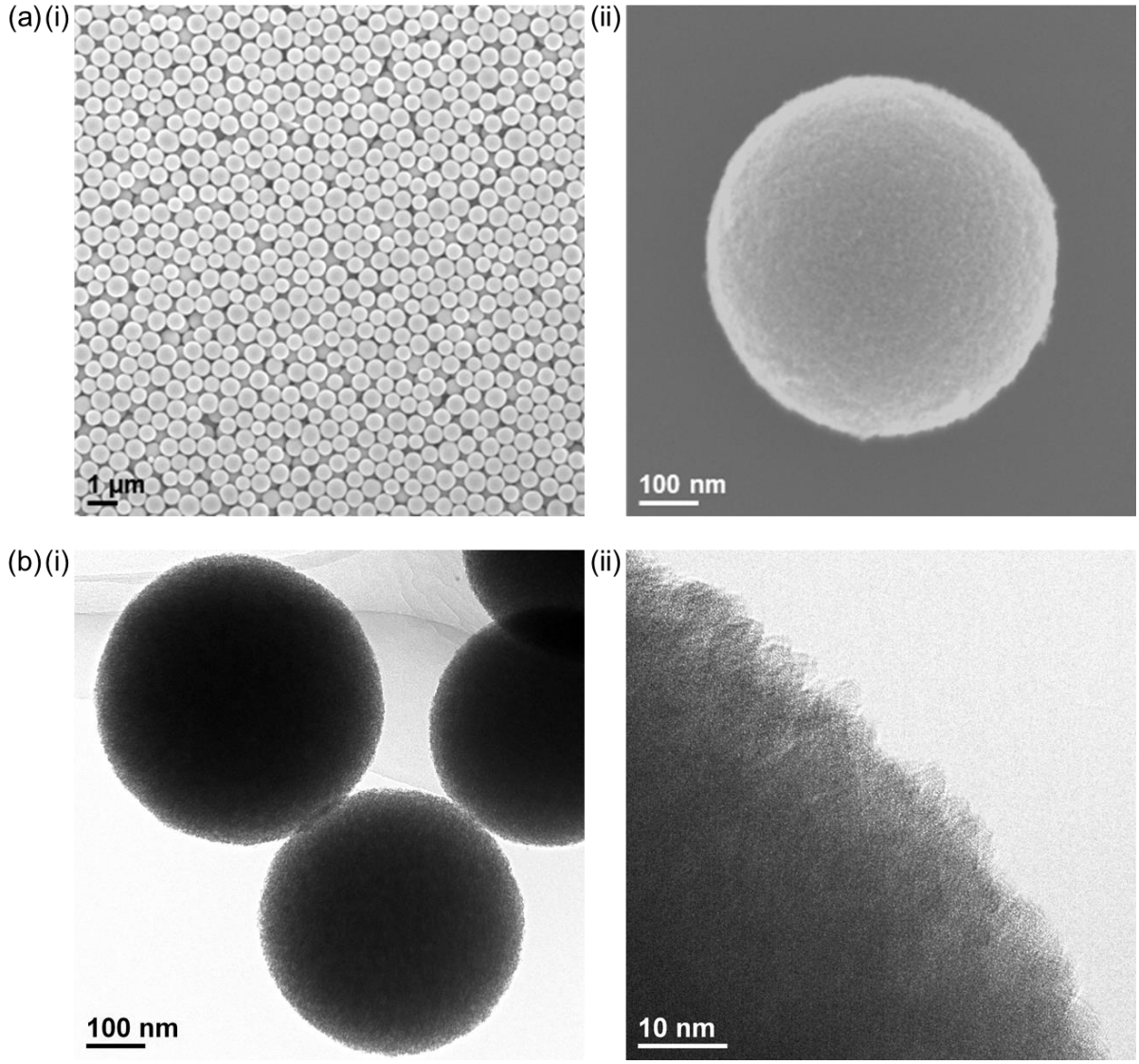

Figure 2–1. (a) SEM and (b) TEM images of the prepared Nb_2O_5 MARIMO at (i) low magnification and (ii) high magnification.

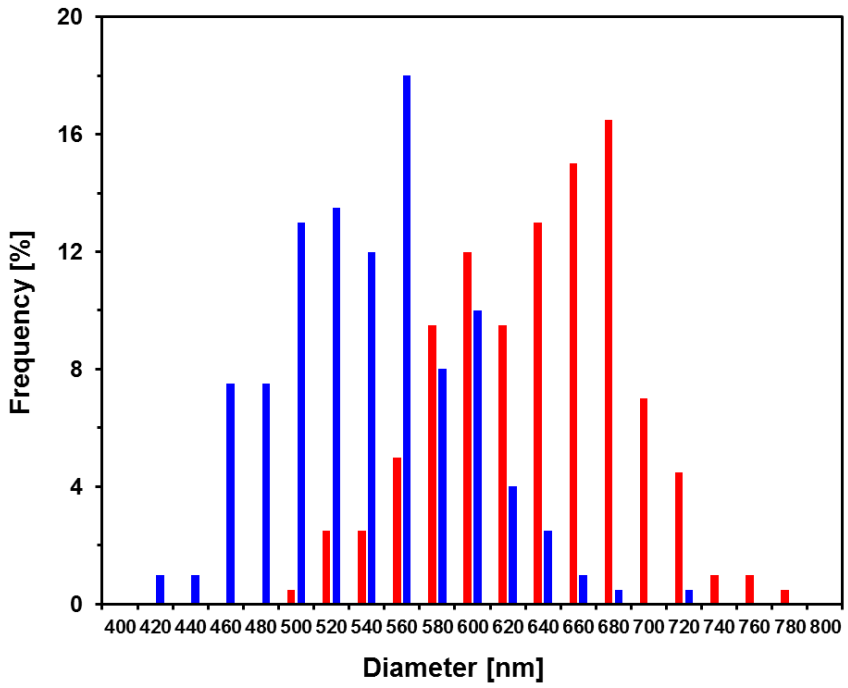

Figure 2–2. Size distribution histogram of Nb_2O_5 MARIMOs obtained by 10 min heating (red) in synthesis and by 30 min heating (blue) in synthesis. The size distribution was evaluated by statistical analyses (N = 200) using selected SEM images.

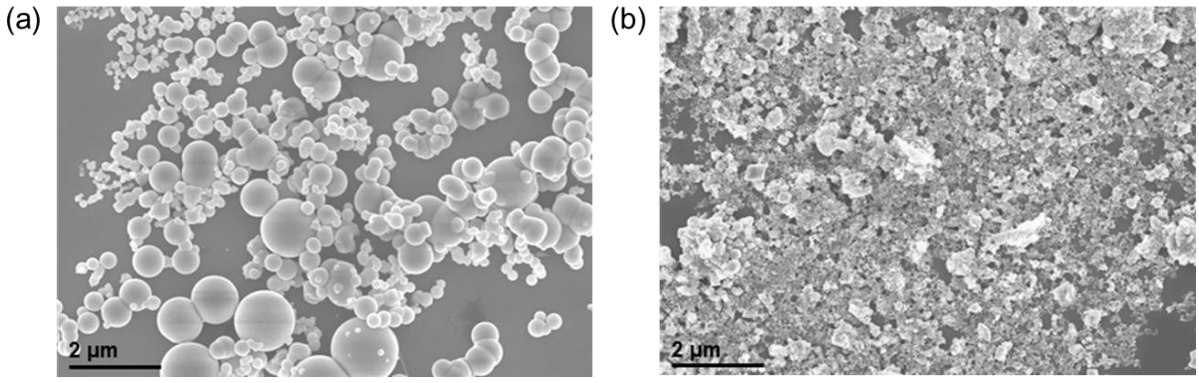

Figure 2–3. SEM image of the Nb_2O_5 Obtained from precursor solution of (a) $Nb(OEt)_5$ and methanol and (b) $Nb(OEt)_5$, formic acid, and water.

The direct evidence of the formation of a pore in Nb_2O_5 spheres was confirmed by nitrogen adsorption-desorption measurements (Figure 2–4a). If the obtained Nb_2O_5 MARIMO has no pores, the specific surface area should be a few m^2/g estimated from the diameter (*ca.* 630 nm) and specific density (d = 4.6 g/cm^3). Contrary to this expectation, the obtained Nb_2O_5 MARIMO showed a high specific surface area (302 m^2/g) and porous structure less than 10 nm-sized (Figure 2–4b). This fact strongly supports the presence of the penetrated pore inside the spherical particles.

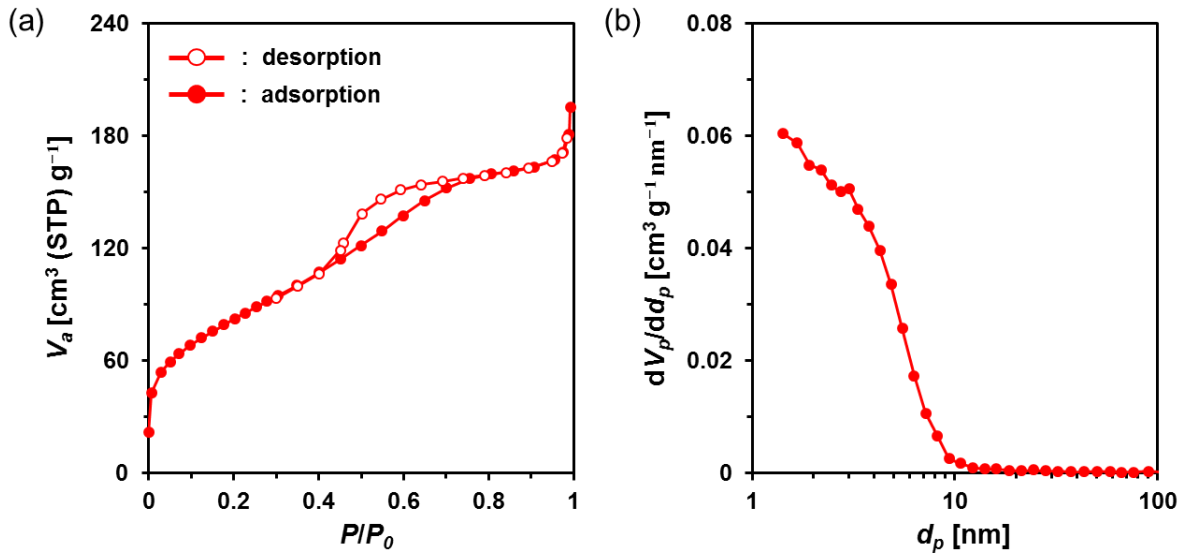

Figure 2–4. (a) Nitrogen adsorption-desorption isotherms and (b) pore size distributions of Nb_2O_5 MARIMO.

To further characterization of the obtained Nb_2O_5 MARIMO, powder XRD and electron microscopic measurements were performed. No peaks were observed in the corresponding XRD pattern (Figure 2–5), and no fringe structure in the Nb_2O_5 MARIMO primary particle was observed in the high-resolution TEM (HR-TEM) image (Figure 2–1b-ii). This indicated that the obtained Nb_2O_5 MARIMO was not crystalline but amorphous.

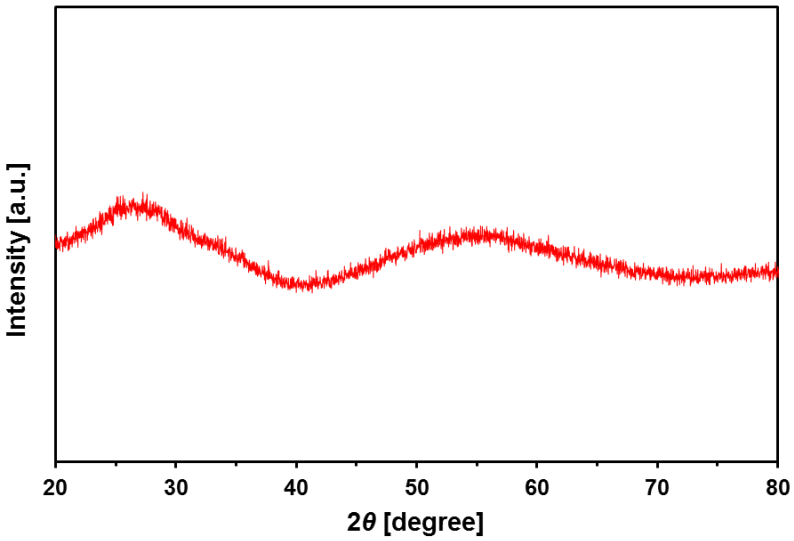

Figure 2–5. XRD patterns of Nb_2O_5 MARIMO.

To date, almost 15 polymorphic forms of Nb_2O_5 have been reported; however, hexagonal, orthorhombic, and monoclinic phases are relatively common.[20] The crystal phases significantly affect the activity of the photocatalyst[24] and solid acid.[25] Thus, it is important to control of the crystal phase formation in the obtained Nb_2O_5 MARIMO. The easiest method to improve the crystallinity is further heating. When the heating time of the precursor solution was prolonged to 60 min, the crystal phase dramatically changed from amorphous to the hexagonal phase of Nb_2O_5 (Figure 2–6c). This was concomitant with a drastic morphology change from spherical to rod-shaped (Figure 2–6a-ii). The corresponding HR-TEM image (Figure 2–6b) showed that the crystal lattice distances were 0.39 nm. In addition, the fast Fourier transform (FFT) pattern in the HR-TEM image indicated that the direction of rod growth was along the [001] facet. When a 30 min heating procedure was used, spheres and rods coexisted. Compared to 10 min heating, a volume reduction of approximately 40% was observed for the 30 min heating process, where the diameter of the obtained Nb_2O_5 MARIMO decreased to 530 ± 50 nm (Figures 2–6a-i and 2–2, blue line). Ostwald ripening was likely responsible for this shrinkage.[26,27] Similarly, higher reaction temperatures (325 and 350 °C) with a fixed reaction time (10 min) resulted in rod-like hexagonal phase nanocrystals (Figure 2–7). Although the crystallinity was successfully improved by extending the reaction time or using a high reaction temperature, the porosity was lost due to the morphology change, and the specific surface area was greatly reduced.

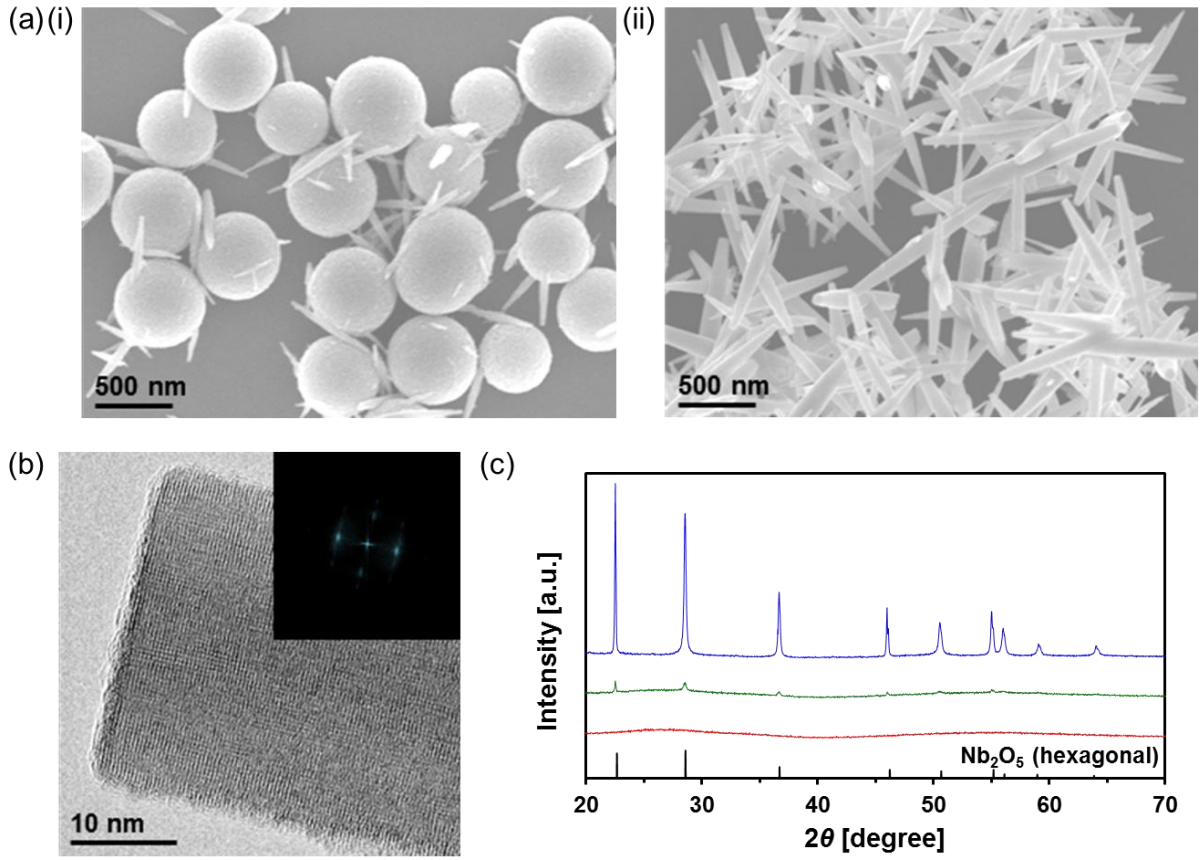

Figure 2–6. (a) SEM images of the Nb_2O_5 obtained at 300 °C with different solvothermal-reaction times (i) 30 min and (ii) 60 min. (b) HR-TEM image of the rod-like Nb_2O_5; corresponding FFT image is inset. (c) XRD patterns of the powdery products obtained using different solvothermal-reaction times (blue, 60 min; green, 30 min; red, 10 min).

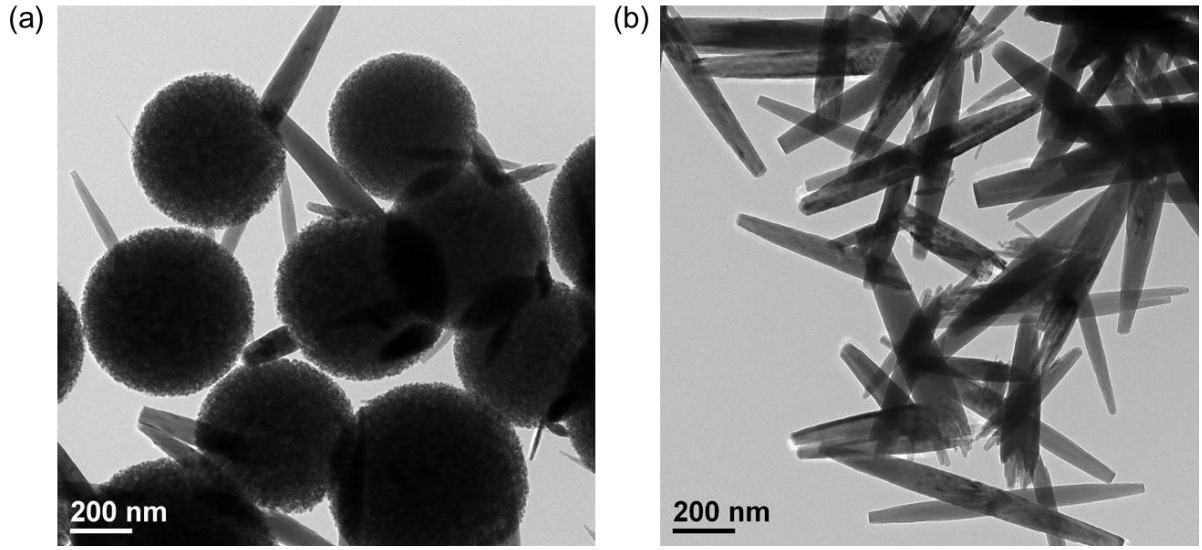

Figure 2–7. TEM images of the Nb_2O_5 obtained with different solvothermal-reaction temperature: (a) 325 °C and (b) 350 °C.

Calcination of the as-synthesized amorphous Nb_2O_5 MARIMO was used as an alternative method to change the crystal phase. Generally, amorphous Nb_2O_5 crystallizes at 500 °C into hexagonal or orthorhombic phase, tetragonal phase at 800 °C, and monoclinic phase at >1000 °C.[28] An exothermic phenomenon was observed at approximately 240 and 560 °C in TG-DTA (Figure 2–8). The exothermic peak at approximately 240 °C originated from the combustion of organic residues included in MARIMO. In addition, the exothermic peak with negligible weight loss at approximately 560 ˚C was assigned to a crystalline phase transfer.[29] Calcination of the as-synthesized amorphous Nb_2O_5 MARIMO yielded a hexagonal phase at 500 °C and an orthorhombic phase at >600 °C, as determined from their XRD patterns (Figure 2–9a). The spherical morphology was maintained at ≤600 °C, but collapsed at 700 °C (Figures 2–9b-i and 2–10). Thus, Nb_2O_5 MARIMO with improved crystallinity was successfully obtained *via* calcination at 500 or 600 °C for 2 h (Figures 2–9a, b, and 2–10a). The specific surface area of Nb_2O_5 MARIMO calcined at 500 °C was 88 m^2/g and average pore size expanded from 3.3 to 6.4 nm upon calcination (Figure 2–11).

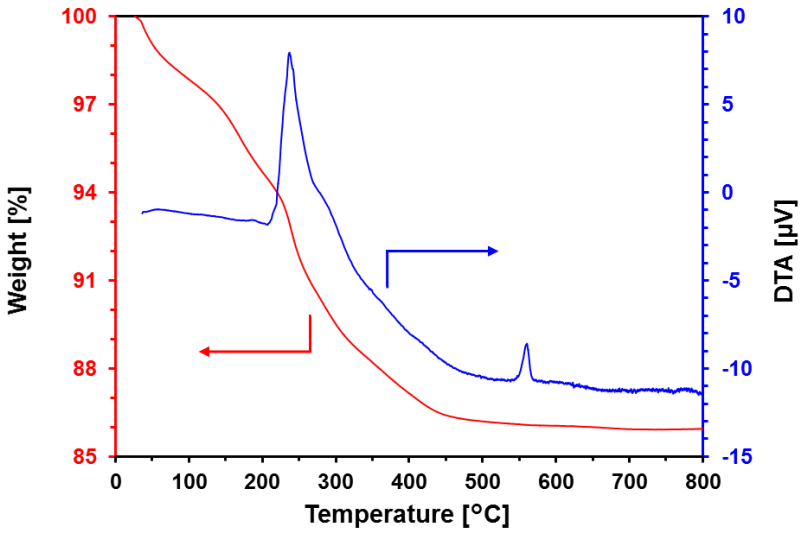

Figure 2–8. TG-DTA profiles of the as-synthesized Nb_2O_5 MARIMO measured in air at a heating rate of 2 °C/min.

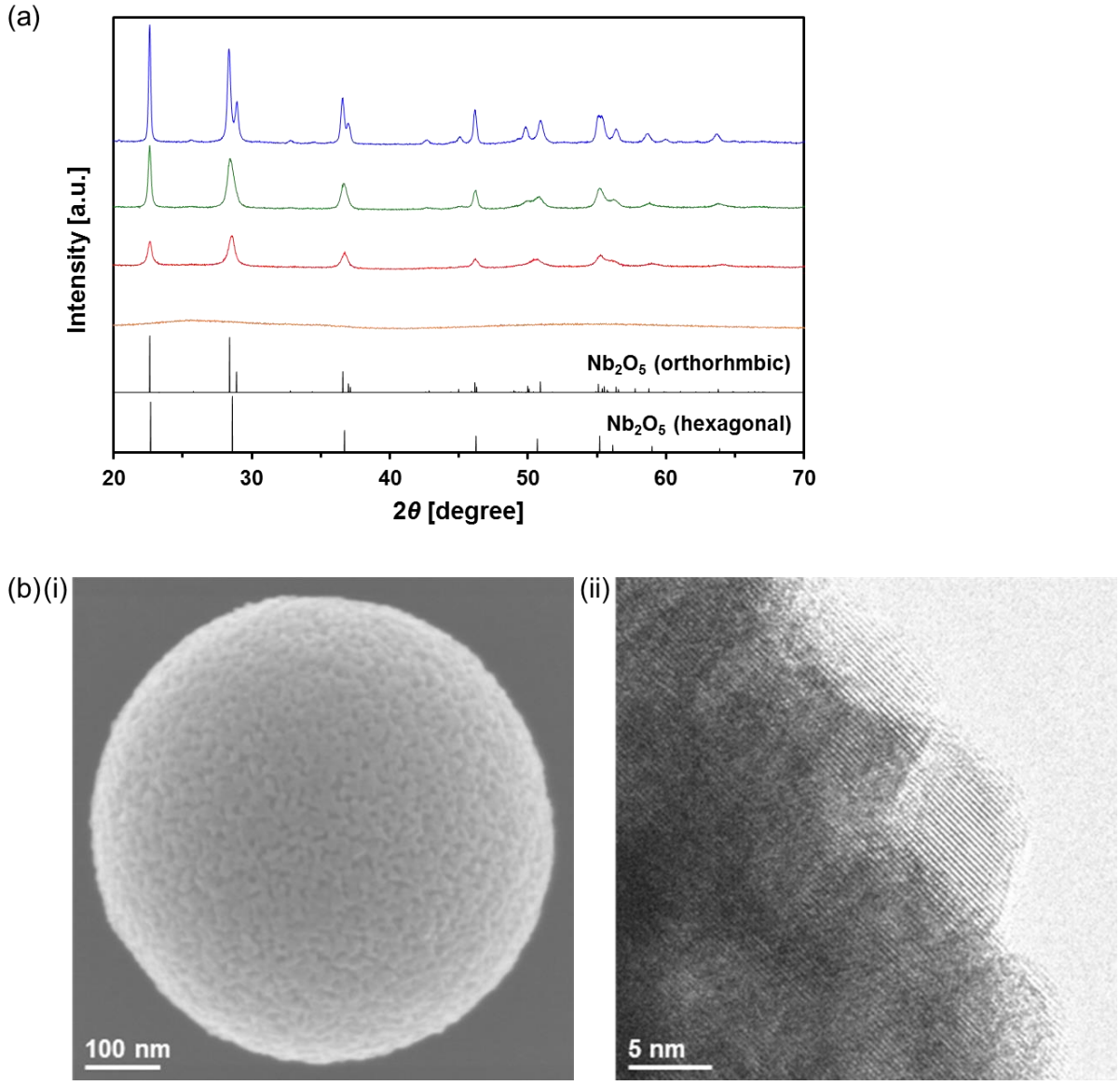

Figure 2–9. (a) XRD patterns of calcined Nb_2O_5 MARIMO at 400–700 °C (blue, 700 °C; green, 600 °C; red, 500 °C; orange, 400 °C). (b) SEM (i) and HR-TEM (ii) images of the Nb_2O_5 MARIMO calcined at 500 °C for 2 h. The crystal lattice distances were 0.31 nm.

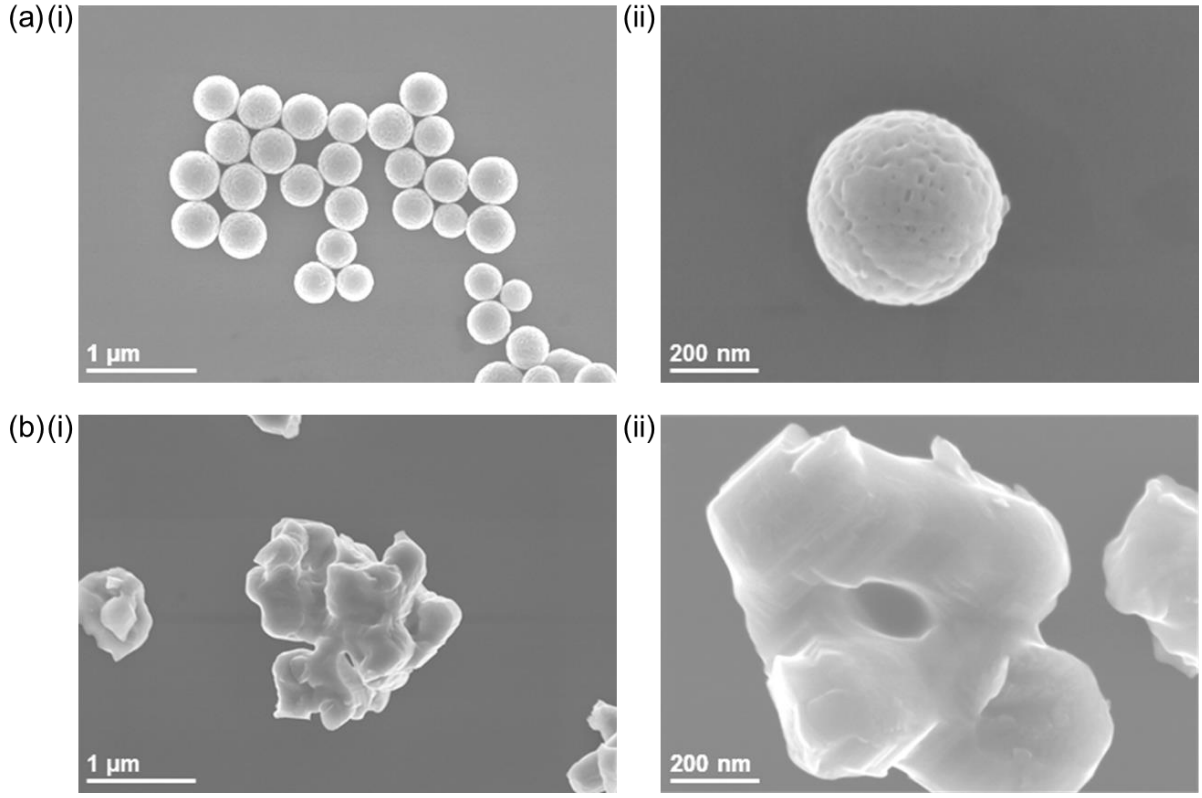

Figure 2–10. SEM images of the Nb_2O_5 obtained with different calcined temperature: (a) 600 °C and (b) 700 °C.

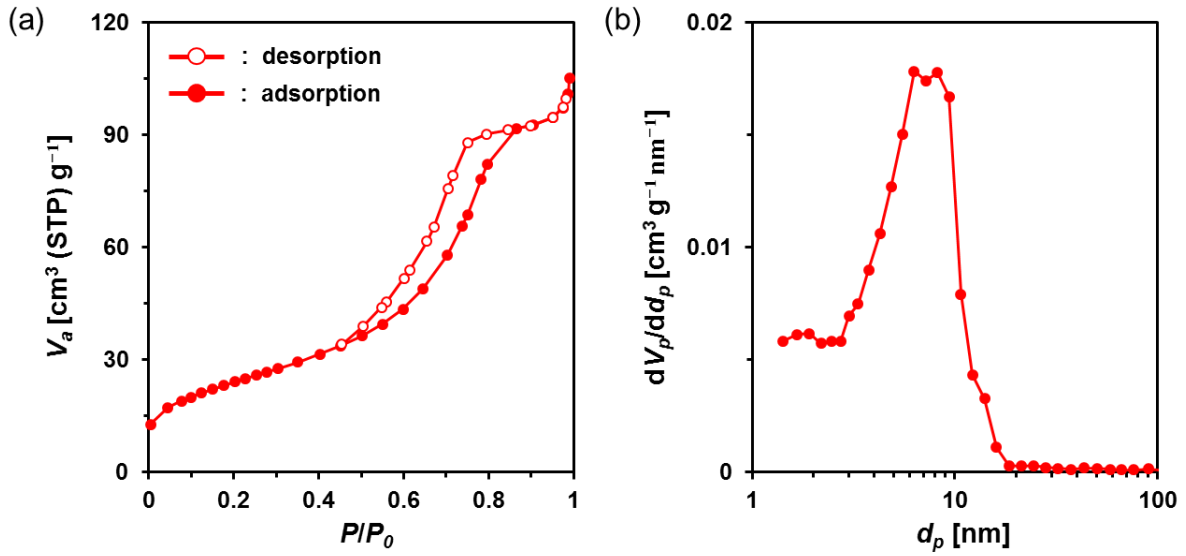

Figure 2–11. (a) Nitrogen adsorption-desorption isotherms and (b) pore size distributions of calcined Nb_2O_5 MARIMO at 500 °C.

2–3–2. Synthesis of TiO_2–Nb_2O_5 composite MARIMO

Ti–Nb binary oxides have attracted significant attention since their discovery as they exhibit reduced electrical resistance,[30] high photocatalytic activity under visible light irradiation,[31] and controlled Brønsted/Lewis acidity.[32] In particular, using Ti–Nb binary oxides in lithium and sodium ion batteries[19,33,34] has attracted great attention because of its improved electronic conductivity,[35] ion diffusion path expansion,[35] and high theoretical capacity.[36] As mentioned in the introduction, composite MARIMOs consisting of plural metal oxides have been successfully synthesized.[10–13] Herein, a one-pot and single-step technique was used to obtain TiO_2–Nb_2O_5 composite MARIMOs.

A methanol solution of $Ti(O^iPr)_4$ and $Nb(OEt)_5$ with formic acid was heated at 300 °C for 10 min. The molar ratio of Ti to Nb in the product MARIMO was easily controlled by changing the ratio in the corresponding precursor solution (entries 2–4 in Table 2–1). Nearly equivalent Ti/Nb ratios between the precursor solutions and products were obtained. As shown in Figures 2–12a–c, Ti and Nb atoms were equally distributed at the nano-level in the TiO_2–Nb_2O_5-75, TiO_2–Nb_2O_5-50, and TiO_2–Nb_2O_5-25 samples, where the numbers denote the atomic percentage of Nb among the total number of Nb and Ti atoms. In addition, the TiO_2–Nb_2O_5 composite MARIMOs were highly porous with specific surface areas of >200 m^2/g (Table 2–1 and Figure 2–13).

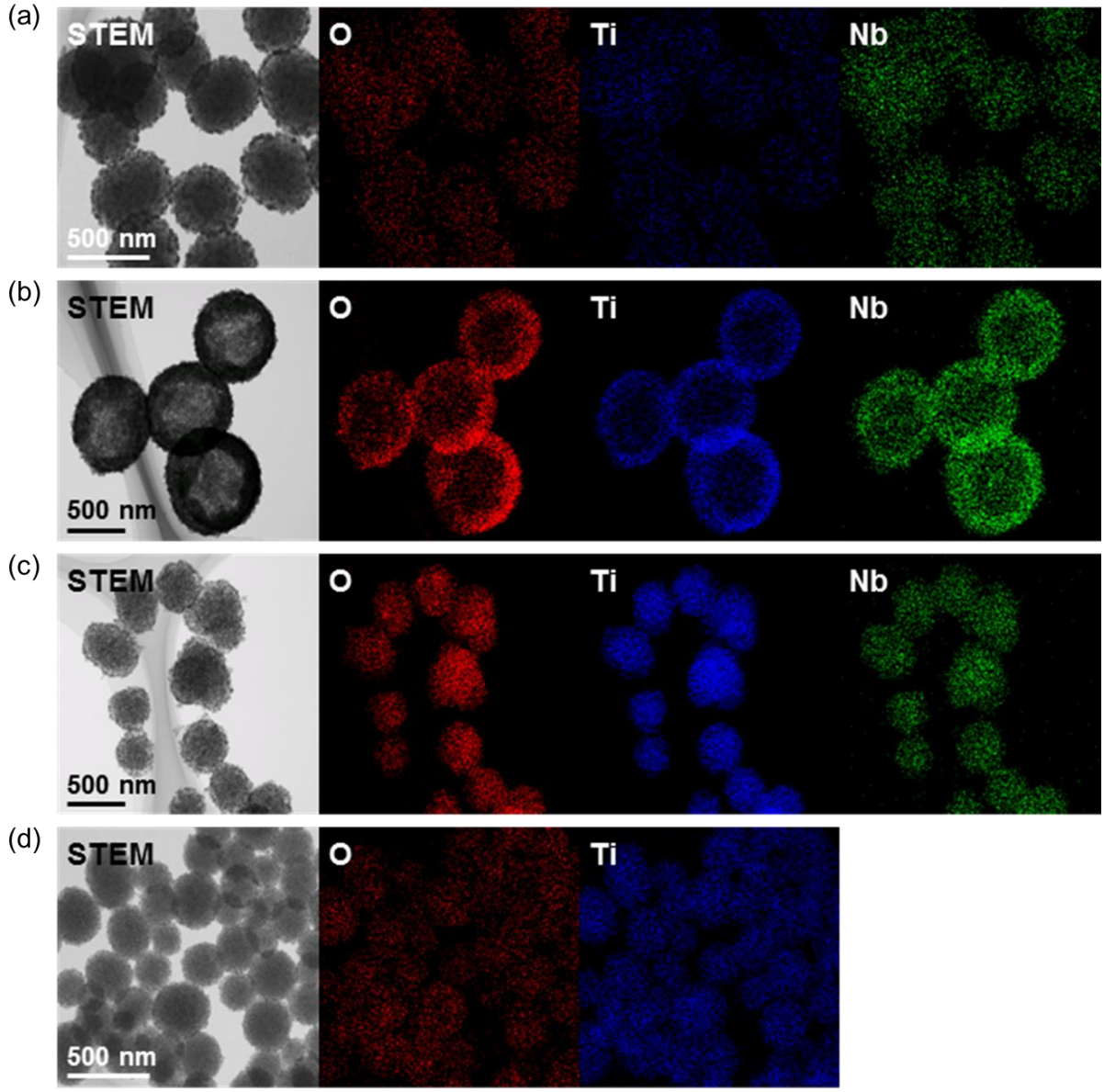

Figure 2–12. STEM/EDX analysis of the prepared TiO_2–Nb_2O_5 composite MARIMOs; (a) TiO_2–Nb_2O_5-75, (b) TiO_2–Nb_2O_5-50, (c) TiO_2–Nb_2O_5-25, and (d) TiO_2.

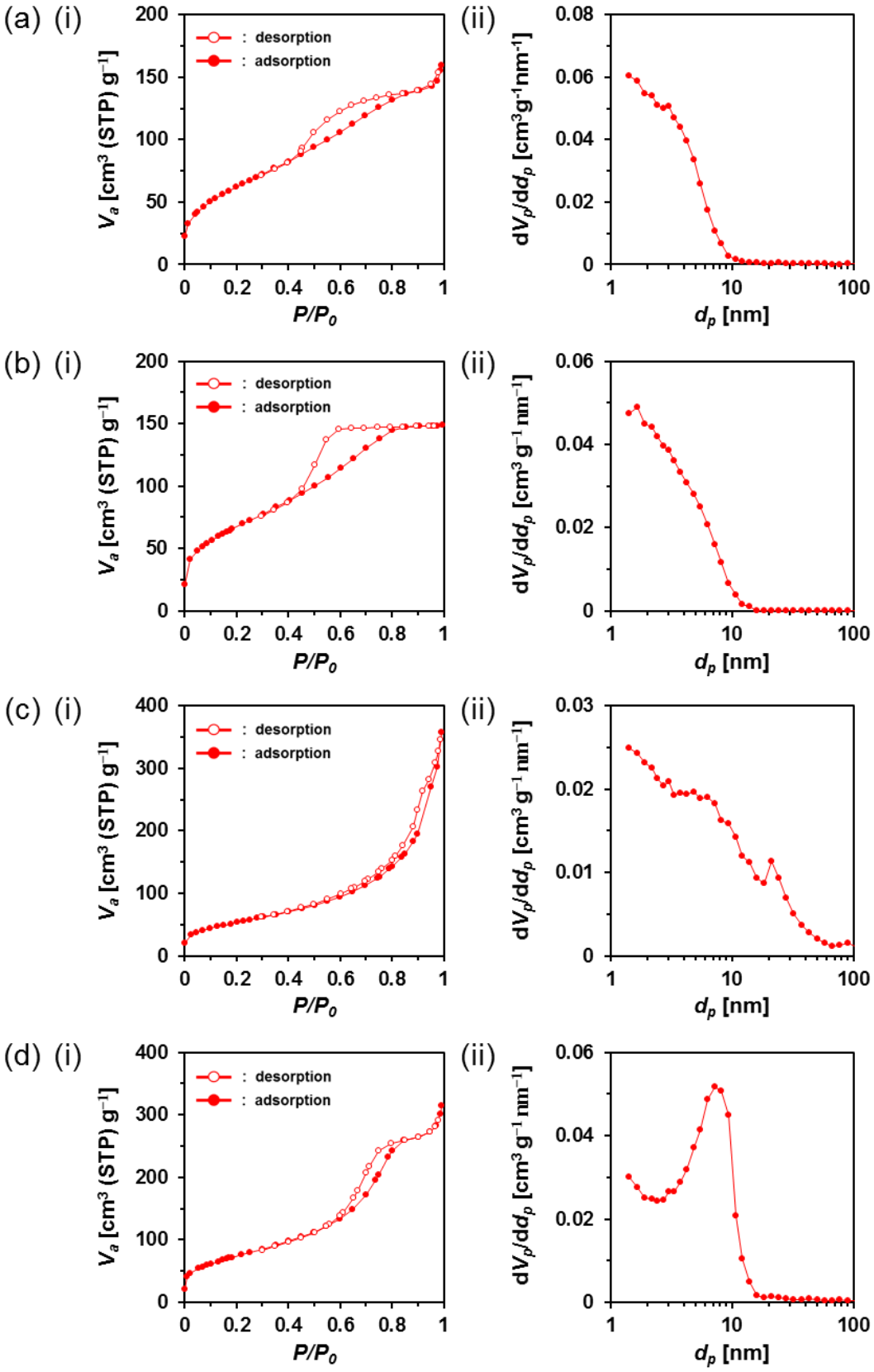

Figure 2–13. (i) Nitrogen adsorption-desorption isotherms and (ii) pore size distributions of (a) TiO_2, (b) TiO_2–Nb_2O_5-25, (c) TiO_2–Nb_2O_5-50, and (d) TiO_2–Nb_2O_5-75.

Only the tetragonal (anatase-type) TiO_2 peaks were observed in the XRD spectra when Nb atoms were included in the product MARIMOs (Figure 2–14a). Lower angle shifts of the diffraction peaks were also observed in the XRD profiles (Figure 2–14b), indicating that the composite MARIMOs consisted of solid solutions and the crystal lattice was enlarged by the doped Nb atoms with larger ionic radii (Nb^{5+} = 0.64 Å, Ti^{4+} = 0.61 Å).[37] Additionally, precursor solutions containing larger amounts of $Nb(OEt)_5$ resulted in the larger primary particle sizes of TiO_2 in the resulting MARIMOs (Table 2–1). However, this crystalline growth of TiO_2 was not observed for the Al_2O_3–TiO_2, ZnO–TiO_2, and SiO_2–TiO_2 composites.[11,12] Thus, the observed crystalline growth of TiO_2 can be ascribed to the catalytic effect of solid Nb_2O_5 as a solid acid that promoted crystalline growth.

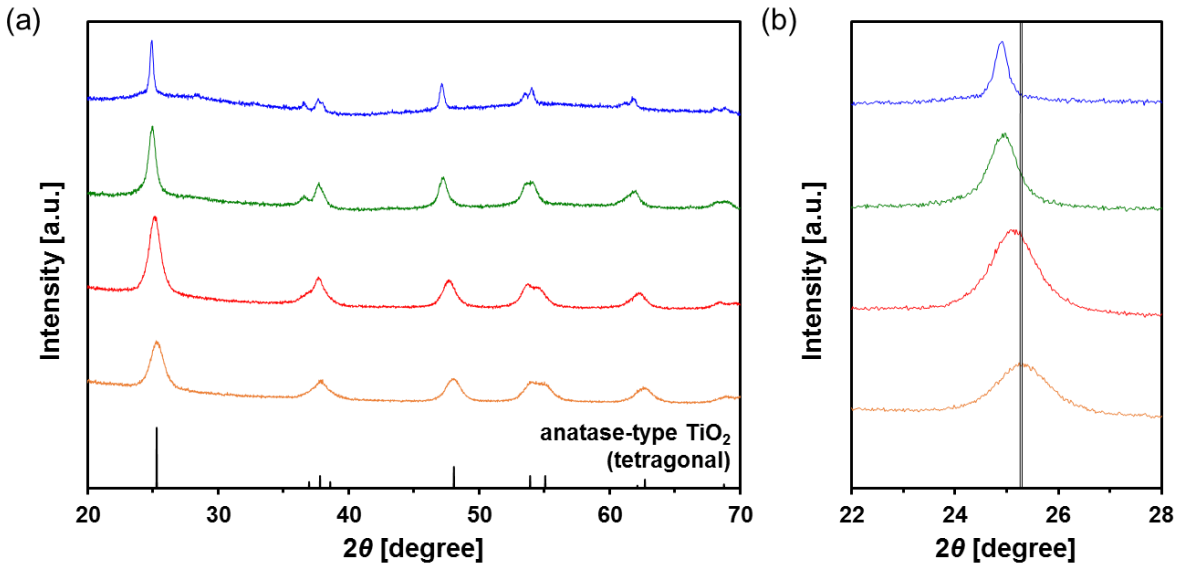

Figure 2–14. XRD patterns of the obtained powdery products prepared with different molar ratios of Ti/Nb (blue, TiO_2–Nb_2O_5-75; green, TiO_2–Nb_2O_5-50; red, TiO_2–Nb_2O_5-25; orange, TiO_2). The 2θ range: (a) 20–70° and (b) 22–28°.

Interestingly, hollow MARIMO were formed at a 50 : 50 Ti/Nb molar ratio (Figures 2–12b and 2–15). However, solid TiO_2–Nb_2O_5-50 MARIMO was obtained (Figure 2–16) when the reaction was immediately quenched at 0 min (the reaction temperature was 300 °C). From the XRD patterns, the longer reaction time yielded better crystallinity (Figure 2–17). Ostwald ripening was likely the cause of the hollow MARIMO formation.[38] These unique hollow structures imparted large surface area, low density, and high loading capacity. Therefore, the prepared materials offer promising potential for use in advanced micro-/nano-reactors, catalysis, energy storage/conversion, biomedicine, sensors, and environmental remediation applications.[39–41]

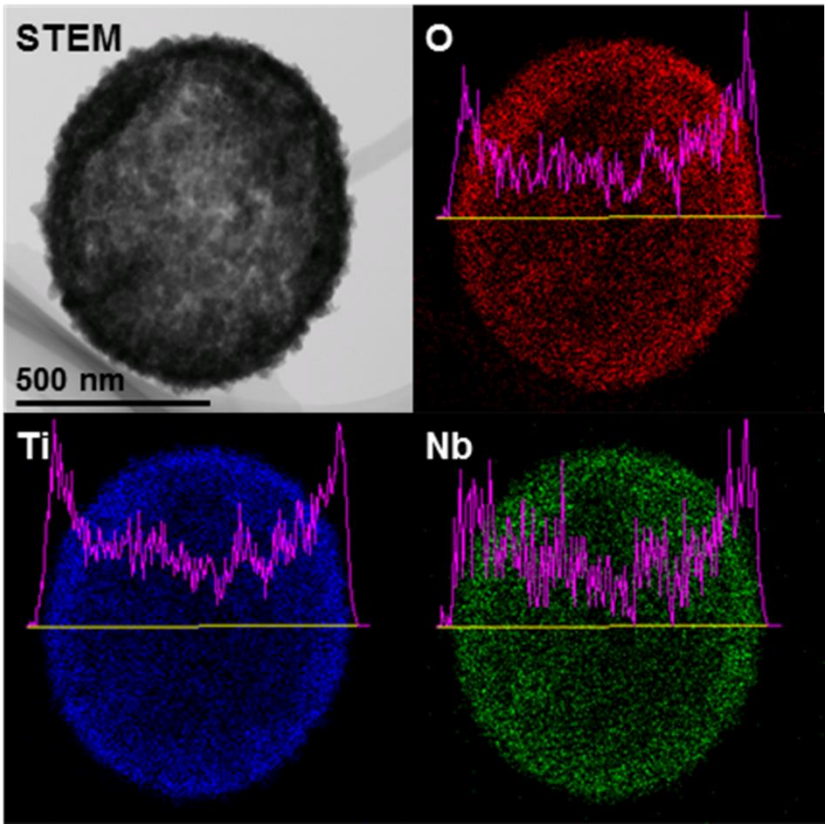

Figure 2–15. EDX mapping and line-scan of the prepared TiO_2–Nb_2O_5-50 MARIMO.

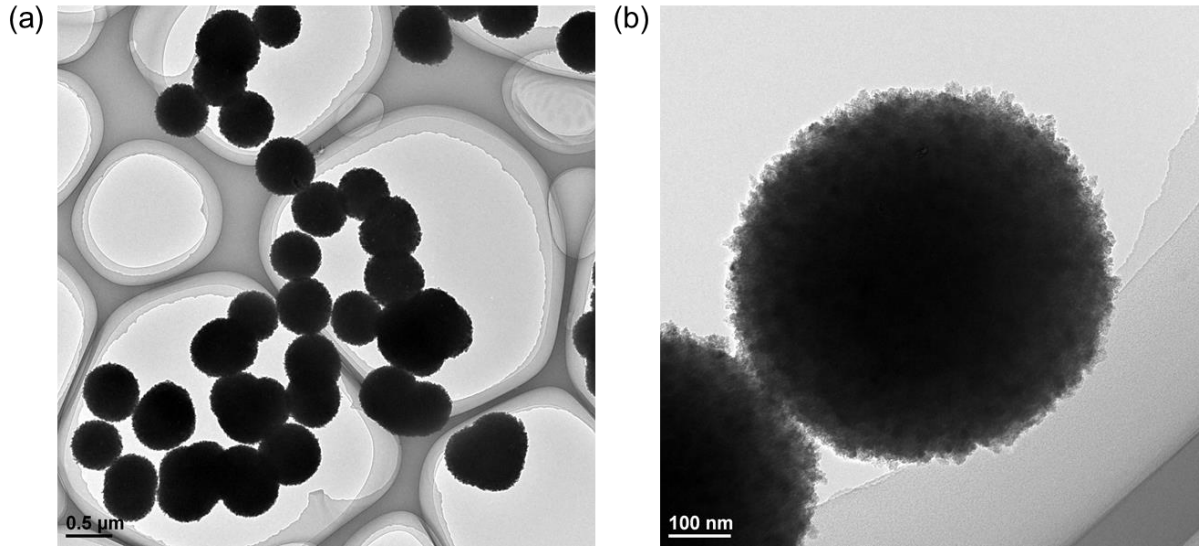

Figure 2–16. TEM images of the prepared solid TiO_2–Nb_2O_5-50 MARIMO.

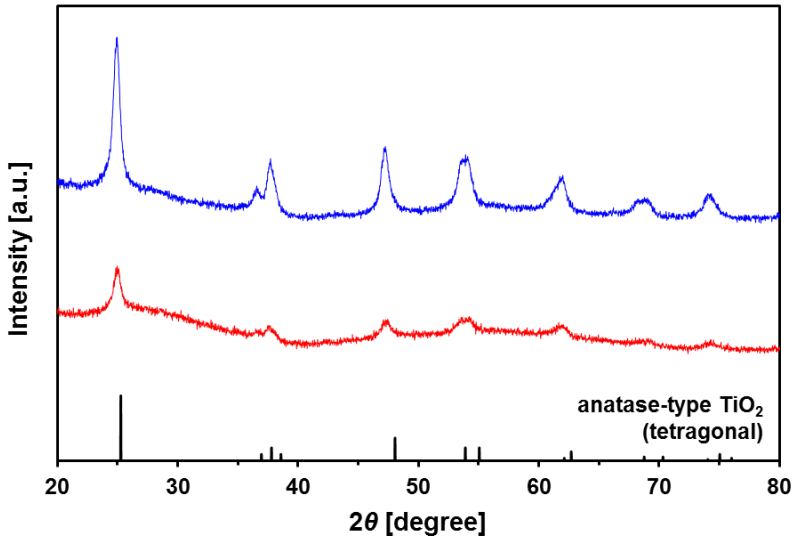

Figure 2–17. XRD patterns of the powdery products with different solvothermal-reaction time (blue, 10 min; red, 0 min).

2–3–3. Formation of $TiNb_2O_7$ MARIMO by crystallization of amorphous TiO_2–Nb_2O_5 composite MARIMO

$TiNb_2O_7$ as an anode material for lithium ion batteries has a high theoretical capacity of 387.6 mA·h/g derived from its 5-electron transfer mechanism (Ti^{4+}/Ti^{3+}, Nb^{5+}/Nb^{4+}, and Nb^{4+}/Nb^{3+}). This value is approximately two times higher than that of the commonly used $Li_4Ti_5O_{12}$ (175 mA·h/g).[36] Thus, $TiNb_2O_7$ has attracted significant attention is promising for application in electric vehicles.[23,33,34] However, $TiNb_2O_7$ suffers from low ionic and electric conductivity. Tailoring special nanostructures of $TiNb_2O_7$ can be used to harness the advantages of nanomaterials, including high electrode/electrolyte contact area and short ion diffusion distances. In particular, microscale spherical materials with hierarchical nanoscale structure are promising for solving the drawbacks of pure nanoscale porous materials with low tap densities and poor Coulombic efficiency. Although, the syntheses of $TiNb_2O_7$ porous spheres have been previously reported, those with larger surface areas remain elusive (Table 2–2). Thus, to obtain $TiNb_2O_7$ porous spheres with large surface area, the synthetic conditions of the precursor composite TiO_2–Nb_2O_5 as well as the calcination conditions were closely examined.

Table 2–2. Reaction conditions to synthesize $TiNb_2O_7$ and specific surface area of the products.

Solvent	Ti precursor	Nb precursor	Additive	Solvothermal conditions	Calcination conditions	Specific surface are [m^2/g]	Ref.
isopropyl alcohol	$Ti(O^nBu)_4$	$Nb(OEt)_5$	diethylenetriamin	200 °C, 12 h	700 °C, 5 h	25.2	41
ethanol	$Ti(O^iPr)_4$	$NbCl_5$	–	200 °C, 24 h	700 °C, 2 h	25.3	42
ethanol	$Ti(O^nBu)_4$	$NbCl_5$	Block copolymer Pluronic P123	220 °C, 16 h	800 °C, 5 h	23.4	43
isopropyl alcohol	$Ti(O^iPr)_4$	$NbCl_5$	Glycerol	180 °C, 24 h	750 °C, 12 h	22.2	44
isopropyl alcohol	$Ti(O^iPr)_4$	$NbCl_5$	diethylenetriamin	200 °C, 24 h	800 °C, 10 h	14.3	45

First, a similar alcothermal treatment of a 1 : 2 (mol ratio) $Ti(O^iPr)_4$ and $Nb(OEt)_5$ mixed methanol solution including formic acid at 300 °C afforded a precursor composite MARIMO with tetragonal (anatase-type) TiO_2 and amorphous Nb_2O_5 as determined from its XRD diffraction pattern (Figure 2–18, blue line). The corresponding SEM images revealed characteristically large primary particles on the MARIMO surface (Figure 2–19a-i). The second step involved calcination of the precursor MARIMO at 700 °C for 2 h and yielded monoclinic $TiNb_2O_7$ MARIMO (Figures 2–19a-ii and 2–20a). However, the XRD patterns showed that the calcined MARIMO contained mainly monoclinic $TiNb_2O_7$ with a small amount of tetragonal (anatase-type) TiO_2 and orthorhombic Nb_2O_5. This indicates that a pure $TiNb_2O_7$ MARIMO was not afforded by the calcination of the as-synthesized TiO_2–Nb_2O_5 MARIMO obtained at 300 °C (Figure 2–20b).

Therefore, amorphous TiO_2–Nb_2O_5 composite MARIMO was selected as an alternative precursor (Figures 2–18, red line and 2–19b-i). The material was prepared using a lower

temperature (200 °C) alcothermal reaction. As shown in Figure 2–21a, calcination of the amorphous TiO_2–Nb_2O_5 composite MARIMO at >600 °C for 2 h produced the desired $TiNb_2O_7$ MARIMO with a pure monoclinic phase. In addition, tetragonal (anatase-type) TiO_2 and orthorhombic Nb_2O_5 peaks were not observed even in case of the obtained sample at 700 °C (Figure 2–20b). Fringe structures were observed in the HR-TEM image (Figure 2–21b-i) of the primary particles, clearly showing that the MARIMO was composed single crystals of $TiNb_2O_7$. The $TiNb_2O_7$ porous morphology was clearly demonstrated by high angle annular dark-field scanning transmission electron microscopy (HAADF-STEM; Figure 2–21b-ii). The specific surface area of the obtained monoclinic $TiNb_2O_7$ MARIMO was smaller (50 m^2/g) than that before calcination (Figure 2–22a-i, 497 m^2/g), but 50 m^2/g is the highest value reported for this type of material to the best of our knowledge (Figure 2–22b-i and Table 2–2). As expected, the average pore size was enlarged from 2.5 to 8.8 nm (Figure 2–22a-ii and b-ii), which is favorable for guest materials to access deep into the porous spheres. In addition, the pore space between the $TiNb_2O_7$ MARIMO can buffer volume changes derived from the phase transitions occurring during lithiation/delithiation, which may result in good cycling performance *via* enhanced structural stability.[45] Thus, $TiNb_2O_7$ porous spheres were successfully prepared with a monoclinic crystal phase and wide pores by calcination of the amorphous TiO_2–Nb_2O_5 composite MARIMO precursor.

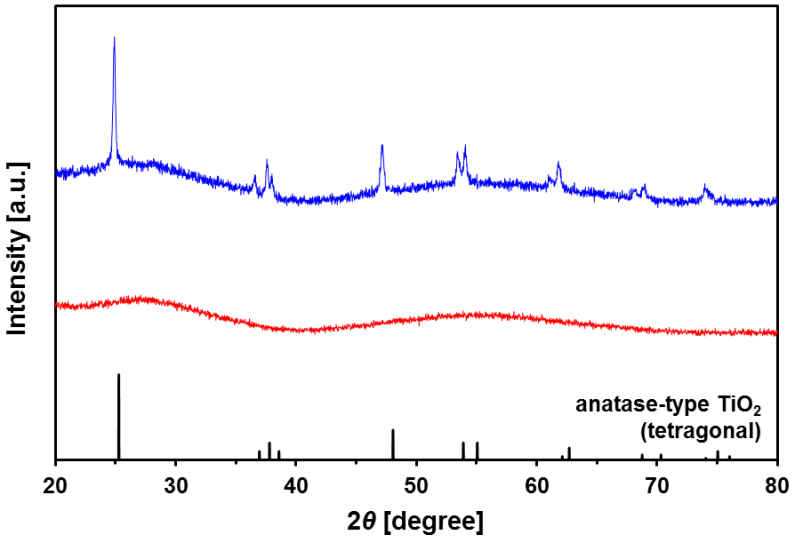

Figure 2–18. XRD patterns of the obtained powdery products prepared with different solvothermal-reaction temperature and time (blue, 300 °C 10 min; red, 200 °C 3 h).

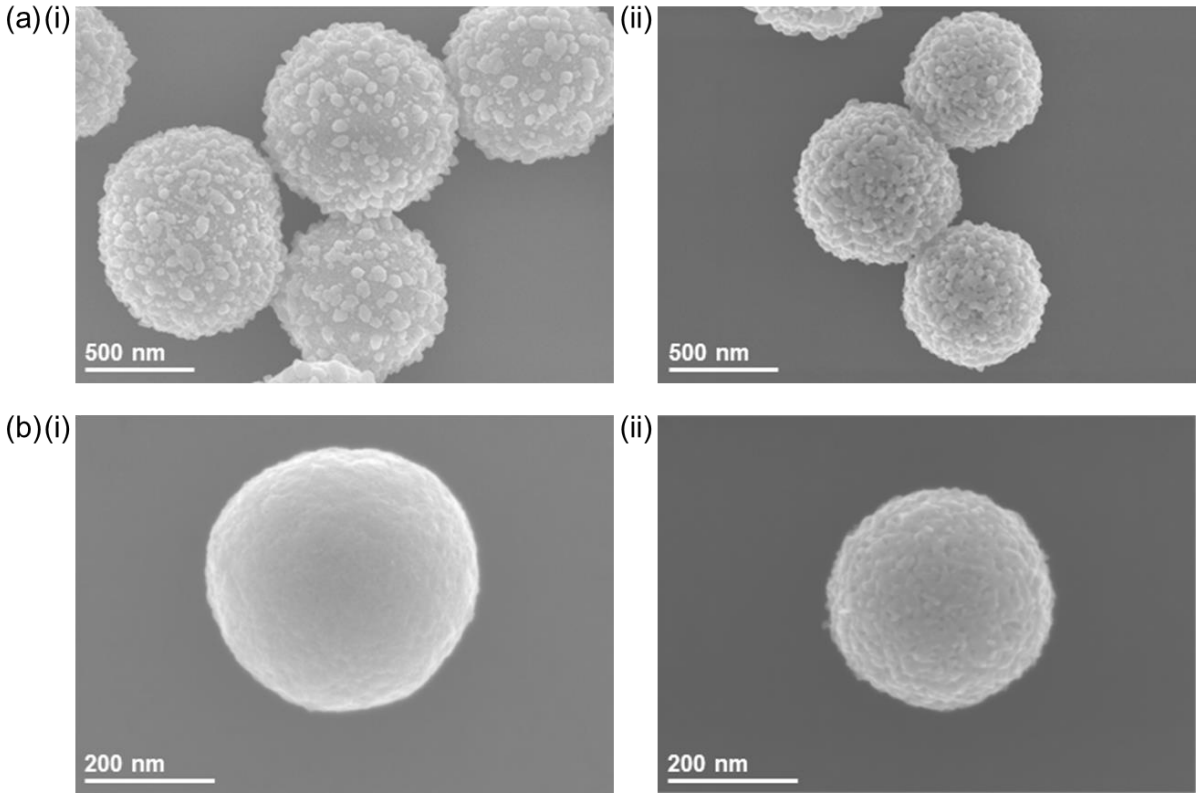

Figure 2–19. SEM images of the $TiNb_2O_7$ MARIMO (a) obtained by the synthesis at 300 °C and (b) at 200 °C in the synthesis process; (i) as-synthesized and (ii) after calcination at 700 for 2h.

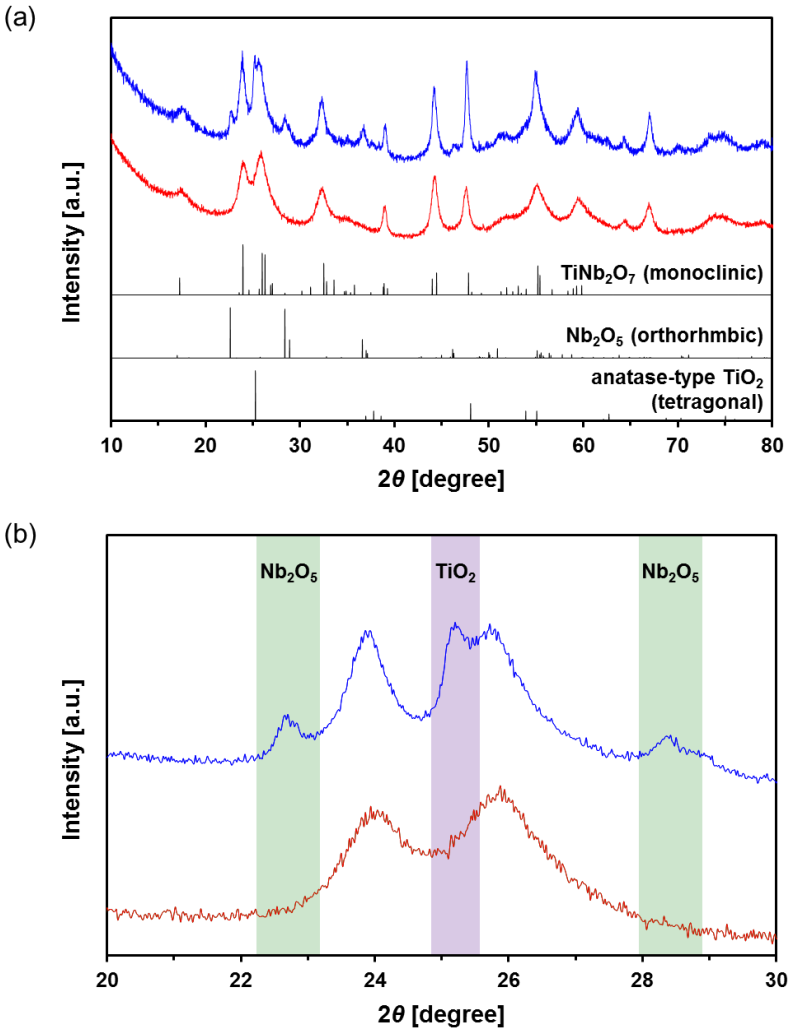

Figure 2–20. XRD diffraction patterns of the $TiNb_2O_7$ MARIMO obtained by calcination of different precursor MARIMOs (blue, crystallized MARIMO; red, amorphous MARIMO). The 2θ range: (a) 10−80° and (b) 20−30° (green, orthorhombic Nb_2O_5; purple, tetragonal TiO_2).

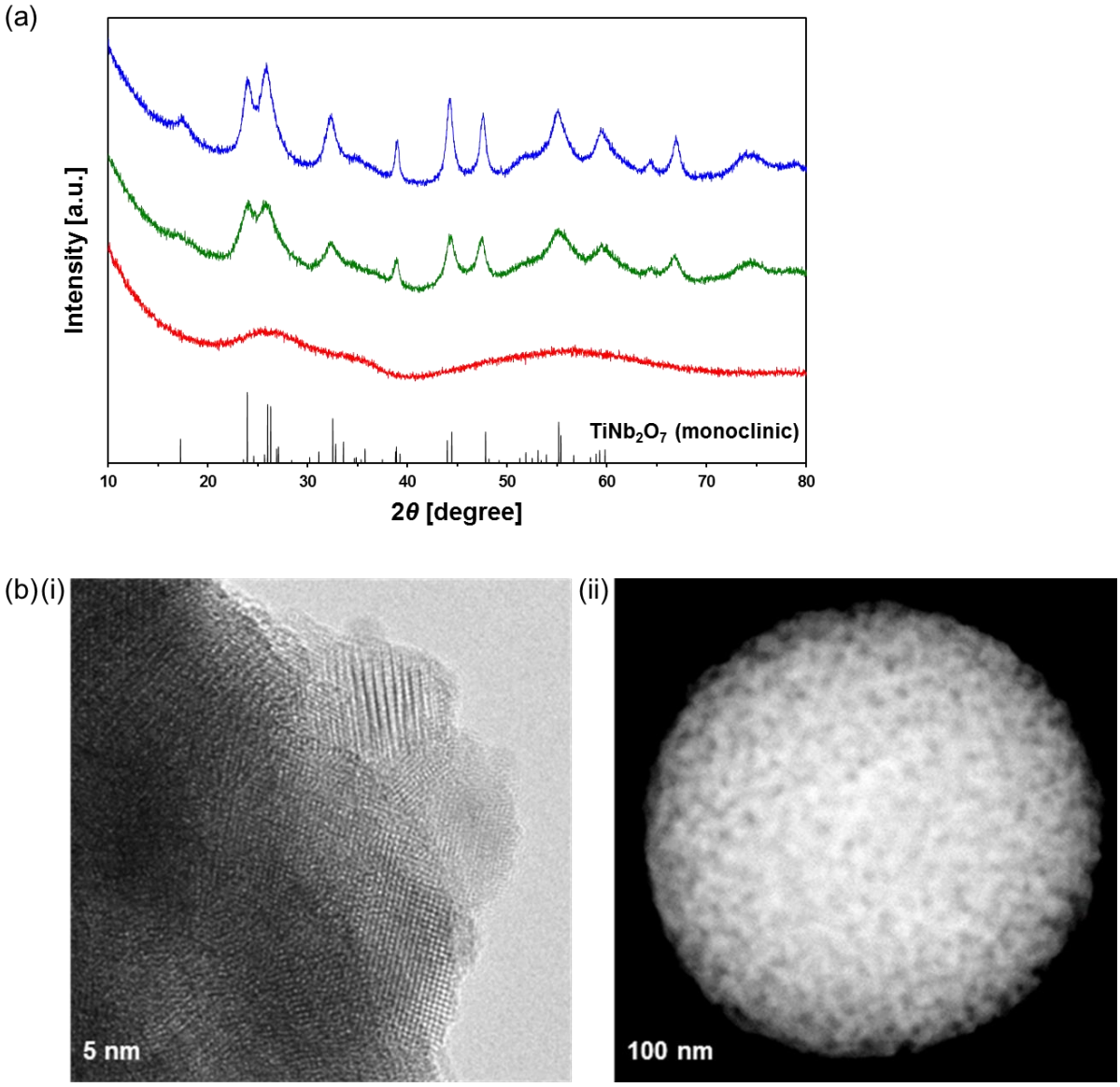

Figure 2–21. (a) XRD patterns of the calcined amorphous TiO_2–Nb_2O_5 composite MARIMO at 500–700 °C (blue, 700 °C; green, 600 °C; red, 500 °C). (b) HR-TEM (i) and HAADF-STEM (ii) images of the amorphous TiO_2–Nb_2O_5 composite MARIMO calcined at 600 °C.

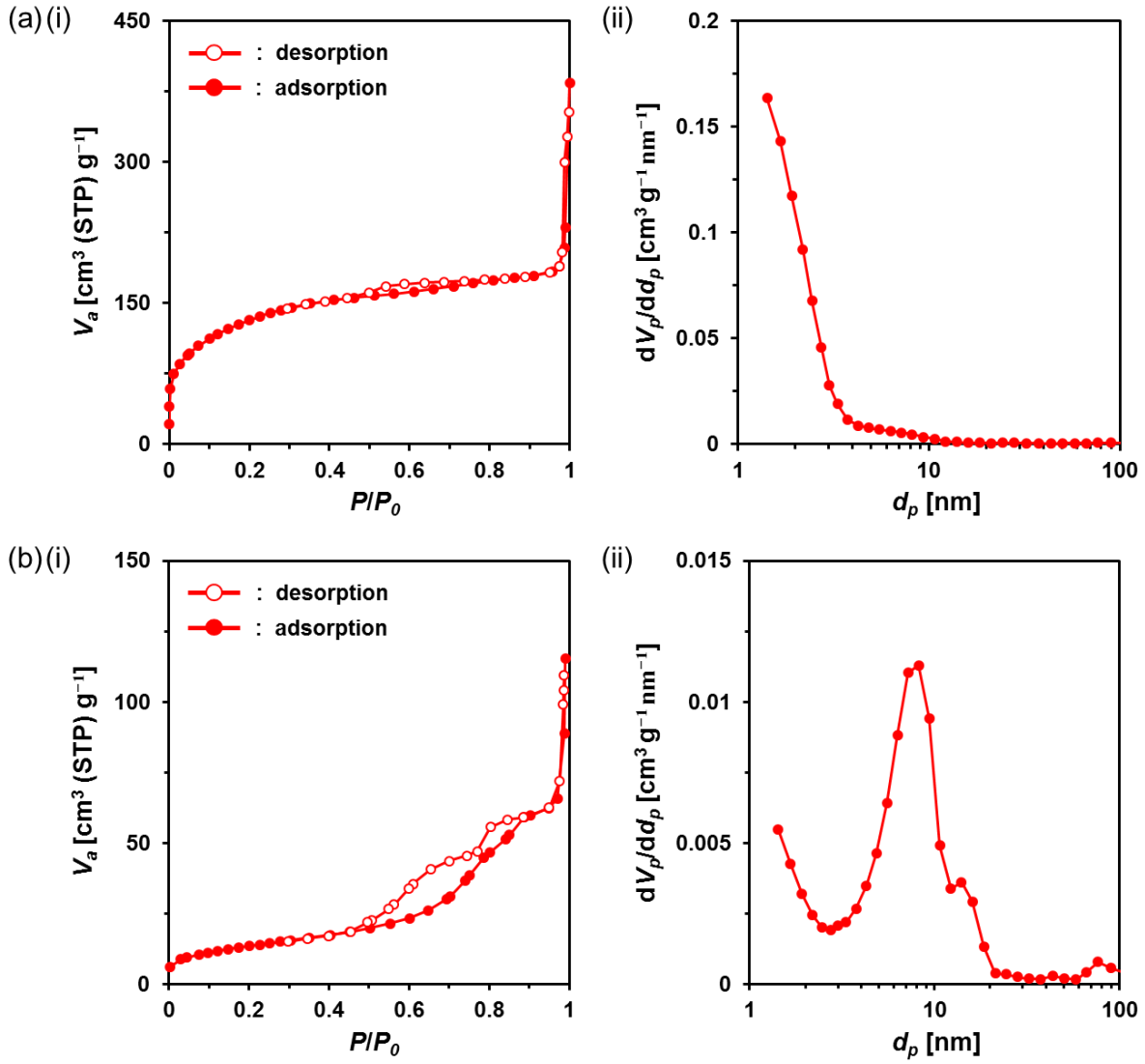

Figure 2–22. (i) Nitrogen adsorption-desorption isotherms and (ii) pore size distributions of (a) the amorphous TiO_2–Nb_2O_5 composite MARIMO and (b) the $TiNb_2O_7$ MARIMO.

2–4. Conclusions

Monodispersed Nb_2O_5 porous spheres (Nb_2O_5 MARIMO) with 630 nm in diameter were prepared *via* the simple alcothermal reaction of a methanol solution of $Nb(OEt)_5$ with formic acid. The crystallinity and pore size of the prepared Nb_2O_5 MARIMO were improved by prolonging the reaction time or simple calcination of the product. TiO_2–Nb_2O_5 composite MARIMO was obtained using a similar alcothermal reaction of $Ti(O^iPr)_4$, $Nb(OEt)_5$, and formic acid in methanol, with a product Ti:Nb atomic ratio that was controlled by changing molar ratio of $Ti(O^iPr)_4$ and $Nb(OEt)_5$ in the precursor solution. A two-step synthetic approach for the generation of $TiNb_2O_7$ porous spheres was developed *via* an alcothermal treatment of a 1:2 (molar ratio) mixed solution of $Ti(O^iPr)_4$ and $Nb(OEt)_5$ in methanol followed by simple calcination. Considering the fact that the obtained submicron-sized porous spheres of niobia and their composites have a large surface area, and high performance can be expected in the field of catalysts and batteries. To evaluate catalyst and battery performance, the research for a practical application is undergoing.

References

1. Valtchev, V.; Tosheva, L. Porous nanosized particles: preparation, properties, and applications. *Chem. Rev.* **2013**, *113*, 6734–6760.
2. Boyjoo, Y.; Wang, M.; Pareek, V. K.; Liu, J.; Jaroniec, M. Synthesis and applications of porous non-silica metal oxide submicrospheres. *Chem. Soc. Rev.* **2016**, *45*, 6013–6047.
3. Varma, A.; Mukasyan, A.; Rogachev, A.; Manukyan, K. V. Solution combustion synthesis of nanoscale materials. *Chem. Rev.* **2016**, *116*, 14493–14586.
4. Qiu, H.-J.; Peng, L.; Li, X.; Xu, H. T.; Wang, Y. Using Corrosion to fabricate various nanoporous metal structures. *Corros. Sci.* **2015**, *92*, 16–31.
5. Lahiri, A.; Endres, F. Review-electrodeposition of nanostructured materials from aqueous, organic and ionic liquid electrolytes for Li-ion and Na-ion batteries: A comparative review. *J. Electrochem. Soc.* **2017**, *164*, 597–612.
6. Leng, J.; Wang, Z.; Wang, J.; Wu, H.-H.; Yan, G.; Li, X.; Guo, H.; Liu, Y.; Zhang, Q.; Guo, Z. Advances in nanostructures fabricated via spray pyrolysis and their applications in energy storage and conversion. *Chem. Soc. Rev*. **2019**, *48*, 3015–3072.
7. Danks, A. E.; Hall, S. R.; Schnepp, Z. The evolution of 'sol–gel' chemistry as a technique for materials synthesis. *Mater. Horiz.* **2016**, *3*, 91–112.
8. Lane, M. K. M.; Zimmerman, J. B.; Controlling metal oxide nanoparticle size and shape with supercritical fluid synthesis. *Green Chem.* **2019**, *21*, 3769–3781.
9. Wang, P.; Ueno, K.; Takigawa, H.; Kobiro, K. Versatility of one-pot, single-step synthetic approach for spherical porous (metal) oxide nanoparticles using supercritical alcohols. *J. Supercrit. Fluids* **2013**, *78*, 124–131.
10. Pradeep, E. K. C.; Habu, T.; Tooriyama, H.; Ohtani, M.; Kobiro, K. Ultra-simple synthetic approach to the fabrication of CeO_2–ZrO_2 mixed nanoparticles into homogeneous, domain,

and core–shell structures in mesoporous spherical morphologies using supercritical alcohols. *J. Supercrit. Fluids* **2015**, *97*, 217–223.

11. Pradeep, E. K. C.; Ohtani, M.; Kobiro, K. A simple synthetic approach to Al_2O_3–TiO_2 and ZnO–TiO_2 mesoporous hollow composite assemblies consisting of homogeneously mixed primary particles at the nano level. *Eur. J. Inorg. Chem.* **2015**, 5621–5627.
12. Nguyen, H. T. T.; Habu, T.; Ohtani, M.; Kobiro, K. One-pot direct synthesis of SiO_2–TiO_2 composite nanoparticle assemblies with hollow spherical morphology. *Eur. J. Inorg. Chem.* **2017**, 3017–3023.
13. Ohtani, M.; Muraoka, T.; Okimoto, Y.; Kobiro, K. Rapid one-pot solvothermal batch synthesis of porous nanocrystal assemblies composed of multiple transition-metal elements. *Inorg. Chem.* **2017**, *56*, 11546–11551.
14. Furukawa, S.; Ohno, Y.; Shishido, T.; Teramura, K.; Tanaka, T. Selective amine oxidation using Nb_2O_5 photocatalyst and O_2. *ACS Catal.* **2011**, *1*, 1150–1153.
15. Liu, H.; Gao, N.; Liao, M. Y.; Fang, X. S. Hexagonal-like Nb_2O_5 nanoplates-based photodetectors and photocatalyst with high performances. *Sci. Rep.* **2015**, *5*, 7716.
16. Siddiki, S. M. A. H.; Rashed, Md. N.; Ali, Md. A.; Toyao, T.; Hirunsit, P.; Ehara, M.; Shimizu, K. Lewis acid catalysis of Nb_2O_5 for reactions of carboxylic acid derivatives in the presence of basic inhibitors. *ChemCatChem* **2018**, *10*, 1–15.
17. Komanoya, T.; Kinemura, T.; Kita, Y.; Kamata, K.; Hara, M. Electronic effect of ruthenium nanoparticles on efficient reductive amination of carbonyl compounds. *J. Am. Chem. Soc.* **2017**, *139*, 11493–11499.
18. Gnanakumar, E. S.; Chandran, N.; Kozhevnikov, I. V.; Grau-Atienza, A.; Fernandez, E. V. R.; Sepulveda-Escribano, A.; Shiju, N. R. Highly efficient nickel-niobia composite catalysts for hydrogenation of CO_2 to methane. *Chem. Eng. Sci.* **2019**, *194*, 2–9.
19. Deng, Q.; Fu, Y.; Zhu, C.; Yu, Y. Niobium-based oxides toward advanced electrochemical

energy storage: recent advances and challenges. *Small* **2019**, *15*, 1804884.

20. Rani, R. A.; Zoolfakar, A. S.; O'Mullane, A. P.; Austin, M. W.; Zadeh, K. K. Thin films and nanostructures of niobium pentoxide: fundamental properties, synthesis methods and applications. *J. Mater. Chem. A* **2014**, *2*, 15683–15703.
21. Li, C. C.; Dou, J.; Chen, L. W.; Lin, J. Y.; Zeng, H. C. Antisolvent precipitation for the synthesis of monodisperse mesoporous niobium oxide spheres as highly effective solid acid catalysts. *ChemCatChem* **2012**, *4*, 1675–1682.
22. Li, L.; Deng, J.; Yu, R.; Chen, J.; Wang, Z.; Xing, X. Niobium pentoxide hollow nanospheres with enhanced visible light photocatalytic activity. *J. Mater. Chem. A* **2013**, *1*, 11894–11900.
23. Dai, Z. F.; Dai, H.; Zhou, Y.; Liu, D. L.; Duan, G. T.; Cai, W. P.; Li, Y. Monodispersed Nb_2O_5 microspheres: facile synthesis, air/water interfacial self-assembly, Nb_2O_5-based composite films, and their selective NO_2 sensing. *Adv. Mater. Interfaces* **2015**, *2*, 1500167.
24. Zhang, H.; Wu, Q.; Guo, C.; Wu, Y.; Wu, T. Photocatalytic selective oxidation of 5-hydroxymethylfurfural to 2,5-diformylfuran over Nb_2O_5 under visible light. *ACS Sustainable Chem. Eng.* **2017**, *5*, 3517–3523.
25. Nakajima, K.; Hirata, J.; Kim, M.; Gupta, N. K.; Murayama, T.; Yoshida, A.; Hiyoshi, N.; Fukuoka, A.; Ueda, W. Facile formation of lactic acid from a triose sugar in water over niobium oxide with a deformed orthorhombic phase. *ACS Catal.* **2018**, *8*, 283–290.
26. Xue, J.; Wang, R.; Zhang, Z.; Qiu, S. Facile preparation of C, N co-modified Nb_2O_5 nanoneedles with enhanced visible light photocatalytic activity. *Dalton Trans.* **2016**, *45*, 16519–16525.
27. Chen, J.; Wang, H.; Huang, G.; Zhang, Z.; Han, L.; Song, W.; Li, M.; Zhang, Y. Facile synthesis of urchin-like hierarchical Nb_2O_5 nanospheres with enhanced visible light photocatalytic activity. *J. Alloys Compd.* **2017**, *728*, 19–28.

28. Ko, E. I.; Weissman, J. G. Structures of niobium pentoxide and their implications on chemical behavior. *Catal. Today* **1990**, *8*, 27–36.
29. Kominami, H.; Oki, K.; Kohno, M.; Onoue, S.; Kera, Y.; Ohtani, B. Novel solvothermal synthesis of niobium(V) oxide powders and their photocatalytic activity in aqueous suspensions. *J. Mater. Chem.* **2001**, *11*, 604–609.
30. Li, G.; Zhang, X.; Lu, H.; Tan, C.; Chen, K.; Lu, H.; Gao, J.; Yang, Z.; Zhu, G.; Wang, G.; He, Z. Ethanol sensing properties and reduced sensor resistance using porous Nb_2O_5–TiO_2 n-n junction nanofibers. *Sens. Actuators, B* **2019**, *283*, 602–612.
31. Kong, L.; Wang, C.; Zheng, H.; Zhang, X.; Liu, Y. Defect-induced yellow color in Nb-doped TiO_2 and its impact on visible-light photocatalysis. *J. Phys. Chem. C* **2015**, *119*, 16623–16632.
32. Akizuki, M.; Oshima, Y. Acid catalytic properties of TiO_2, Nb_2O_5, and NbO_x/TiO_2 in supercritical water. *J. Supercrit. Fluids* **2018**, *141*, 173–181.
33. Lou, S.; Zhao, Y.; Wang, J.; Yin, G.; Du, C.; Sun, X. Ti-based oxide anode materials for advanced electrochemical energy storage: lithium/sodium ion batteries and hybrid pseudocapacitors. *Small* **2019**, *15*, 1904740.
34. Ma, J.; Guo, X.; Xue, H.; Pan, K.; Liu, C.; Pang, H. T. Niobium/tantalum-based materials: synthesis and applications in electrochemical energy storage. *Chem. Eng. J.* **2020**, *380*, 122428.
35. Usui, H.; Yoshioka, S.; Wasada, K.; Shimizu, M.; Sakaguchi, H. Nb-doped rutile TiO_2: a potential anode material for Na-ion battery. *ACS Appl. Mater. Interfaces* **2015**, *7*, 6567–6573.
36. Han, J.-T.; Huang, Y.-H.; Goodenough, J. B. New anode framework for rechargeable lithium batteries. *Chem. Mater.* **2011**, *23*, 2027–2029.
37. Lv, Y.; Cai, B.; Ma, Q.; Wang, Z.; Liu, J.; Zhang, W.-H. Highly crystalline Nb-doped TiO_2

nanospindles as superior electron transporting materials for high-performance planar structured perovskite solar cells. *RSC Adv.* **2018**, *8*, 20982–20989.

38. Yang, H. G.; Zeng, H. C. Preparation of hollow anatase TiO_2 nanospheres *via* ostwald ripening. *J. Phys. Chem. B* **2004**, *108*, 3492–3495.
39. Wang, X.; Feng, J.; Bai, Y.; Zhang, Q.; Yin, Y. Synthesis, properties, and applications of hollow micro-/nanostructures. *Chem. Rev.* **2016**, *116*, 10983–11060.
40. Prieto, G.; Tüysüz, H.; Duyckaerts, N.; Knossalla, J.; Wang, G.-H.; Schüth, F. Hollo nano- and microstructures as catalysts. *Chem. Rev.* **2016**, *116*, 14056–14119.
41. Yu, L.; Hu, H.; Wu, H. B.; Lou, X. W. Complex hollow nanostructures: synthesis and energy-related applications. *Adv. Mater.* **2017**, *29*, 1604563.
42. Park, H.; Wu, H. B.; Song, T.; Paik, U. Porosity-controlled TiNb2O7 microspheres with partial nitridation as a practical negative electrode for high-power lithium-ion batteries. *Adv. Energy Mater.* **2015**, *5*, 1401945.
43. Li, H.; Shen, L.; Pang, G.; Fang, S.; Luo, H.; Yang, K.; Zhang, X. $TiNb_2O_7$ nanoparticles assembled into hierarchical microspheres as high-rate capability and long-cycle-life anode materials for lithium ion batteries. *Nanoscale* **2015**, *7*, 619–624.
44. Cheng, Q.; Liang, J.; Lin, N.; Guo, C.; Zhu, Y.; Qian, Y. Porous $TiNb_2O_7$ nanospheres as ultra long-life and high-power anodes for lithium-ion batteries. *Electrochim. Acta* **2015**, *176*, 456–462.
45. Liu, G.; Zhao, L.; Sun, R.; Chen, W.; Hu, M.; Liu, M.; Duan, X.; Zhang, T. Mesoporous $TiNb_2O_7$ microspheres as high performance anode materials for lithium-ion batteries with high-rate capability and long cycle-life. *Electrochim. Acta* **2018**, *259*, 20–27.

Chapter III.

Rapid one-pot synthesis of ultrafine titania nanocrystals and their conversion into transparent mesoporous thin layer films

3–1. Introduction

Controlling the size and morphology of inorganic nanocrystals is an important aspect of improving certain intrinsic characteristics, such as electronic, magnetic, photophysical, and catalytic properties.[1,2] Over the past decade, considerable effort has been devoted to developing new methods for the synthesis of unique nanomaterials having well-controlled sizes and specific morphologies.[3,4] The precise synthesis of titania nanocrystals has been intensively researched owing to the potential applications of this oxide in energy storage, photocatalysts, solar cells, and other optoelectronic devices.[5–9]

A wide variety of solution-based techniques based on sol–gel, co-precipitation, hydrothermal, and solvothermal processes have been developed for the synthesis of nanocrystalline TiO_2.[10,11] Although these conventional approaches are able to synthesize TiO_2 crystals from 10 to 50 nm in size, there remains a need for an efficient method capable of generating crystals in sizes less than 5 nm. The synthesis of ultrafine TiO_2 nanocrystals is quite difficult as a result of sintering of the primary particles during the high-temperature reaction and/or the post annealing process. Several approaches have recently been reported as potential means of overcoming the limitations of the present-day methods.[12] Pioneering techniques meant to address this challenge include the use of self-assembled molecular cages[13] and dendrimers[14] as sacrificial templates. However, much simpler synthetic methodologies are desirable based on practical considerations.

Recently, we have successfully synthesized porous spherical nanocrystal assemblies

having extremely wide surface area by our original one-pot and single-step solvothermal method.[15–22] The key factor to yield such porous spherical morphology is to control solvolysis rate of metal alkoxide in the precursor solutions under solvothermal conditions. For example, we chose carboxylic acid as additives for the preparation of titania nanocrystal assembles. As a result, we have controlled the resultant morphologies of the solid or hollow porous nanomaterials by changing the carboxylic acid as an additive. However, the relationships between the resultant material morphology and chemical structure of carboxylic acid as an additive have yet to be well understood.

In this chapter, a simple, one-pot approach to producing ultrafine titania nanocrystals, using a rapid heating technique in conjunction with a solvothermal reaction using aliphatic carboxylic acid were reported. This rapid heating method enhances the nucleation and crystal growth of the nanocrystals, thus avoiding undesired sintering during the high temperature solvothermal reaction and ensuring sub-5 nm sized nanocrystals.

3–2. Experiment

3–2–1. Materials

Methanol, hexane, toluene, oleic acid, linoleic acid, oleylamine, titanium tetrabutoxide [$Ti(O^nBu)_4$], ascorbic acid, potassium bromide (KBr), and potassium chloride (KCl) were purchased from FUJIFIM Wako Pure Chemical Corporation. Octanoic acid was purchased from Tokyo Chemical Industry Co., Ltd. Commercial titania powder (Degussa P25 TiO_2) was obtained from Nippon Aerosil Co., Ltd. All the reagents used as received, unless otherwise noted.

3–2–2. Synthetic procedure

Synthesis of titania nanocrystals. Titania nanocrystals were synthesized by using liquid mixtures of titanium alkoxide and oleic acid as precursor solutions. For example, adequate amounts of $Ti(O^nBu)_4$ (125 μL, 0.35 mmol) and oleic acid (3.5 mL, 11.1 mmol) were mixed in a glass vial. The resultant precursor solution was transferred to an SUS-316 stainless steel tubular reactor of 10 mL inner volume, and then, the reactor was sealed with an SUS-316 screw cap. The sealed reactor was placed in a pre-heated molten-salt bath, which was heated to and maintained at 300 ˚C for 10 min. In the present experimental conditions, maximum heating rate is reached to 500 ºC/min. Thus, the inner pressure of the reactor is drastically increasing within 30 seconds. It should be carefully treated with protection gloves, lab coat, and eye shield to avoid unexpected accident. After certain time period, the reaction was immediately quenched by placing the reactor in an ice-water bath. The obtained precipitates were centrifuged, washed with methanol, and dried under vacuum to give a powdery product.

Preparation of the thin-layer films. The synthesized TiO_2 sample (20 mg) was dispersed in toluene (4 mL). The resultant dispersion was drop-casted on the ITO glass plate (1

cm × 1 cm square), and then calcined in an electric oven under air at 400˚C for 2 h. As a control experiment sample, the commercial TiO_2 (Degussa P25 TiO_2, 5 mg) was prepared by the same manner with methanol (1 mL).

3–2–3. Characterization methods

Transmission electron microscopy. The Transmission electron microscopy (TEM) images were measured on a JEOL JEM-2100F. For the preparation of the specimen, first, the washed sample was dispersed in methanol. Then, 10 μL of resultant dispersion was drop-casted on a carbon-coated copper microgrid and the solvent was vaporized under atmospheric pressure.

Scanning electron microscopy. Scanning electron microscopy (SEM) was performed using a Hitachi SU8020 FE-SEM. A specimen was prepared by drop-casting of the sample dispersion on a silicon wafer and calcining at 400 ˚C for 2 h. Energy-dispersive X-ray (EDX) mapping images were obtained from HORIBA X-max EDX spectrometer.

X-ray diffraction measurements. X-ray diffraction (XRD) patterns were obtained using a Rigaku SmartLab diffractometer with graphite-monochromatized Cu Kα radiation (X-ray wavelength: 1.5418 Å) in steps of 0.02° over the 2θ range of 10−90°. The powdery samples were set on a non-refractive silicon holder (Overseas X-Ray Service, Japan).

Infrared spectroscopic measurements. Fourier transform infrared (FT-IR) spectra were recorded using a JASCO FT/IR-480 plus spectrometer. The sample was thoroughly ground and press-molded with KBr.

Thermogravimetric measurements. The thermogravimetric (TG) analysis was measured on a HITACHI STA7200RV. A samples was placed on an open platinum sample pan. The experiments were conducted at 2 °C/min heating rate in air.

Small-angle X-ray scattering measurements. Small-angle X-ray scattering (SAXS) patterns were obtained using a Rigaku SmartLab diffractometer with graphite-monochromatized Cu Kα radiation (X-ray wavelength: 1.5418 Å) in steps of 0.02° over the 2θ range of 0.12−8°. A sample was dispersed in hexane and filled in a glass capillary (ϕ1.0 mm). The measurement was conducted using transmission method. The scattering data was analyzed on the basis of a curve fitting to a cylinder model using Rigaku NANO-Solver Ver. 3.6 (particle size and pore size analysis software).

Nitrogen adsorption-desorption isotherm measurements. Nitrogen adsorption–desorption isotherms were obtained using a Belsorp Mini II (BEL Corp.). For the preparation of the specimen, first, the washed sample was dispersed in hexane and dried in a crucible overnight. Then, it was calcined at 400 °C for 2 h and dried at 250 °C for 6 h under vacuum condition. The specific surface areas were determined using the Brunauer-Emmett-Teller (BET) multipoint method. The average pore size distributions were calculated using the Barrett-Joyner-Halenda (BJH) from the nitrogen adsorption isotherm data.

UV-vis spectroscopic measurements. Transmittance and reflectance spectra of the thin-layer film was measured on a JASCO V-650 spectrophotometer with an integrated sphere attachment. After the first measurement, the process of drop-casting, calcination and measurement was repeated twice using the same glass.

Photocurrent measurements. Photocurrent measurements were performed on EC Frontier ECstat-300 with the standard three-component electrochemical cell composed of a photocatalyst-deposited ITO working, Pt-coil counter, Ag/AgCl reference electrodes. An aqueous solution of ascorbic acid (0.2 mol/L) and KCl (0.1 mol/L) was used as an electrolyte solution. UV irradiation was carried out with 300 W Xenon lamp (MAX-301, Asahi Spectra Co., Ltd.).

3–3. Results and discussion

3–3–1. Synthesis of titania nanocrystals

The nanostructure of the powdery product was confirmed by TEM. Surprisingly, the obtained materials exhibited perfectly uniform sizes and morphologies (Figure 3–1a), with an average particle diameter of 3.0 ± 0.4 nm (Figure 3–1b). Judging from the high-resolution TEM (HR-TEM) images, each product generated a clear lattice fringe with an interplanar distance of 0.19 nm (Figure 3–2), corresponding to the (200) or (020) planes of anatase TiO_2. XRD patterns also demonstrated the presence of an anatase phase, although a bronze phase was present in less than 10 % (Figure 3–3).[23] It is also worth noting that these nanocrystals exhibited a perfect periodic arrangement on the micrometer scale, judging from the wide-range TEM observation shown in Figure 3–1c. The fast Fourier transform (FFT) of the TEM image presented in Figure 3–1d also shows a hexagonal pattern, providing evidence for perfect periodicity in the observed structure. These results show that the present method synthesizes extremely fine and uniformly sized TiO_2 nanocrystals.

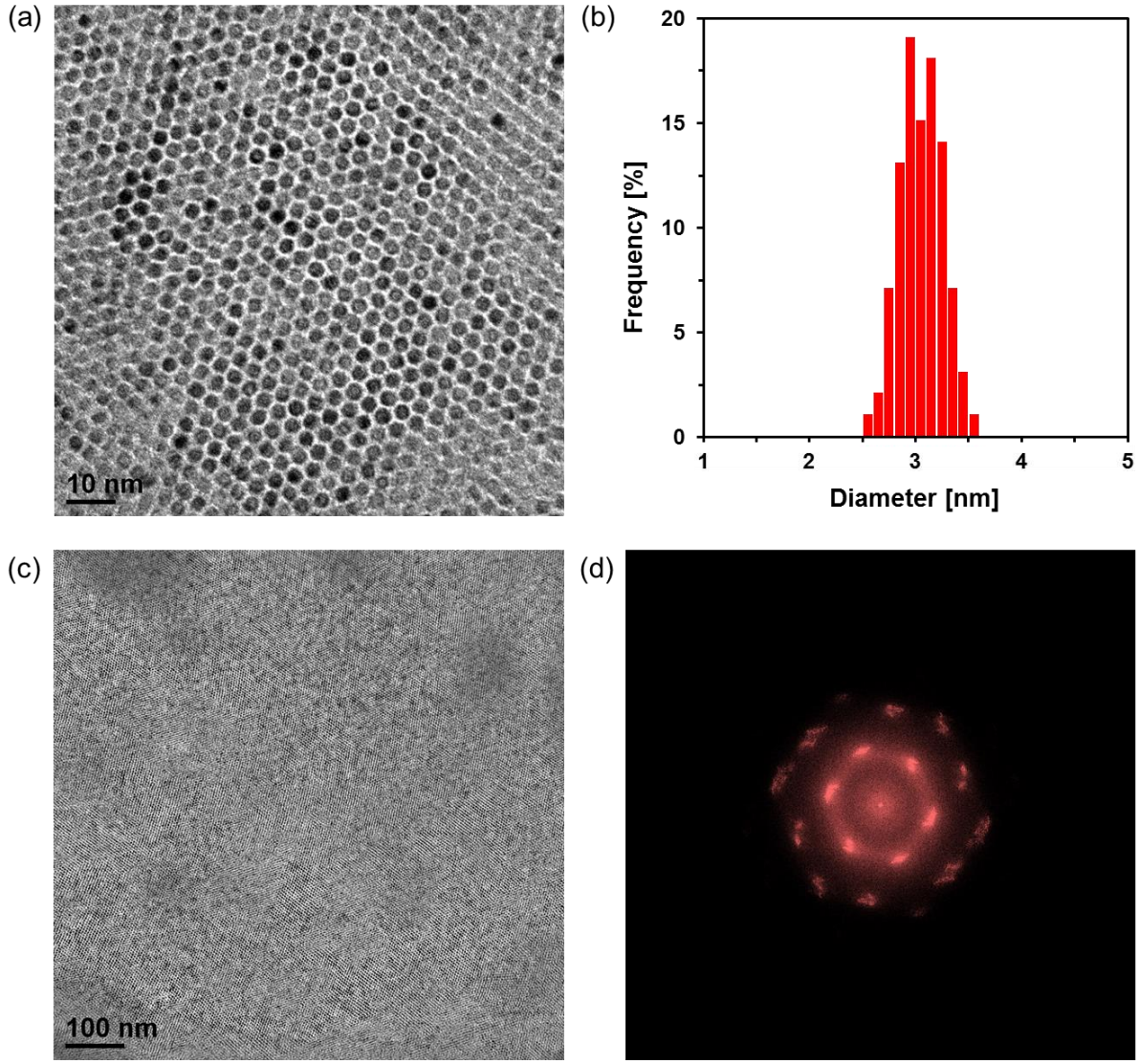

Figure 3–1. (a) TEM image and (b) size distribution histogram of the TiO_2 nanocrystals. The size distribution was evaluated by statistical analyses (N = 100) using selected TEM images. (c) Low magnification TEM image of the periodically aligned TiO_2 nanocrystals. (d) The FFT image derived from the image in (c).

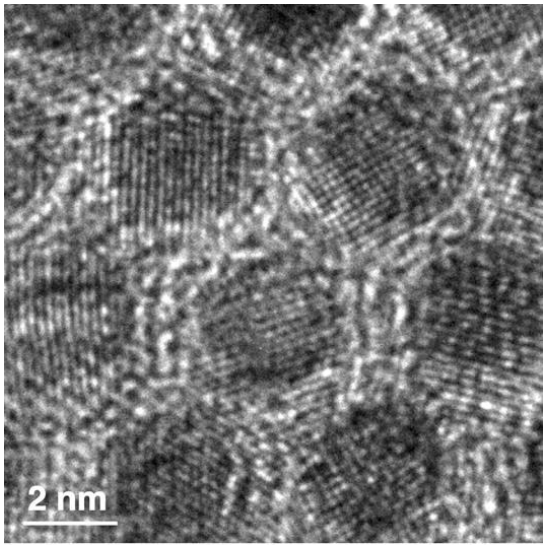

Figure 3–2. HR-TEM image of the obtained TiO_2 nanocrystals (3 nm).

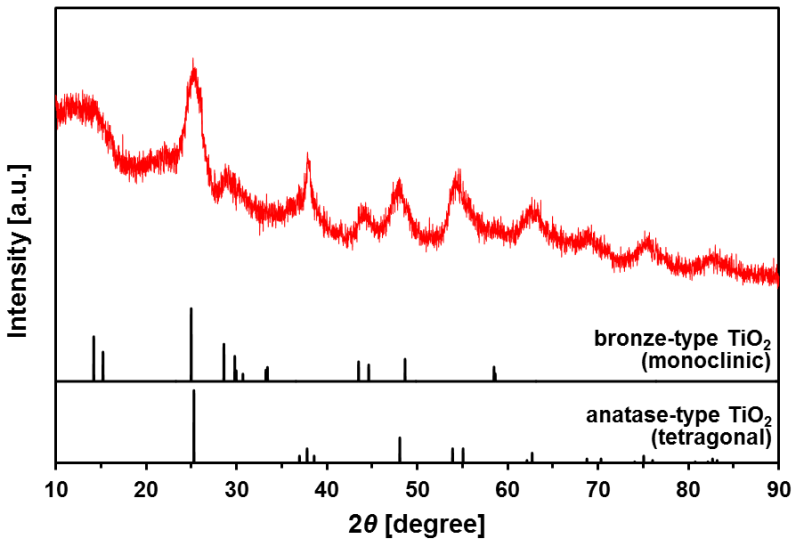

Figure 3–3. XRD patterns of the obtained TiO_2 nanocrystals (3 nm).

3–3–2. Generation mechanism of hexagonal assemblies

To confirm the role of the oleic acid in the formation of these titania nanocrystals, we performed a detailed characterization of the products using FT-IR spectroscopy and TG analysis. As shown in Figure 3–4a, the IR spectra of the powdery product show strong characteristic peaks around 3000 and 1500 cm^{-1}. These peaks can be assigned to antisymmetric and symmetric C–H stretching vibration modes, typically located at 2920 and 2851 cm^{-1}, and antisymmetric and symmetric stretching vibration modes of the COO^- anion on the surface of the TiO_2, located at 1514 and 1427 cm^{-1}, respectively.[24] In addition, the TG data demonstrate a mass loss of approximately 30% in the temperature range from 200 to 400 °C (Figure 3–4b), indicating the inclusion of organic material. These results show that the surfaces of the nanocrystals were covered with oleate anions. The surface covering of oleate anion on the nanocrystals may also contribute the hexagonal periodic alignment of the nanocrystals through the lipophilic interaction between unsaturated aliphatic chains.

As a result of the strong interaction between the oleate anions on the TiO_2 surfaces, the nanocrystals could be redispersed in non-polar solvents, such as hexane and toluene, in a stable manner. This enabled the spectroscopic analysis of the nanocrystal structure using SAXS. Figure 3–4c presents the SAXS profiles for a hexane dispersion of the TiO_2 nanocrystals. Theoretical curve fitting determined that the SAXS profile (the red trace) could be matched to the curve generated using a rod model (black line), indicating that the dispersed TiO_2 nanocrystals had an anisotropic rod structure with a small aspect ratio (length/diameter = 2.5). The average diameter based on calculations using the rod model was estimated to be 3.6 nm (Figure 3–4d). This value is consistent with that derived from the TEM observations in Figure 3–1a. To confirm the formation of an anisotropic rod structure, we performed an acid treatment of the as-prepared TiO_2 nanocrystals to remove the olate anions and then isolated the

nanocrystals. Rod-like nanocrystals were subsequently observed by TEM, as shown in Figure 3–5. This fact is again consistent with the surface covering of olate anion on the TiO_2 nanocrystals through the chemical adsorption.

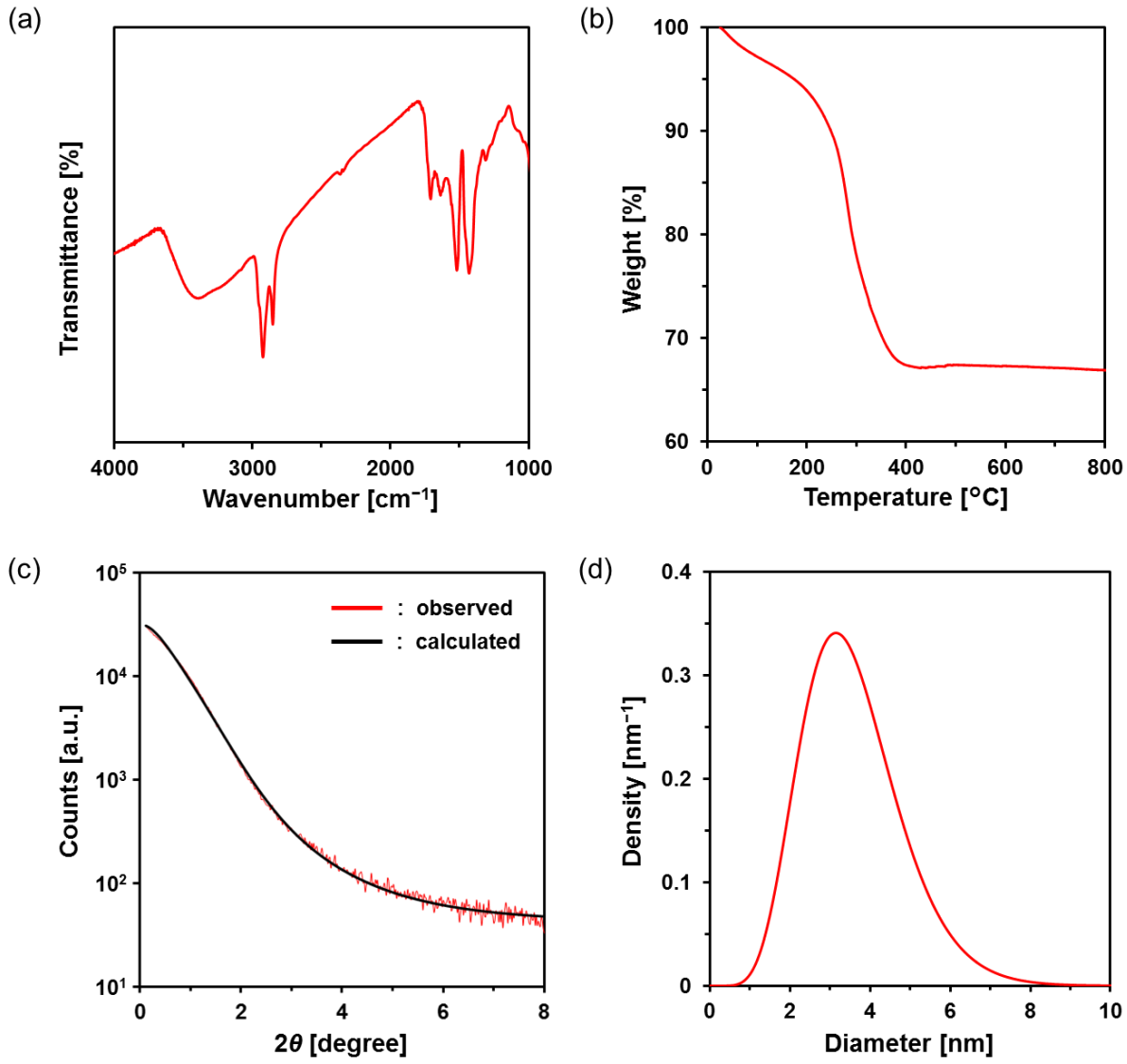

Figure 3–4. (a) FT-IR spectrum of the TiO_2 nanocrystals. (b) TG data for the TiO_2 nanocrystals, measured in air at a heating rate of 2 °C/min. (c) SAXS profile of a hexane dispersion of the TiO_2 nanocrystals (red curve) at 25 °C, and a simulated scattering pattern (black curve). (d) The calculated diameter distribution resulting from the rod model.

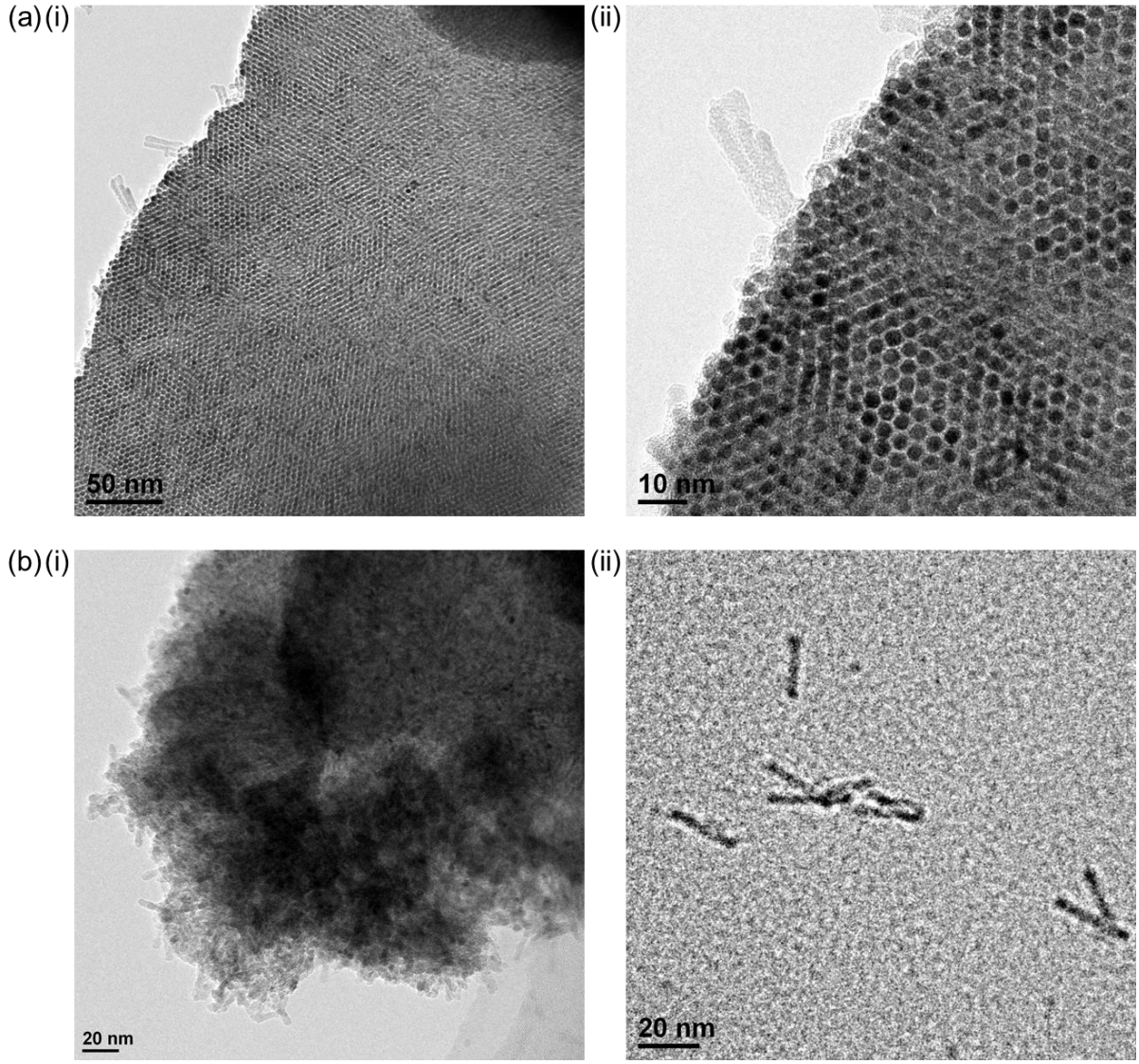

Figure 3–5. TEM images of the TiO_2 nanocrystals (a) before and (b) after washing with 0.1 mol/L HCl aqueous solution: at (i) low magnification and (ii) high magnification.

The factors influencing the formation of the ultrafine nanocrystals were assessed by examining the effect of the heating rate. In comparison with the products obtained from the rapid heating reaction, clear structural differences were observed when using slow heating. The products of the slow heating reaction showed an agglomerated structure (Figure 3–6b) in contrast to the nanocrystals prepared by rapid heating (Figures 3–1a and 3–6a). The maximum reaction temperature also affected the ultrafine structure of the products, even when applying rapid heating. The reaction at a relatively low temperature (250 °C) with rapid heating gave amorphous agglomerates (Figure 3–7a). In contrast, the product prepared at a higher temperature (400 °C) with rapid heating afforded highly crystallized TiO_2 nanocrystals approximately 5 nm in size (Figure 3–7b). The results of their XRD analysis were also consistent with the TEM observations (Figure 3–7c). The HR-TEM image for the 5-nm TiO_2 nanocrystals also showed a clear lattice fringe with an interplanar distance of 0.19 nm (Figure 3–8), which was correspond to the (200) or (020) planes of anatase TiO_2. These results suggest that rapid heating to a suitable target temperature is crucial to the growth of fine nanocrystals without sintering.

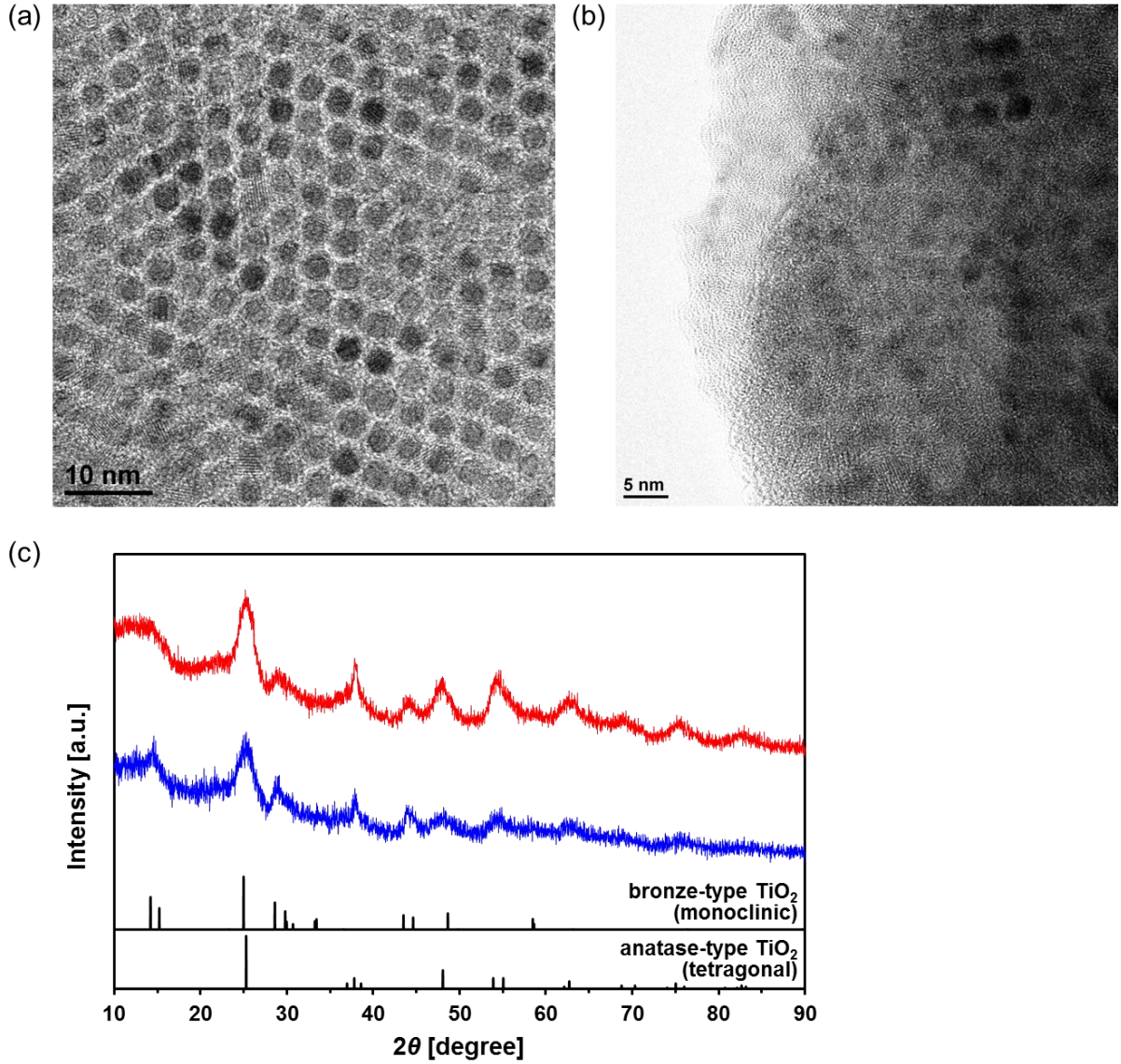

Figure 3–6. TEM images of (a) the TiO_2 nanocrystals synthesized by rapid-heating solvothermal reaction (heating rate: 500 ºC/min, reaction temperature: 300 ºC) and (b) the TiO_2 agglomerates synthesized by slow-heating solvothermal reaction (heating rate: 5.4 ºC/min, reaction temperature: 300 ºC). (c) XRD patterns of the TiO_2 nanocrystals (red line) and the TiO_2 agglomerates (blue line).

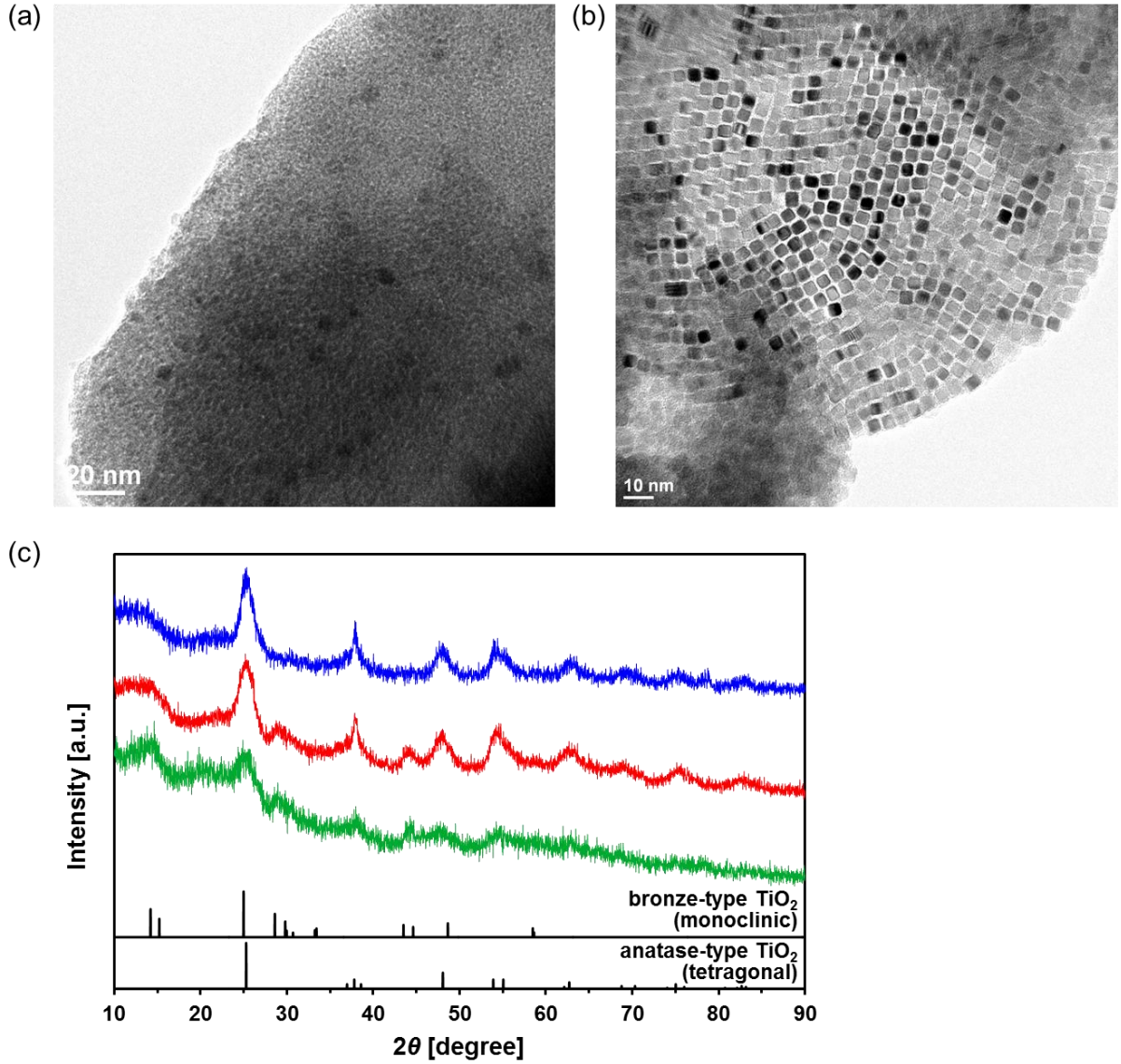

Figure 3–7. TEM images of TiO_2 nanocrystals obtained using different solvothermal-reaction temperature: (a) 250 ˚C, (b) 400 ˚C. (c) XRD pattern of the powdery products with different solvothermal-reaction temperature (blue, 400 ˚C; red, 300 ˚C; green, 250 ˚C)

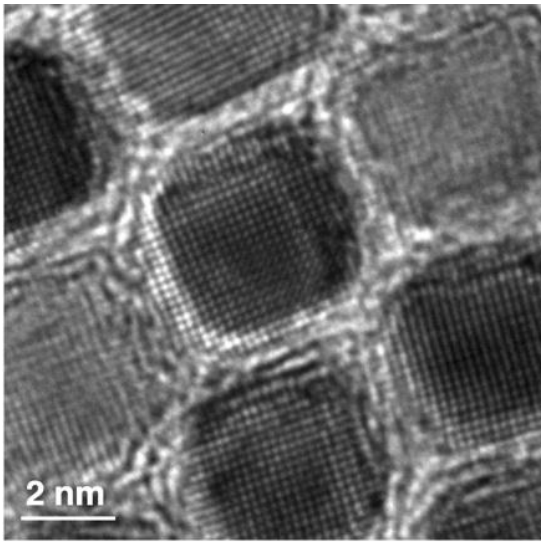

Figure 3–8. HR-TEM image of the obtained TiO_2 nanocrystals (5 nm).

The presence of oleic acid as a solvent and additive is another critical factor in the present reaction. The use of octanoic acid, which has a relatively short aliphatic chain, gave a product having an aggregated structure (Figure 3–9a). In contrast, linoleic acid produced similar nanocrystals with a periodic alignment, indicating that a longer aliphatic chain is necessary to prevent the aggregation of the nanocrystals (Figure 3–9b). Furthermore, judging from the results obtained with oleylamine, the carboxylic acid group is also important to the formation of nanocrystals (Figure 3–9c).

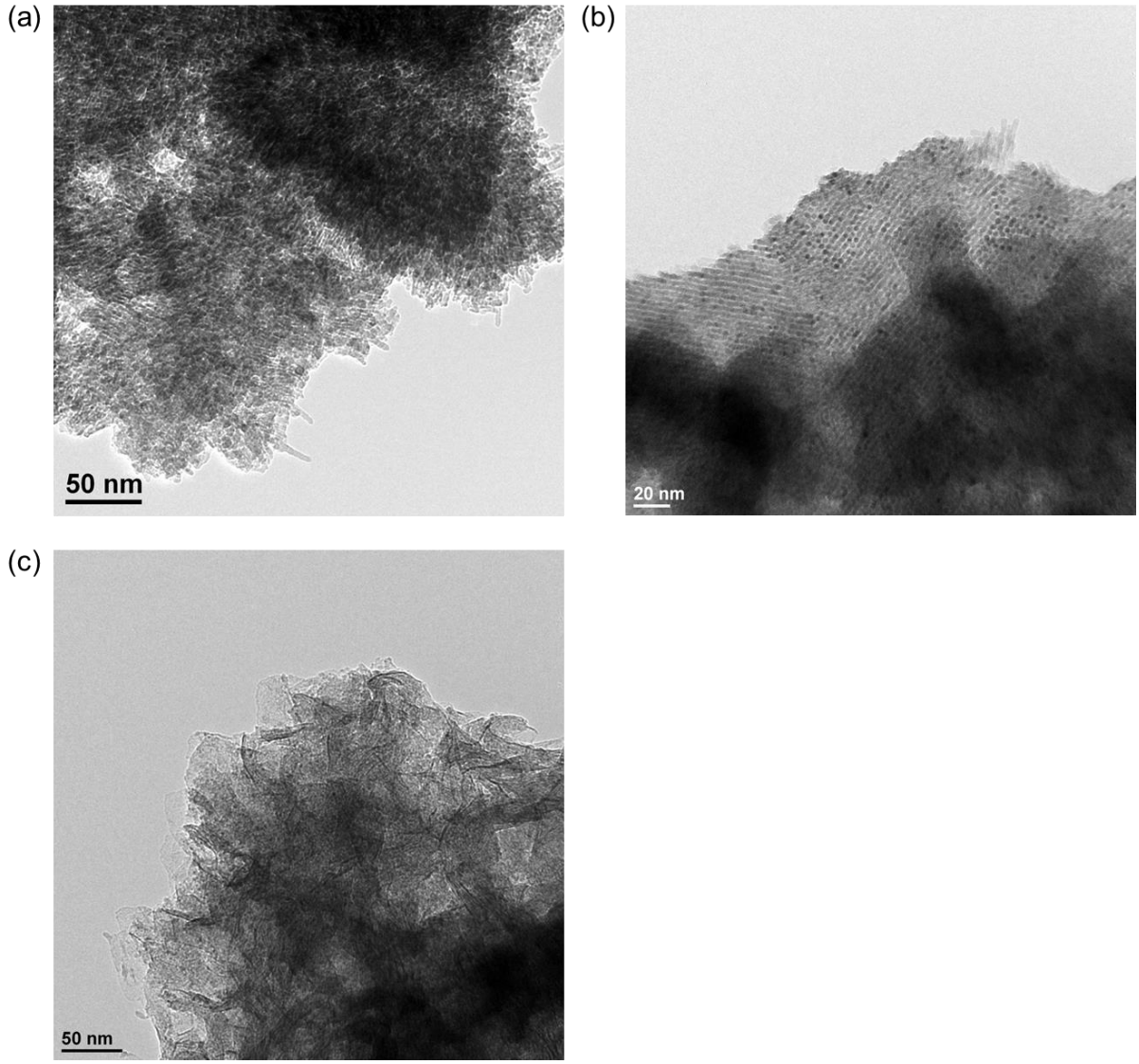

Figure 3–9. TEM images of the TiO_2 particles synthesized by rapid-heating solvothermal reaction (heating rate: 500 ºC/min, reaction temperature: 300 ºC) with (a) octanoic acid, (b) linoleic acid, and (c) oleyl amine instead of oleic acid.

On the basis of the above experimental results, we propose a generation mechanism of hexagonal assemblies. Generally, mesoporous materials having periodic pore, such as MCM-41 and SBA-15, were prepared by using micellar templates composed of ionic surfactants such as cetyltrimethylammonium bromide.[25,26] In contrast to the typical synthetic conditions of mesoporous materials, the neat conditions with a large amount of oleic acid might give rod-like reverse micelles with titanium tetrabutoxide, where butoxy anions were exchanged with oleate anions to wrap the nano-rods.[27] Then, when these soft-templated structures were heated up to 300–400 °C, titanium olate was converted to rod-like nanocrystals. Finally, rod-like nanocrystals were self-assembled in a hexagonal array during drying process. This was confirmed by measuring the SAXS profiles of the rod-like nanocrystals before and after drying (Figure 3–10).[28] The estimated distance (ca. 6.1 nm) between the nanocrystals from the 2 theta angle of the peak in the SAXS profile (2θ = 1.42˚) was consistent with the center-to-center distance of nanocrystals in the TEM observations (Figures 3–1a and 3–2).

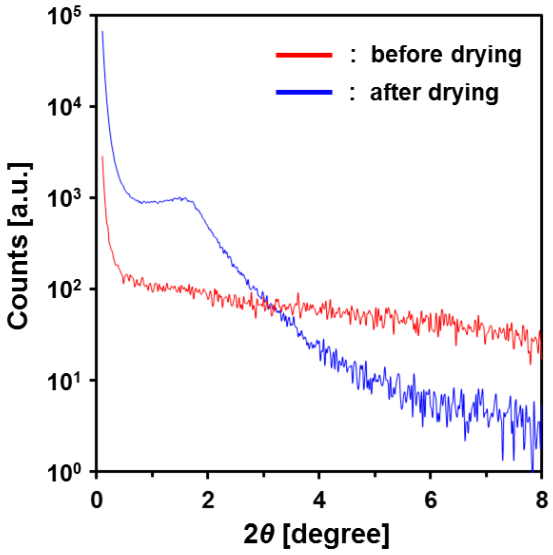

Figure 3–10. SAXS profiles of a methanol dispersion of the TiO_2 nanocrystals before (red line) and after (blue line) drying.

3–3–3. Preparation of the mesoporous TiO_2 thin layer films

Further investigations of the resultant ultrafine TiO_2 nanocrystals revealed another interesting phenomenon. Recently, TiO_2 nanoparticles have been considered for use in practical applications as a coating material to give anti-reflective, self-cleaning properties and superwettability to material surfaces.[29–32] In this context, the structural features of the present TiO_2 nanocrystals motivated us to consider their use as practical coating materials. Figure 3–11a shows the structure of a calcined TiO_2 thin layer film prepared through the drop-casting of a nanocrystal dispersion onto a Si wafer followed by calcination at 400 °C. These SEM observations show that the obtained TiO_2 film had a uniform thickness in the sub-millimeter thickness range (Figures 3–11a-i and 3–12), and a mesoporous structure (Figure 3–11a-ii). The XRD analysis of the resultant calcined film afforded anatase phase with the disappearance of the bronze phase (Figure 3–13). To further characterize the porous thin film, we also performed nitrogen adsorption/desorption measurements to determine the specific surface area and pore size distribution. On the basis of the adsorption-desorption isotherm in Figure 3–11b-i, the specific surface area and mean pore size were estimated to be 136 m^2/g (BET method) and 8.1 nm (Figure 3–11b-ii, BJH method), respectively. This estimated BJH pore size was also consistent with the gap of the nanocrystals in the high magnification image of the SEM observations (Figure 3–11a-ii).

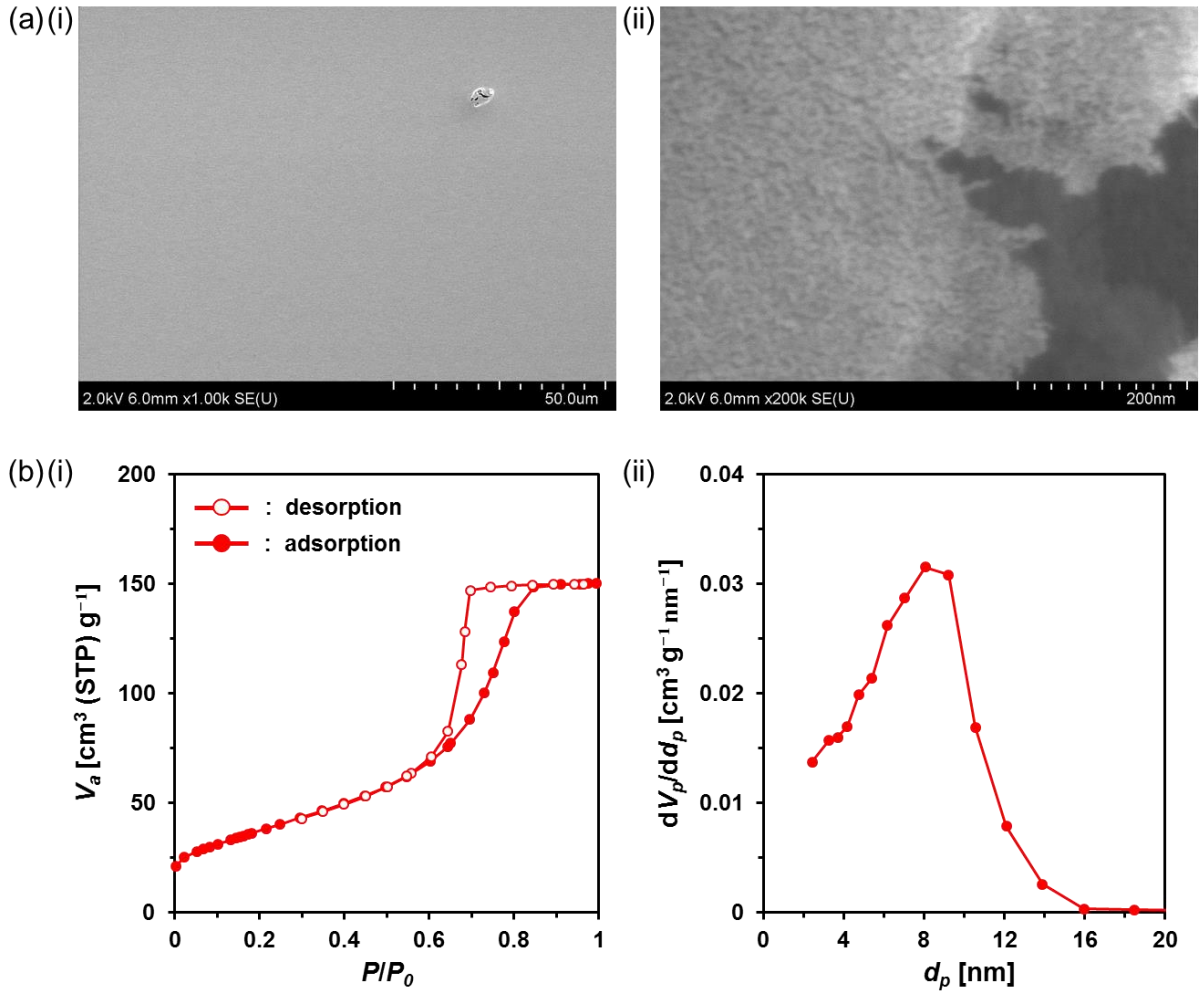

Figure 3–11. (a) SEM images (i, low magnification; ii, high magnification) of the porous TiO_2 thin-layer film obtained by drop-casting a hexane dispersion of TiO_2 nanorods followed by calcination at 400 °C in air. (b) Specific surface area analysis of the calcined TiO_2 film (i, nitrogen adsorption/desorption isotherm; ii, pore size distribution derived by the BJH method.)

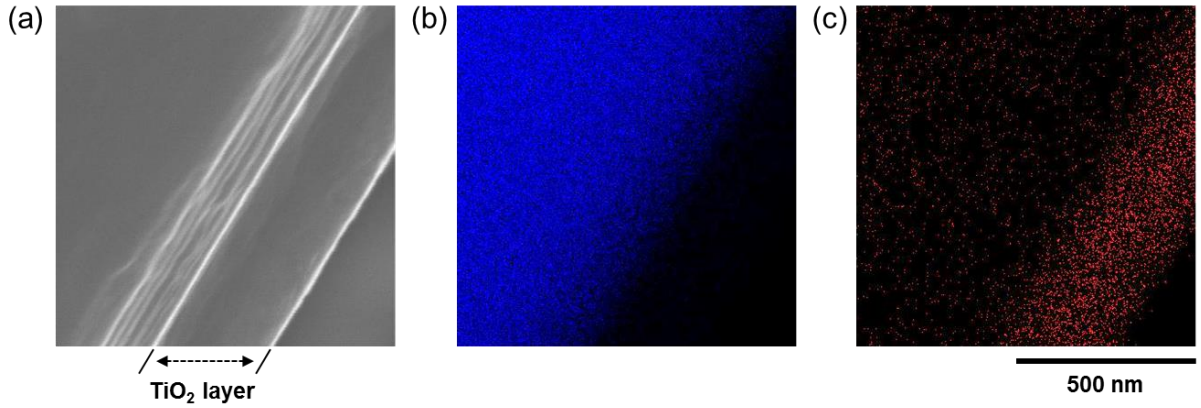

Figure 3–12. The cross-section SEM (a) and EDX mapping (b: Si atom mapping, c: Ti atom mapping) images of the calcined porous TiO_2 film on a silicon wafer, which was prepared from the dispersion of TiO_2 nanocrystals.

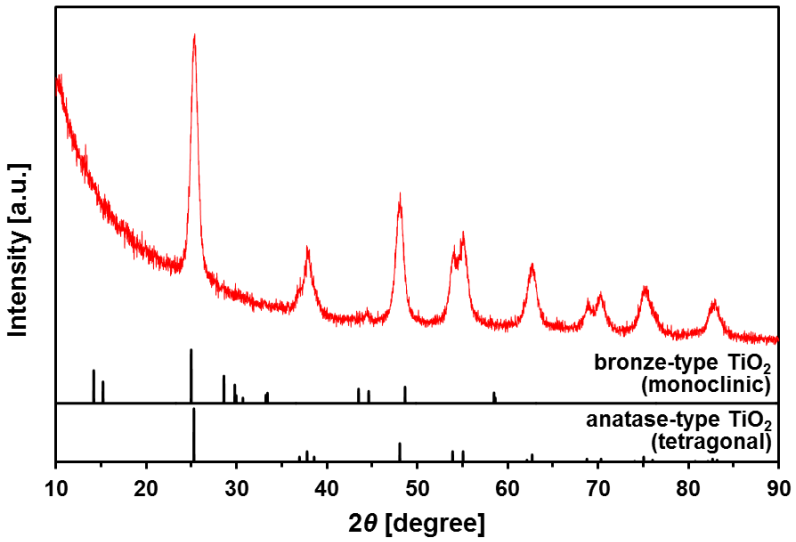

Figure 3–13. XRD pattern of the calcined TiO_2 film prepared from the dispersion of the 3-nm TiO_2 nanocrystals.

The optical properties of the resultant mesoporous TiO_2 film were also assessed. As shown in Figure 3–14a-i, the film had good optical transparency even after three cycles of drop-casting and calcination. Transmittance and reflectance in the UV-visible region were also measured with an integrating sphere system. Consistent with the above optical images, the transmittance and reflectance spectra exhibited no significant changes with repeated TiO_2 coating applications, although the slight decreasing of the transmittance and increasing of the reflectance in the ultraviolet region from 300 to 400 nm was observed corresponding to the band-gap absorption of the TiO_2 nanocrystals. To emphasize this point, we also conducted a similar experiment with commercial TiO_2 nanoparticles approximately 25 nm in size, as a control. For comparison, the same amount of commercial TiO_2 (Degussa P25) was deposited on glass in the same manner. In this case, the optical transparency and reflectivity were significantly changed over three cycles of coating (Figure 3–14b), possibly due to the surface roughness of the resultant film, as indicating by the SEM images in Figure 3–15. These results indicate the potential of our ultrafine nanocrystals as coating materials.

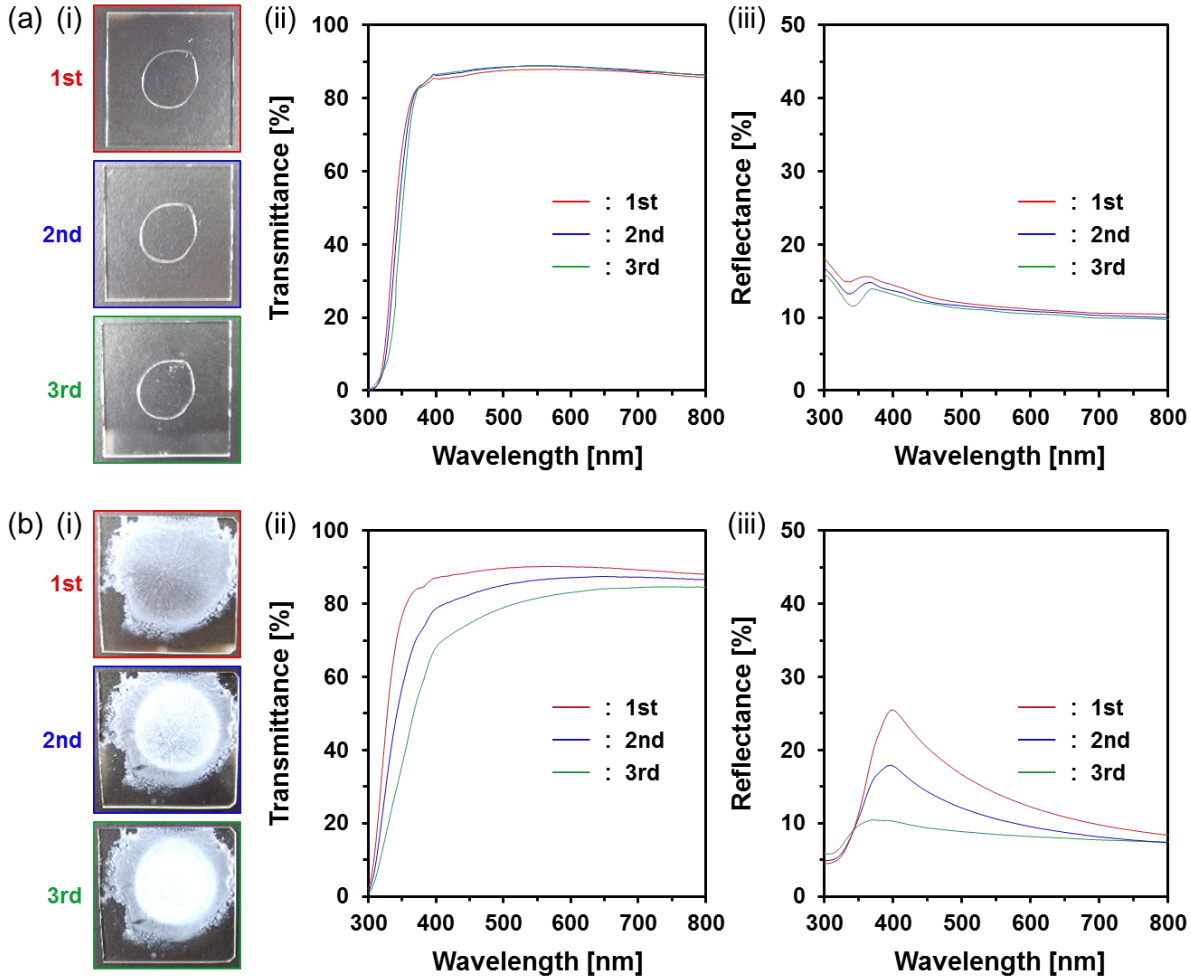

Figure 3–14. Optical image (i), transmittance spectra (ii), and reflectance spectra (iii) of deposited TiO_2 thin films on glass substrates prepared from dispersions of (a) TiO_2 nanocrystals and (b) commercial TiO_2 (Degussa P25 TiO_2) nanoparticles.

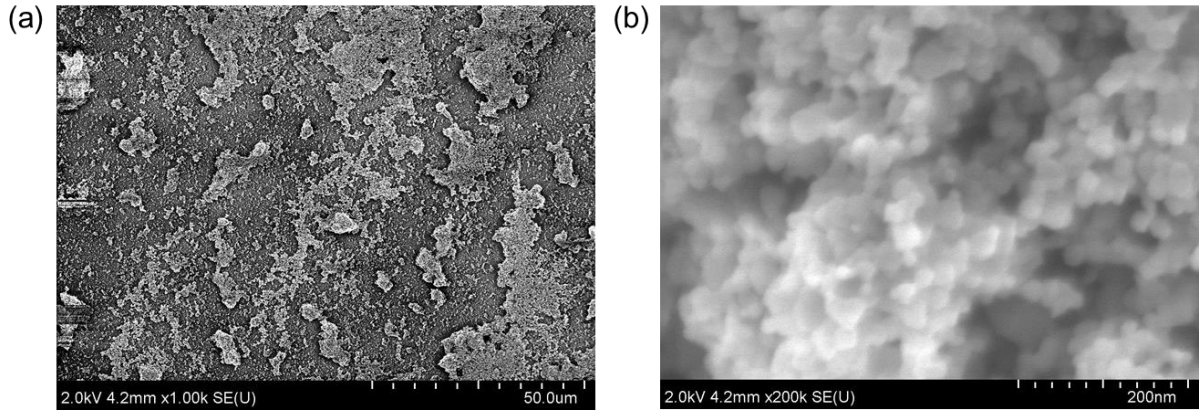

Figure 3–15. SEM images of the calcined TiO_2 film prepared from the dispersion of commercial TiO_2 (Degussa P25 TiO_2) nanoparticles: at (a) low magnification and (b) high magnification.

3–3–4. Evaluation of catalytic ability of TiO_2 thin layer film

To evaluate the catalytic ability of the above mesoporous TiO_2 thin layer film, transient photocurrent measurements were also performed. Prior to these measurements, TiO_2 samples (our 3-nm TiO_2 nanocrystals and P25 TiO_2) were drop-cast on ITO glass and calcined in the same manner as above. The resultant TiO_2 films were used as photoanodes in photoelectrochemical cells with a standard three-electrode setup. As shown in Figure 3–16, both TiO_2 film electrodes showed stable photocurrent responses during repeated ON-OFF photoirradiation cycles. However, in spite of its transparency, the mesoporous TiO_2 film electrode prepared from the ultrafine TiO_2 nanocrystals generated a photocurrent 2.7 times that obtained from the commercial P25-TiO_2 film electrode. The stability of photocatalysts was proved by 15 cycles of repeated ON-OFF photoirradiation in Figure 3–17. In addition, the comparison of the photocatalytic activity between nanocrystal films prepared from the dispersions of the 3-nm and 5-nm TiO_2 nanocrystals (Figure 3–18), which were synthesized different solvothermal reaction temperature, showed similar results (Figure 3–19), although the slight photocurrent improvement in the case of the 3-nm TiO_2 nanocrystal film was observed due to the nano confinement effect. The above series of experiments clearly demonstrate the potential usefulness of these ultrafine TiO_2 nanocrystals in a wide variety of applications, such as coating materials for anti-reflection and self-cleaning films and electrode base materials for solar cells.

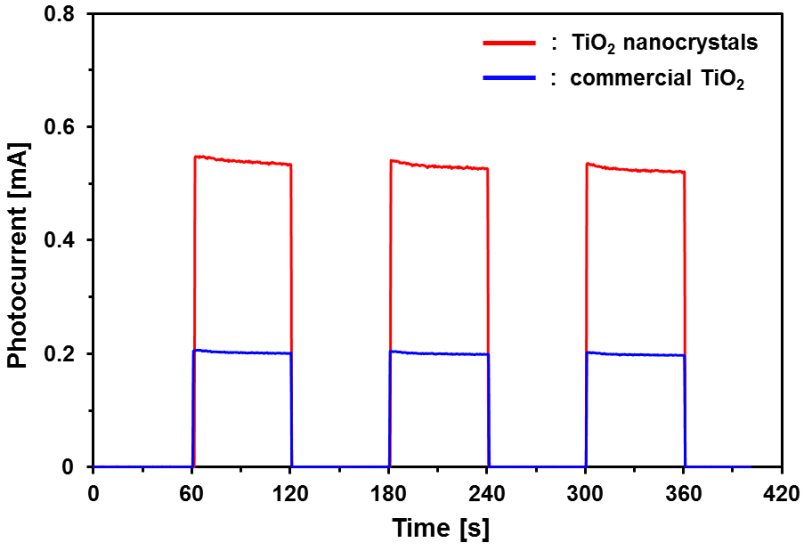

Figure 3–16. Transient photocurrent responses of semiconducting thin layer electrodes prepared from ultrafine 3-nm TiO_2 nanocrystals (red line) and commercial TiO_2 nanoparticles (Degussa P25 TiO_2, blue line) under ON-OFF cycles of UV irradiation (< 350 nm).

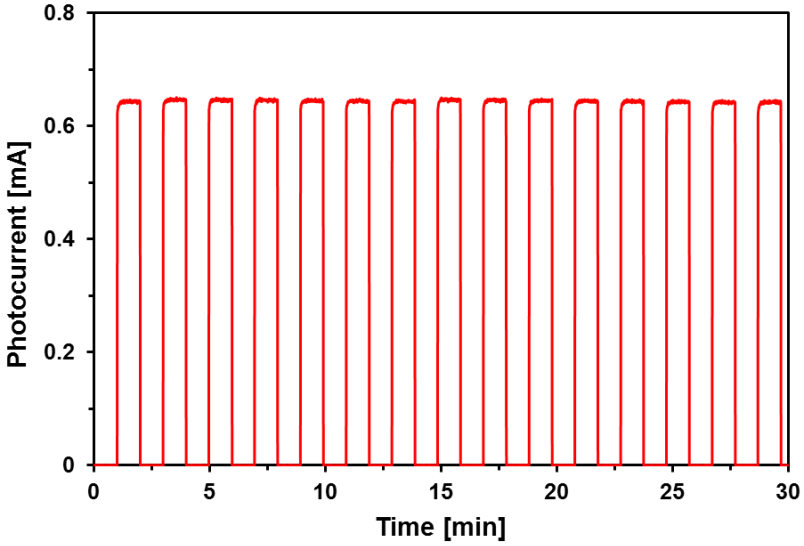

Figure 3–17. Transient photocurrent responses of semiconducting thin layer electrodes prepared from ultrafine 3-nm TiO_2 nanocrystals under ON-OFF cycles of UV irradiation (< 350 nm).

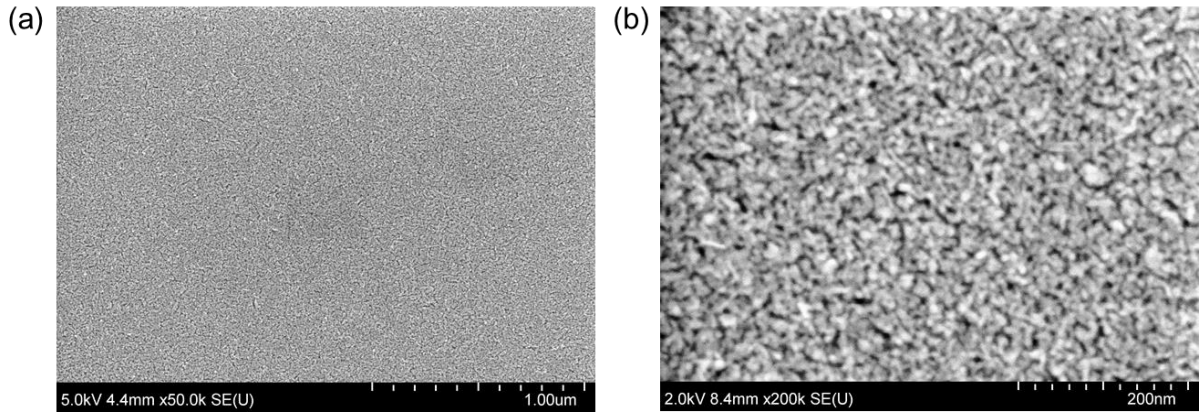

Figure 3–18. SEM images of the calcined TiO_2 film prepared from the dispersion of 5-nm TiO_2 nanocrystals: at (a) low magnification and (b) high magnification.

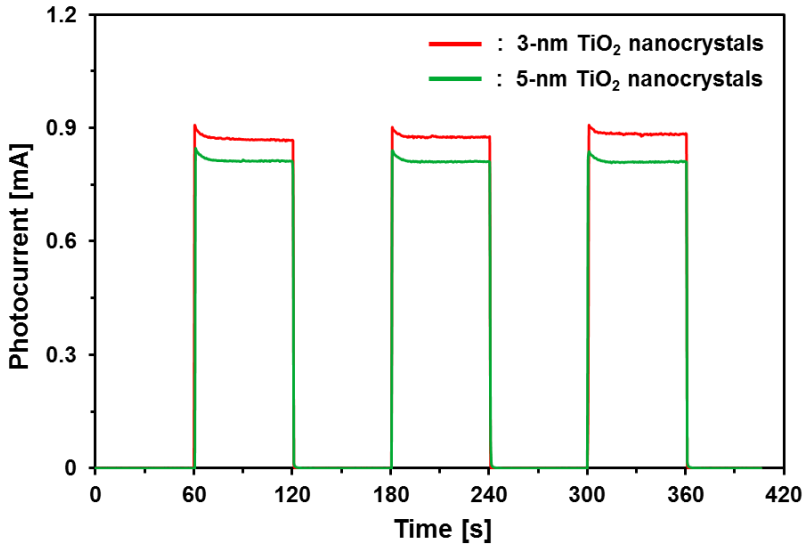

Figure 3–19. Transient photocurrent responses of semiconducting thin layer electrodes prepared from ultrafine 3-nm TiO_2 nanocrystals (synthesized by the solvothermal reaction at 300 ºC, red line) and 5-nm TiO_2 nanocrystals (synthesized by the solvothermal reaction at 400 ºC, green line) under ON-OFF cycles of UV irradiation (< 350 nm).

3–4. Conclusions

In conclusion, a new method for synthesizing ultrafine TiO_2 nanocrystals using a rapid one-pot solvothermal reaction were demonstrated. It is of particular note that these monodispersed ultrafine nanocrystals can be easily converted into a low reflecting porous thin layer through a simple drop-casting and calcination process. The present research suggests a new approach to the facile synthesis of ultrafine nanocrystals and the preparation of nano concave-convex surfaces for transparent anti-reflection materials.

Reference

1. Polavarapu, L.; Mourdikoudis, S.; Pastoriza-Santos, I.; Pérez-Juste, J. Nanocrystal engineering of noble metals and metal chalcogenides: controlling the morphology, composition and crystallinity. *CrystEngComm* **2015**, *17*, 3727–3762.
2. Huang, W. Oxide nanocrystal model catalysts. *Acc. Chem. Res.* **2016**, *49*, 520–527.
3. Jun, Y.-W.; Choi, J.-S.; Cheon, J. Shape control of semiconductor and metal oxide nanocrystals through nonhydrolytic colloidal routes. *Angew. Chem., Int. Ed.* **2006**, *45*, 3414–3439.
4. Kuang, Q.; Wang, X.; Jiang, Z.; Xie, Z.; Zheng, L. High-energy-surface engineered metal oxide micro- and nanocrystallites and their applications. *Acc. Chem. Res.* **2014**, *47*, 308–318.
5. Wang, H.; Guan, C.; Wang, X.; Fan, H. J. A high energy and power Li-ion capacitor based on a TiO_2 nanobelt array anode and a graphene hydrogel cathode. *Small* **2015**, *11*, 1470–1477.
6. Wang, F.; Wang, C.; Zhao, Y.; Liu, Z.; Chang, Z.; Fu, L.; Zhu, Y.; Wu, Y.; Zhao, D. A quasi-solid-state Li-ion capacitor based on porous TiO_2 hollow microspheres wrapped with graphene nanosheets. *Small* **2016**, *12*, 6207–6213.
7. Padilha, A. C. M.; Raebiger, H.; Rocha, A. R.; Dalpian, G. M. Charge storage in oxygen deficient phases of TiO_2: defect physics without defects. *Sci. Rep.* **2016**, *6*, 28871.
8. Wang, X.; Li, Z.; Shi, J.; Yu, Y. One-dimensional titanium dioxide nanomaterials: nanowires, nanorods, and nanobelts. *Chem. Rev.* **2014**, *114*, 9346–9384.
9. Liu, G.; Yang, H. G.; Pan, J.; Yang, Y. Q.; Lu, G. Q.; Cheng, H.-M. Titanium dioxide crystals with tailored facets. *Chem. Rev.* **2014**, *114*, 9559–9612.
10. Chen, X.; Mao, S. S. Titanium dioxide nanomaterials: synthesis, properties, modifications,

and applications. *Chem. Rev.* **2007**, *107*, 2891–2959.

11. Cargnello, M.; Gordon, T. R.; Murray, C. B. Solution-phase synthesis of titanium dioxide nanoparticles and nanocrystals. *Chem. Rev.* **2014**, *114*, 9319–9345.
12. Sang, L.; Zhao, Y.; Burda, C. TiO_2 nanoparticles as functional building blocks. *Chem. Rev.* **2014**, *114*, 9283–9318.
13. Ichijo, T.; Sato, S.; Fujita, M. Size-, mass-, and density-controlled preparation of TiO_2 nanoparticles in a spherical coordination template. *J. Am. Chem. Soc.* **2013**, *135*, 6786–6789.
14. Satoh, N.; Nakashima, T.; Kamikura, K.; Yamamoto, K. Quantum size effect in TiO_2 nanoparticles prepared by finely controlled metal assembly on dendrimer templates. *Nat. Nanotechnol.* **2008**, *3*, 106–111.
15. Wang, P.; Kobiro, K. Ultimately simple one-pot synthesis of spherical mesoporous TiO_2 nanoparticles in supercritical methanol. *Chem. Lett.* **2012**, *41*, 264–266.
16. Wang, P.; Yokoyama, K.; Konishi, T.; Nishiwaki, N.; Kobiro, K. Ultimately simple one-pot single-step synthesis of rare earth doped spherical mesoporous metal oxide nanospheres with upconversion emission ability in supercritical methanol. *J. Supercrit. Fluids* **2013**, *80*, 71–77.
17. Wang, P.; Ueno, K.; Takigawa, H.; Kobiro, K. Versatility of one-pot, single-step synthetic approach for spherical porous (metal) oxide nanoparticles using supercritical alcohols. *J. Supercrit. Fluids* **2013**, *78*, 124–131.
18. Pradeep, E. K. C.; Habu, T.; Tooriyama, H.; Ohtani, M.; Kobiro, K. Ultra-simple synthetic approach to the fabrication of CeO_2–ZrO_2 mixed nanoparticles into homogeneous, domain, and core–shell structures in mesoporous spherical morphologies using supercritical alcohols. *J. Supercrit. Fluids* **2015**, *97*, 217–223.
19. Pradeep, E. K. C.; Ohtani, M.; Kobiro, K. A simple synthetic approach to Al_2O_3–TiO_2 and

$ZnO–TiO_2$ mesoporous hollow composite assemblies consisting of homogeneously mixed primary particles at the nano level. *Eur. J. Inorg. Chem.* **2015**, 5621–5627.

20. Duriyasart, F.; Hamauzu, H.; Ohtani, M.; Kobiro, K. Three-dimensionally branched titanium dioxide with cheek-brush morphology: synthesis and its application to polymer composites. *ChemistrySelect* **2016**, *1*, 5121–5128.
21. Nguyen, H. T. T.; Habu, T.; Ohtani, M.; Kobiro, K. One-step direct synthesis of $SiO_2–TiO_2$ composite nanoparticle assemblies with hollow spherical morphology. *Eur. J. Inorg. Chem.* **2017**, 3017–3023.
22. Ohtani, M.; Muraoka, T.; Okimoto, Y.; Kobiro, K. Rapid one-pot solvothermal batch synthesis of porous nanocrystal assemblies composed of multiple transition-metal elements. *Inorg. Chem.* **2017**, *57*, 11546–11551.
23. Kobayashi, M.; Petrykin, V. V.; Kakihana, M. One-step synthesis of TiO_2(B) nanoparticles from a water-soluble titanium complex. *Chem. Mater.* **2007**, *19*, 5373–5376.
24. Chen, Y.; Kang, K. S.; Yoo, K. H.; Jyoti, N.; Kim, J. Cause of slow phase transformation of TiO_2 nanorods. *J. Phys. Chem. C* **2009**, *113*, 19753–19755.
25. Wan, Y.; Zhao, D. On the controllable soft-templating approach to mesoporous silicates. *Chem. Rev.* **2007**, *107*, 2821–2860.
26. Hossain, M. K.; Koirala, A. R.; Akhtar, U. S.; Song, M. K.; Yoon, K. B. First synthesis of highly crystalline, hexagonally ordered, uniformly mesoporous TiO_2–B and its optical and photocatalytic properties. *Chem. Mater.* **2015**, *27*, 6550–6557.
27. Huo, Z.; Tsung, C.-K.; Huang, W.; Fardy, M.; Yan, R.; Zhang, X.; Li, Y.; Yang, P. Selforganized ultrathin oxide nanocrystals. *Nano Lett.* **2009**, *9*, 1260–1264.
28. Cormary, B.; Li, T.; Liakakos, N.; Peres, L.; Fazzini, P.; Blon, T.; Respaud, M.; Kropf, A. J.; Chaudret, B.; Miller, J. T.; Mader, E. A.; Soulantica, K. Concerted growth and ordering of cobalt nanorods arrays as revealed by tandem in situ SAXS-XAS studies. *J. Am. Chem.*

Soc. **2016**, *138*, 8422–8431.

29. Zhang, X.-T.; Sato, O.; Taguchi, M.; Einaga, Y.; Murakami, T.; Fujishima, A. Self-cleaning particle coating with antireflection properties. *Chem. Mater.* **2005**, *17*, 696–700.
30. Nakata, K.; Sakai, M.; Ochiai, T.; Murakami, T.; Takagi, K.; Fujishima, A. Antireflection and self-cleaning properties of a moth-eye-like surface coated with TiO_2 particles. *Langmuir* **2011**, *27*, 3275–3278.
31. Xi, J.-Q.; Schubert, M. F.; Kim, J. K.; Schubert, E. F.; Chen, M.; Lin, S.-Y.; Liu, W.; Smart, J. A. Optical thin-film materials with low refractive index for broadband elimination of Fresnel reflection. *Nat. Photon*. **2007**, 1, 176–179.
32. Liu, K.; Cao, M.; Fujishima, A.; Jiang, L. Bio-inspired titanium dioxide materials with special wettability and their applications. *Chem. Rev.* **2014**, *114*, 10044–10094.

Chapter IV.

Selective synthesis of Ti-based nanocrystals *via* hydrothermal method using squaric acid

4–1. Introduction

TiO_2 is known as a promising material used in a wide area of applications in energy storage, photocatalysts, solar cells, and other optoelectronic devices.[1,2] Controlling crystal structures and exposing desired crystal face are important for improving performance.[3,4] Three types of TiO_2 crystal structures were known: rutile (tetragonal), anatase (tetragonal), and brookite (orthorhombic). Stability of the TiO_2 phases depends on their particle sizes. Rutile is the most stable phase for particles where particle sizes are above 35 nm, anatase is the most stable phase for nanoparticles of which particle sizes are below 11 nm, and brookite is found to be the most stable for 11–35nm nanoparticles.[5] Although anatase-type TiO_2 with large surface area has been well studied, few studies have been reported on the synthesis of rutile-type TiO_2 with a specific surface area over 100 m^2/g.[6–8]

The fundamental structure of all three crystal phases of TiO_2 consists of TiO_6 octahedra with different spatial arrangements (Figure 4–1).[9] Rutile is composed of primarily corner-sharing octahedra with each octahedron surrounded by ten octahedra: two of them are edge-shared, and eight of them are corner shared. The TiO_6 octahedra in anatase are surrounded by eight octahedra (four edges and four corners are shared). Thus, the fraction of edge-sharing octahedra to form anatase is larger than that of rutile (50% *vs* 20%, respectively). In order to form an edge-sharing bond between two octahedra, two juxtaposed hydrolysis and condensation reactions must occur. Corner-sharing octahedra requires just one hydrolysis and

condensation reaction in the coordination sphere. Therefore, the crystal phases of TiO_2 can be formed separately by controlling the hydrolysis and condensation reactions depending to the coordination form of the titanium complex.[9–11]

In this chapter, hydrothermal synthesis of urchin-like TiO_2 crystals with rutile crystal phase using squaric acid was studied. Squaric acid (3,4-dihydroxycyclobut-3-ene-1,2-dione) is a type of oxocarbonic acid in which two carbonyl groups and two hydroxyl groups are arranged on a cyclobutene ring *via* a conjugated system. Squaric acid features quite strong acidity[12] (pK_{a1} = 0.54, Figure 4–2) as an organic acid as well as unique square molecular structure with various coordination modes to metal cations (Figure 4–3).[13] Due to its unique properties, it is widely used in the fields such as synthetic organic chemistry, medicinal chemistry, and functional materials science.[14–16] In particular, squaric acid has attracted significant attention as a ligand for metal–organic frameworks (MOFs).[17–21] However, to our knowledge, such unique squaric acid has not been utilized as an additive for metal oxide nanoparticles. Then, I expect that the usage of squaric acid would be a new synthetic approach to lead a new type of metal oxide particle assemblies.

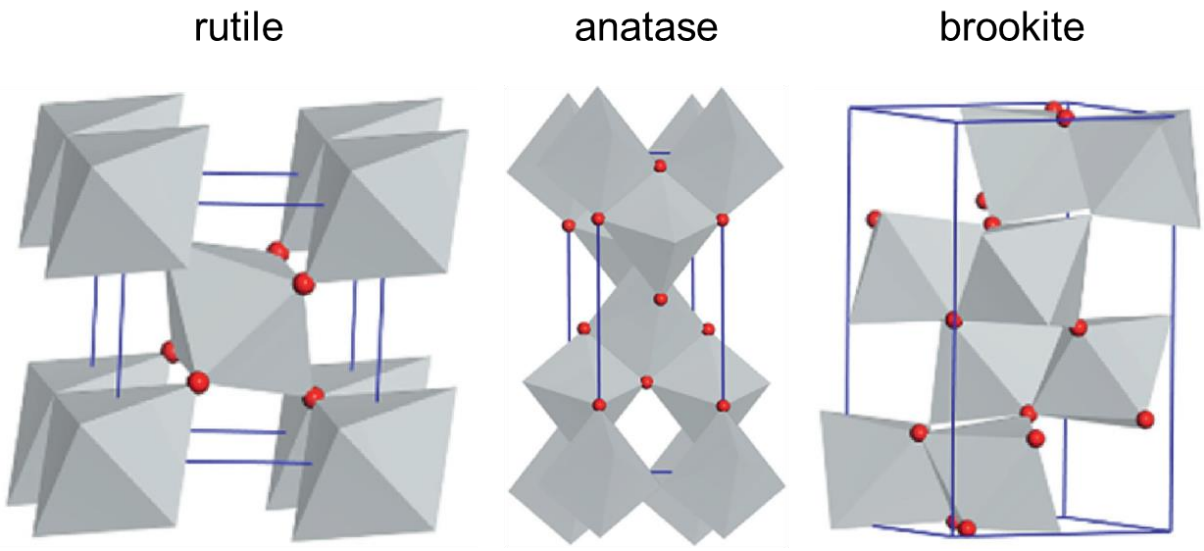

Figure 4–1. Illustrations of the TiO_6 octahedral arrangements.

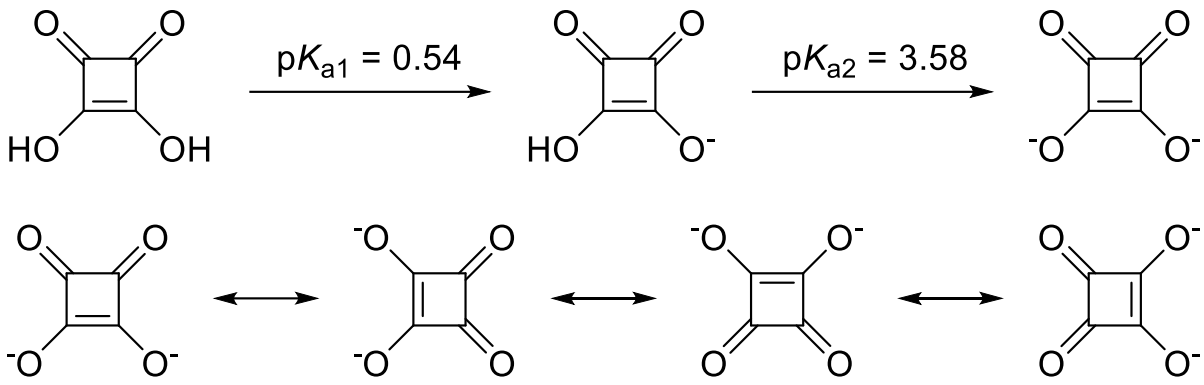

Figure 4–2. Acidity and delocalization of squaric acid.

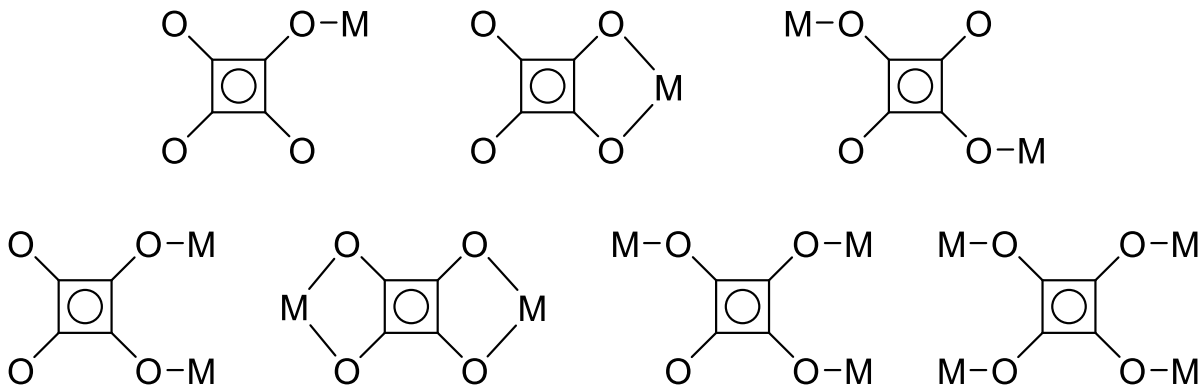

Figure 4–3. Different bridging modes of squarate dianion with metal cations.

4–2. Experiment

4–2–1. Materials

Titanium tetraisopropoxide [Ti(O^iPr)$_4$], tris(acetylacetonato)ruthenium(III) [Ru(acac)$_3$], methanol, potassium bromide (KBr), molecular sieves 3A, and silica gel were obtained from FUJIFIM Wako Pure Chemical Corporation. Squaric acid was purchased from Tokyo Chemical Industry Co., Ltd. Commercial TiO_2 nanoparticles (JRC-TIO-16) was obtained from Sakai Chemical Industry Co., Ltd. All reagents were used as received unless otherwise noted.

4–2–2. Synthetic procedure

Synthesis of Ti-based nanocrystals. Ti(O^iPr)$_4$ (196 μL, 0.625 mmol) was added to a solution of squaric acid in water (12.5 mL) and the suspension was sonicated at 50 °C. The resultant precursor solution was sealed in a Teflon-lined autoclave with a 25 mL inner volume. The sealed autoclave was heated to 150 °C and the temperature was maintained at 150 °C for 3 h. After cooling to room temperature, the precipitates were centrifuged, washed with water and methanol several times, and dried in a vacuum to afford a powdery product.

Synthesis of hexagonal plates. Ti(O^iPr)$_4$ (196 μL, 0.625 mmol) was added to a solution of squaric acid (285 mg, 2.5 mmol) in water (12.5 mL) and the suspension was sonicated at 50 °C. The resultant precursor solution was sealed in a Teflon-lined autoclave with a 25 mL inner volume. The sealed autoclave was heated to 120 °C and the temperature was maintained at 120 °C for 72 h. After cooling to room temperature, the precipitates were centrifuged, washed with water and methanol several times, and dried in a vacuum to afford a powdery product. hexagonal plates

Synthesis of urchin-like TiO_2 nanocrystals. Ti(O^iPr)$_4$ (2.35 mL, 7.5 mmol) was added to a solution of squaric acid (570 mg, 5 mmol) in water (50 mL) and the suspension was

sonicated at 50 °C for 3 h. The resultant precursor solution was sealed in a Teflon-lined autoclave with a 100 mL inner volume. The sealed autoclave was heated to 180 °C and the temperature was maintained at 180 °C for 5 h. After cooling to room temperature, the precipitates were centrifuged, washed with water and methanol several times, and dried in a vacuum to afford a powdery product.

Preparation of RuO_2/TiO_2. RuO_2/TiO_2 catalysts with Ru amount of 2 wt% were prepared by wet impregnation method. Prior to wet impregnation, urchin-like TiO_2 nanocrystals were calcined at 350 °C for 1 h in air to remove organic residue. $Ru(acac)_3$ (40 mg, 0.1 mmol) dissolved in 5 mL of methanol was added to a powdery support (500 mg) prior to the sonication for 5 min. Then mixed solution was stirred using an AR-100 planetary centrifugal mixer (Thinky Corp.) until the solvent was evaporated. The obtained product was grounded with a pestle and a mortar and dried at 80 °C for 1 h in an oven. The obtained powdery product was calcined at 300 °C for 2 h in air to yield the final product.

4–2–3. Characterization methods

Transmission electron microscopy. The transmission electron microscopy (TEM) images were obtained using a JEOL JEM-2100F. The specimens were prepared as follows: samples were dispersed in methanol; 10 μL of the resultant dispersion was drop-casted onto a carbon-coated copper microgrid (Okenshoji, Japan); and the solvent was evaporated under atmospheric pressure. Energy dispersive X-ray (EDX) mappings of high angle annular dark-field scanning transmission electron microscopy (HAADF-STEM) images were obtained using an Oxford INCA X-max 80 EDX spectrometer.

Scanning electron microscopy. Scanning electron microscopy (SEM) was performed using a Hitachi SU8020 FE-SEM. The specimens were prepared by drop-casting the sample

dispersion on a silicon wafer.

X-ray diffraction measurements. X-ray diffraction (XRD) patterns were recorded using a Rigaku SmartLab diffractometer with graphite-monochromatized Cu Kα radiation (X-ray wavelength: 1.5418 Å) in steps of 0.02° over the 2θ range of 5−90°. The powdery samples were placed on a non-refractive silicon holder (Overseas X-Ray Service, Japan).

Energy dispersive X-ray fluorescence analysis. Energy dispersive X-ray fluorescence (EDXRF) analysis was performed using a Epsilon 1 (Malvern Panalytical Ltd.). The powdery samples (100 mg) were loaded in the plastic cup (inner diameter: 6 mm) to cover with Mylar film (6 μm).

Thermogravimetric analysis. The thermogravimetric (TG) analysis was performed using a HITACHI STA7200RV instrument. A sample was placed on an open platinum sample pan. The samples were heated at a 2 °C/min heating rate in air.

Infrared spectroscopic measurements. Fourier transform infrared (FT-IR) spectra were recorded using a JASCO FT/IR-4600 spectrometer. The sample was mixed with KBr and measured using diffuse reflection method.

Nitrogen adsorption-desorption isotherm measurements. Nitrogen adsorption-desorption isotherms were obtained using a Belsorp Mini II instrument (BEL Corp.). Before performing measurement, the powdery samples were pre-treated by vacuum heating at 250 °C for 5 h to remove absorbed moisture on surface. The specific surface areas were determined using the Brunauer–Emmett–Teller (BET) multipoint method.

CO-pulse adsorption measurements. Prior to pulse measurement, RuO_2/TiO_2 catalyst (50 mg) was reduced under H_2 stream (30 mL/min) at 200 °C for 2 h, and Ru/TiO_2 catalyst was pretreated at 200 °C for 1 h in He to remove adsorbed H_2. Then, CO-pulse adsorption

measurement was performed using 5 vol% CO/He (50 mL/min) at 50 °C. The outlet gas was analyzed by BELCAT II (MicrotracBEL) equipped with a thermal conductivity detector (TCD) using He as a carrier gas. The Ru dispersion was calculated as follows:

$$\text{Ru dispersion} = \frac{V_{\text{CO}} \times SF/22414 \times M}{Wx} \times 100$$

where V_{CO}: absorbed amount

SF: stoichiometric factor (1)

M: atomic mass of Ru (101.07 g/mol)

W: weight of sample (g)

x: loading amount of Ru deposits on the TiO_2 supports (quantified by XRF analysis)

Evaluation of catalytic activity. The catalytic activity of the Ru/TiO_2 catalysts for CO_2 methanation was tested using the flow-type reactor (BELCAT II; MicrotracBEL) at the atmospheric pressure. The catalyst (200 mg) was loaded in the fixed bed reactor stuffed by quartz wool on both sides. Prior to the active test, the catalyst was reduced under H_2 stream (30 mL/min) at 200 °C for 2 h. Then, CO_2 methanation was conducted in a mixed gas stream of CO_2 (10%), H_2 (40%), and Ar (50%) at a total flow rate of 20 mL/min. After the mixed gas was fed for 30 min, the effluent gaseous products were passed through a molecular sieves 3A and silica gel to remove water vapor and then analyzed by a gas chromatograph (GC3200; GL Sciences) using an active carbon column equipped with a TCD using Ar as a carrier gas. From the GC data, the CH_4 yield (%) was determined as follows:

$$\text{CH}_4 \text{ yield (\%)} = \frac{X_{\text{CH}_4}}{X_{\text{CO}_2} + X_{\text{CH}_4} + X_{\text{CO}}} \times 100$$

where X_{CO_2}: proportion of CO_2 molecules in the outflow

X_{CH_4}: proportion of CH_4 molecules in the outflow

X_{CO}: proportion of CO molecules in the outflow

To calculate chemical equilibrium of the product mixture, Newton's method is employed with the NASA computer program Chemical Equilibrium with Applications (CEA) developed by Gordon and McBride.[22] The activation energies of the catalysts was assessed *via* turnover frequency (TOF), which was normalized by the loading amount and the dispersion of Ru deposits on TiO_2 supports[23]:

$$\text{TOF } (S^{-1}) = \frac{F_{CO_2} X_{CH_4} M}{WDx}$$

where F_{CO_2}: moles of CO_2 per unit time in the inflow (mol/s)

X_{CH_4}: proportion of CH_4 molecules in the outflow

M: atomic mass of Ru (101.07 g/mol)

W: weight of catalyst (g)

D: Ru dispersion of Ru on the support

x: loading amount of Ru deposits on the TiO_2 supports (quantified by EDXRF analysis)

4–3. Results and discussion

4–3–1. Hydrothermal synthesis of Ti-based nanocrystals using squaric acid

$Ti(O^iPr)_4$ was mixed with water yielding a white suspension. Squaric acid was added to the suspension and the suspension was sonicated. Then, the white suspension changed to a homogeneous red solution (Figure 4–4). The slow resolution with drastic color change suggests that a rather strong Ti(IV)-oxocarbon interaction *via* the CO moieties with the formation of a strongly allowed ligand to metal charge transfer state.[24]

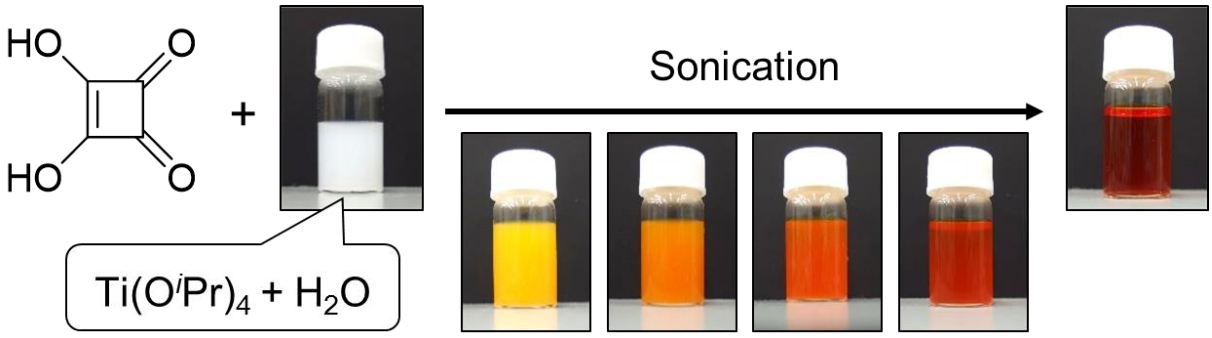

Figure 4–4. Change in color of precursor solutions.

The precursor aqueous solutions were heated at 150 °C for 3 h in a Teflon autoclave. TiO_2 synthesized without additives had a heterogeneous morphology and crystal phases of anatase and brookite (entry 1 in Table 4–1, Figures 4–5a and c). On the other hand, TiO_2 obtained by adding squaric acid had an urchin-like morphology and a crystal phases of rutile (entry 2 in Table 4–1, Figures 4–5b and c).

Table 4–1. Reaction conditions of the prepared Ti-based nanocrystals using squaric acid.

Entry	Concentration of $Ti(O^iPr)_4$ [mmol/L]	Concentration of squaric acid [mmol/L]	Molar ration of $Ti(O^iPr)_4$ and squaric acid	Volume of H_2O [mL]	Reaction temperature [°C]	Reaction time [h]
1	50	–	1 : 1	17.5	150	3
2	50	50	1 : 1	17.5	150	3
3	75	75	1 : 1	17.5	150	3
4	100	100	1 : 1	17.5	150	3
5	150	150	1 : 1	17.5	150	3
6	50	50	1 : 1	12.5	150	3
7	50	100	1 : 2	12.5	150	3
8	50	200	1 : 4	12.5	150	3
9	50	200	1 : 4	12.5	120	72
10	50	50	1 : 1	17.5	150	0.5
11	150	100	3 : 2	50	180	5

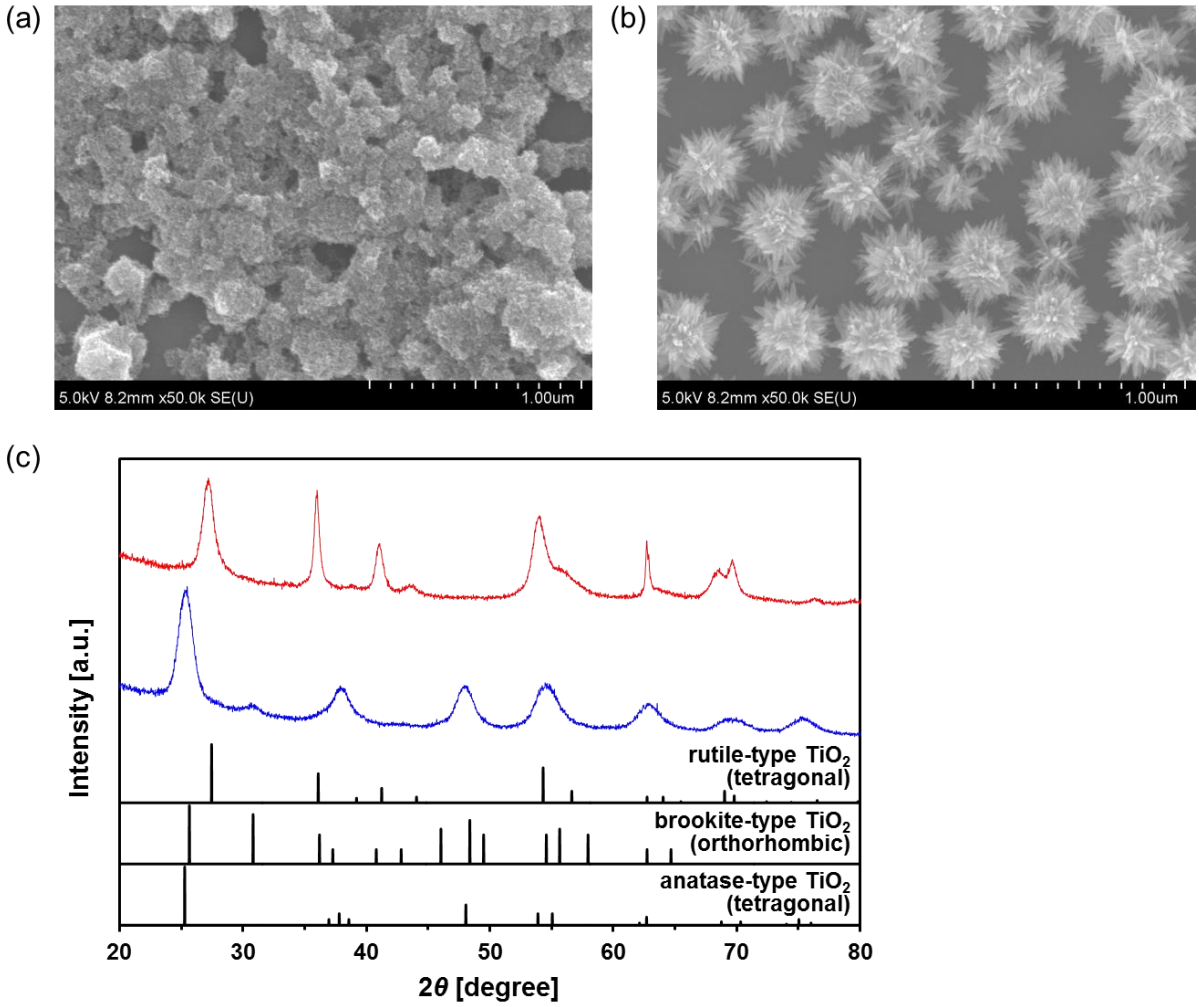

Figure 4–5. SEM images of the obtained (a) entry 1 and (b) entry 2. (c) XRD patterns of the entry 1 (blue line) and entry 2 (red line).

Next, the precursor aqueous solutions with different concentrations of $Ti(O^iPr)_4$ and squaric acid were tested (entries 2–10 in Table 4–1). In the case of a precursor aqueous solutions with 1 : 1 molar ratio of $Ti(O^iPr)_4$ and squaric acid were used (entries 2–5 in Table 4–1), urchin-like nanocrystals (Figure 4–6a) and hexagonal plates (Figure 4–6d) were obtained from low (entry 2 in Table 4–1) and high (entry 5 in Table 4–1) concentrations of the precursor, respectively. At medium concentrations, both of these particles were obtained (entries 3 and 4 in Table 4–1, Figures 4–6b and c). XRD patterns of the obtained hexagonal plates were totally different from the known crystal phases of TiO_2 (Figure 4–6e, purple line). On the other hand, XRD patterns of urchin-like nanocrystals demonstrated the presence of a rutile-type TiO_2 phase (Figure 4–6e, red line). In addition, hexagonal plates were obtained even when using precursor aqueous solutions with 1 : 2 and 1 : 4 molar ratio of $Ti(O^iPr)_4$ and squaric acid (entries 7 and 8 in Table 4–1, Figure 4–7).

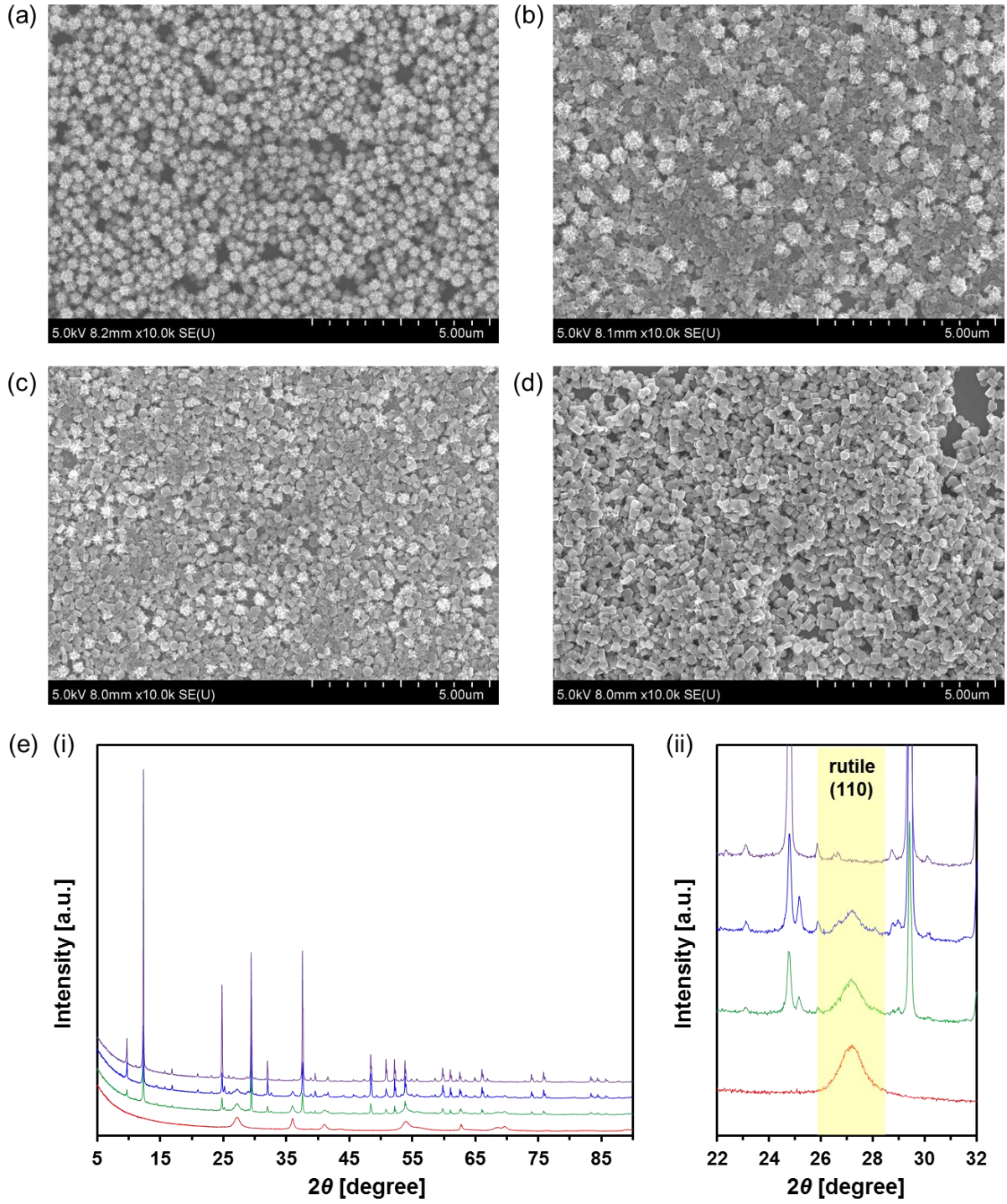

Figure 4–6. SEM images of the obtained (a) entry 2, (b) entry 3, (c) entry 4, and (d) entry 5. (e) XRD patterns of entry 2 (red line), entry 3 (green line), entry 4 (blue line), and entry 5 (purple line). The 2θ range; (i) 5–90 ° and (ii) 22–32 ° (orange, (110) plane of rutile-type TiO_2).

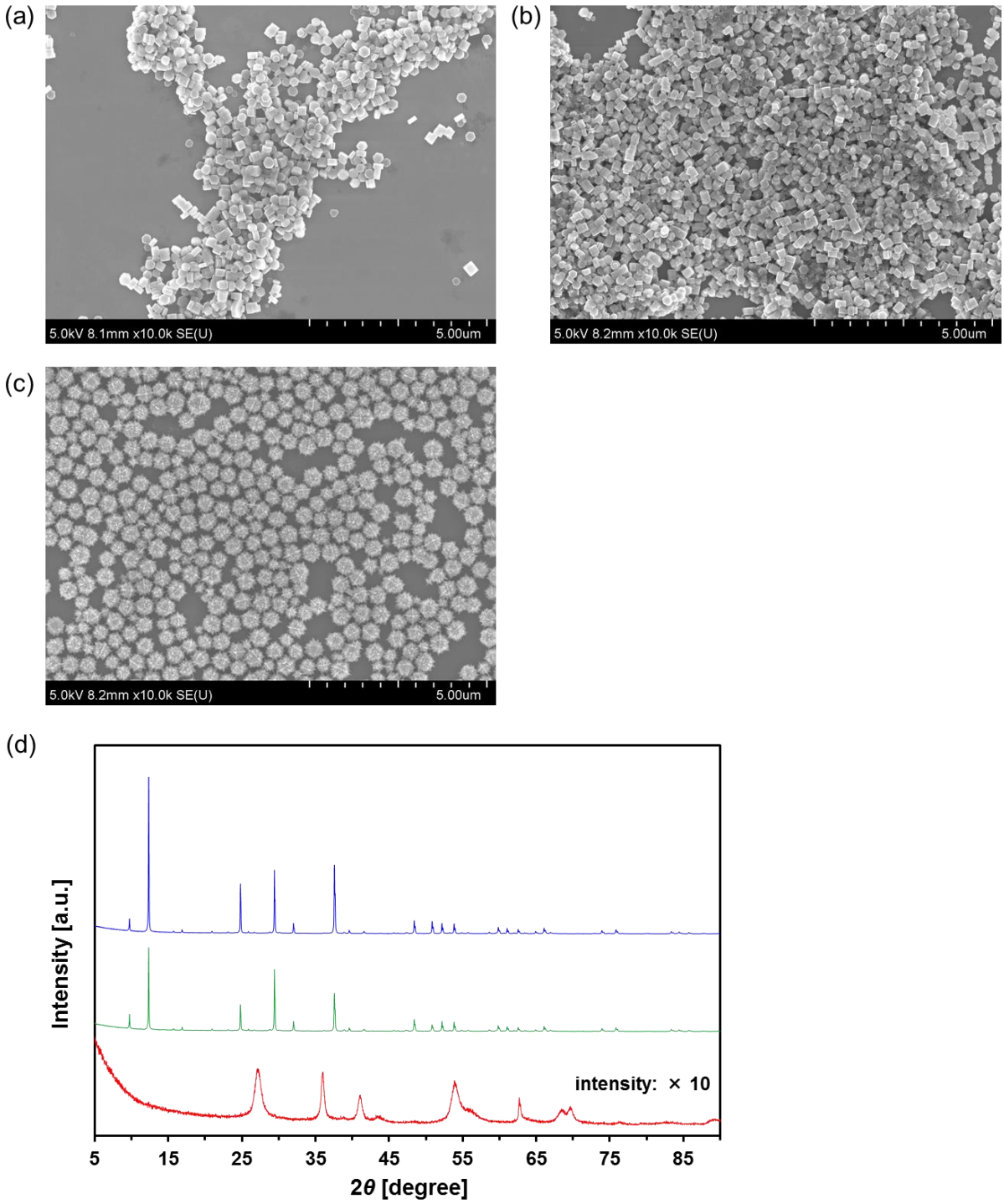

Figure 4–7. SEM images of the obtained (a) entry 6, (b) entry 7, and (c) entry 8. (d) XRD patterns of entry 6 (red line), entry 7 (green line), and entry 8 (blue line).

Heating of a aqueous solution of $Ti(OiPr)_4$ (50 mmol/L) and squaric acid (200 mmol/L) at 120 °C for 72 h afforded hexagonal plates (entry 9 in Table 4–1, Figure 4–8a). The obtained particle diameter and thickness were *ca.* 670 nm and *ca.* 320 nm, respectively. XRD patterns of the obtained hexagonal plates were totally different from the know crystal phases of TiO_2, Ti-based MOF,[25–27] and squarate-based MOF (Figures 4–8b and 4–9).[17,18,28–31] The IR spectra of the hexagonal plates exhibits characteristic bands of the squarate moiety (Figure 4–8c). The peak around 1542 cm^{-1} can likely be assigned to ν(CO)/ν(CC) combination vibrations of the $C_4O_4^{2-}$ ligand.[32–34] In addition, TG analysis of the hexagonal plates demonstrates weight-loss of approximately 40% in the temperature range from 300 to 400 °C, indicating the inclusion of organic materials (Figure 4–8d). These results strongly suggest that the hexagonal plates are a new MOF consisting of titanium ions and squarate ligands.

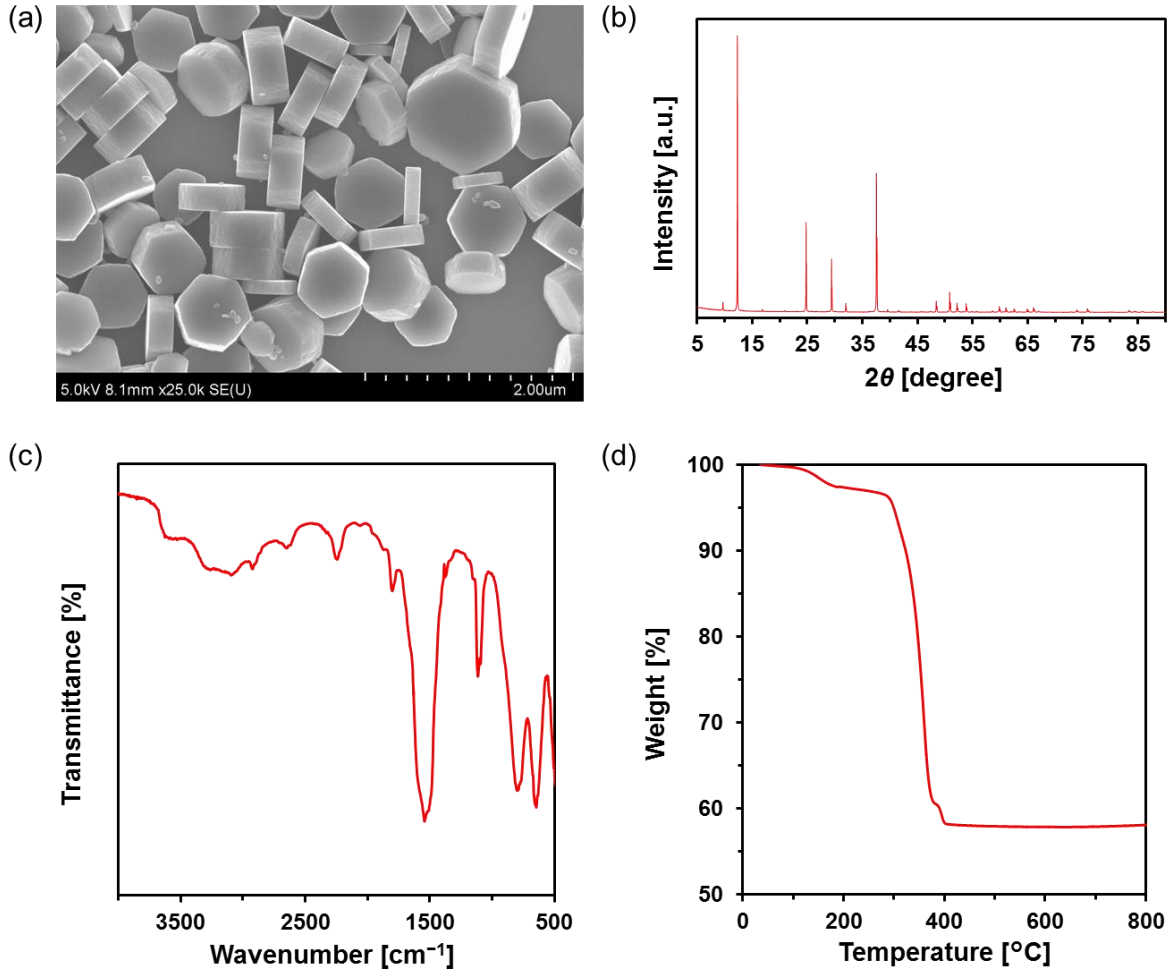

Figure 4–8. (a) SEM image, (b) XRD patterns, (c) FT-IR spectrum, and (d) TG profiles of the obtained hexagonal plates.

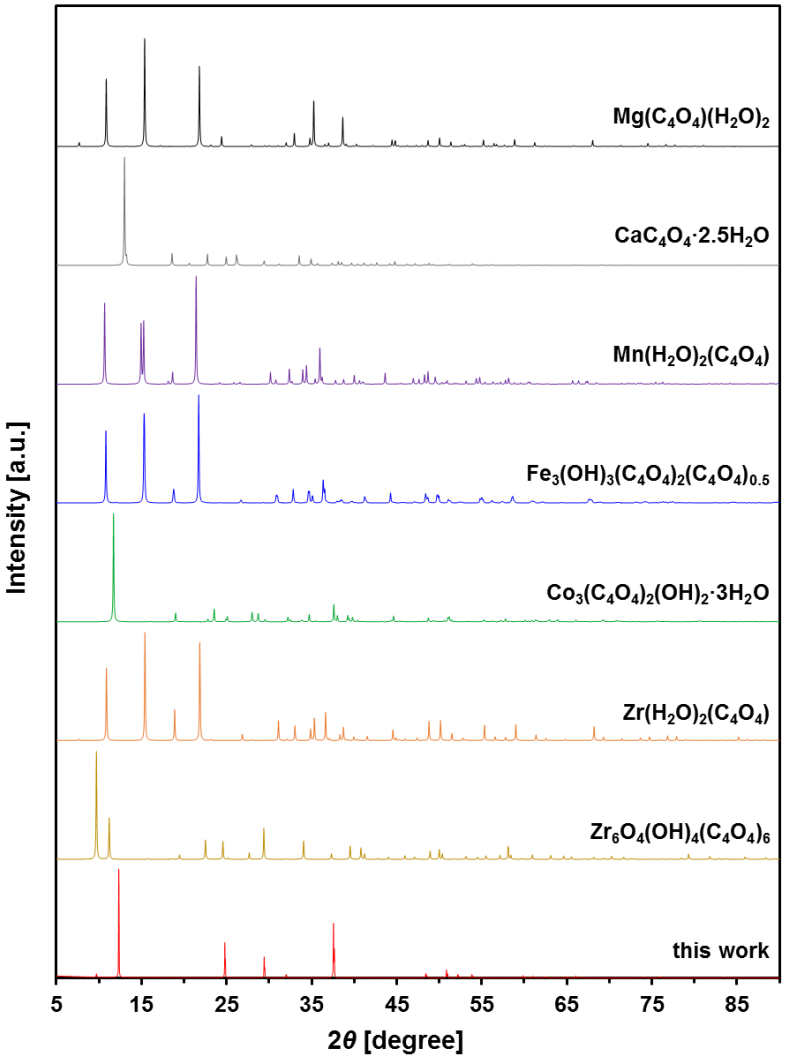

Figure 4–9. XRD patterns of squarate-based MOFs.

To investigate the formation process of the obtained urchin-like TiO_2 nanocrystals, time-dependent experiments were performed. When the heating time of the precursor solution was shortened to 0.5 h, two kinds of colored particles, orange and beige, were obtained (entry 10 in Table 4–1, Figure 4–10a). The two kinds of particles were separated by the difference in sedimentation velocity. The beige particles formed a spherical shapes (Figure 4–10c), but the orange particles did not (Figure 4–10d). The XRD patterns showed that the orange particles were consisted of anatase-type TiO_2 (Figure 4–10b, blue line). Thus, it was found that nanocrystals of anatase-type TiO_2 were also produced at the initial stage of the reaction. When the heating time of the precursor solution was prolonged to 3 h, the particle diameter changed from 230 to 400 nm (Figures 4–11a and b). In addition, the XRD patterns showed that the (002) planes were grown dramatically (Table 4–2, Figures 4–11e). The high-resolution TEM (HR-TEM) image for the obtained urchin-like TiO_2 nanocrystals showed that the crystal lattice distances were 0.25 nm (Figures 4–11d). The plane spacing with a width of 0.25 nm corresponds to the (101) planes and is inclined to the growth direction of <001> at a 57 ° angle approximately.[35] HR-TEM image indicated that the direction of needle growth was along the [001] facet. The urchin-like TiO_2 nanocrystals showed a high specific surface area (94 m^2/g, Figure 4–12).

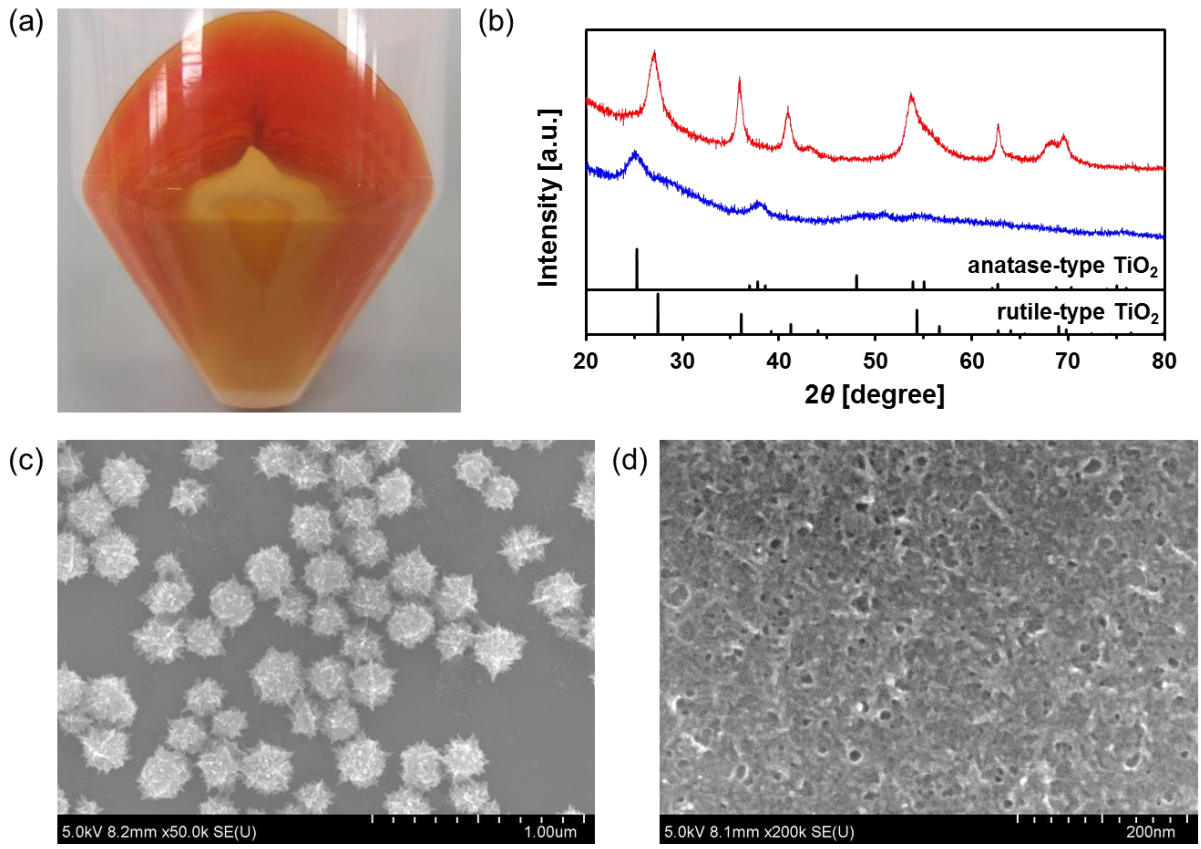

Figure 4–10. (a) Optical image of entry 10. (b) XRD patterns of beige particles (red line) and orange particles (blue line). SEM images of (c) beige particles and (d) orange particles.

Table 4–2. Crystalline size of urchin-like TiO_2 nanocrystals.

Crystal face	Crystalline size[a] [nm]		
	Entry 2	Entry 10	Increased amount
(110)	3.2	8.0	4.8
(101)	14.1	18.2	4.1
(002)	15.3	37.6	22.3

[a] Estimated using the Scherrer equation.

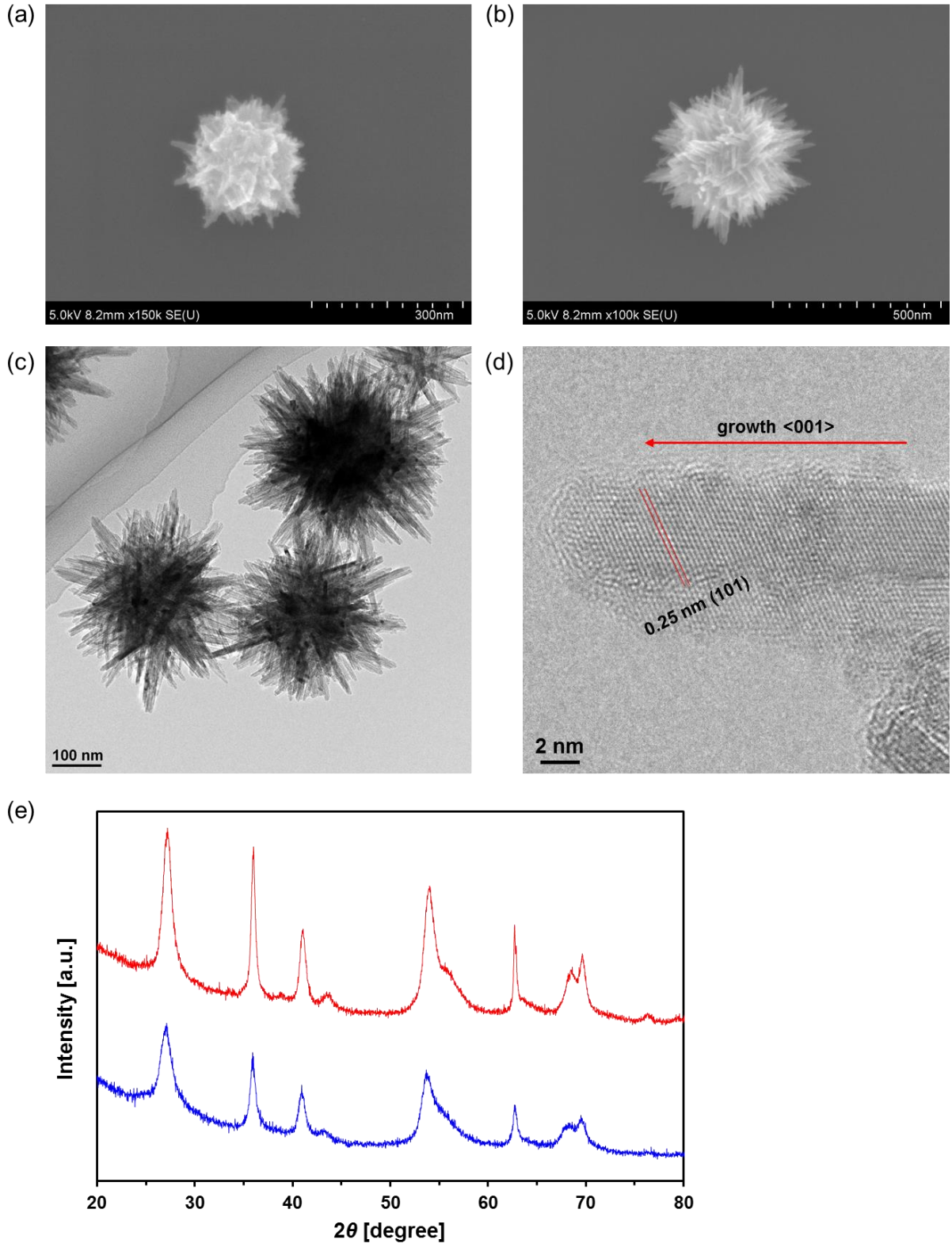

Figure 4–11. SEM images of the obtained (a) entry 10 and (b) entry 2. (c) TEM image and (d) HR-TEM image of entry 2. (e) XRD patterns of entry 2 (red line) and entry 10 (blue line).

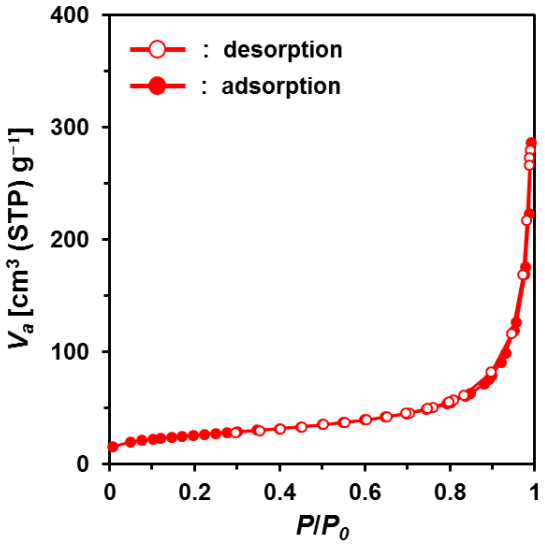

Figure 4–12. Nitrogen adsorption-desorption isotherms of entry 2.

By increasing the molar ration of Ti(O^iPr)$_4$ to squaric acid, particles containing only rutile-type TiO_2 were obtained even when the concentration of the precursor was high. By the use of this procedure, it is possible to obtain over 500 mg of urchin-like TiO_2 nanocrystals in one reaction. Compared to the urchin-like TiO_2 nanocrystals obtained so far (entry 2), the density of needles decreased and the specific surface area increased from 94 to 122 m^2/g (Figure 4–13).

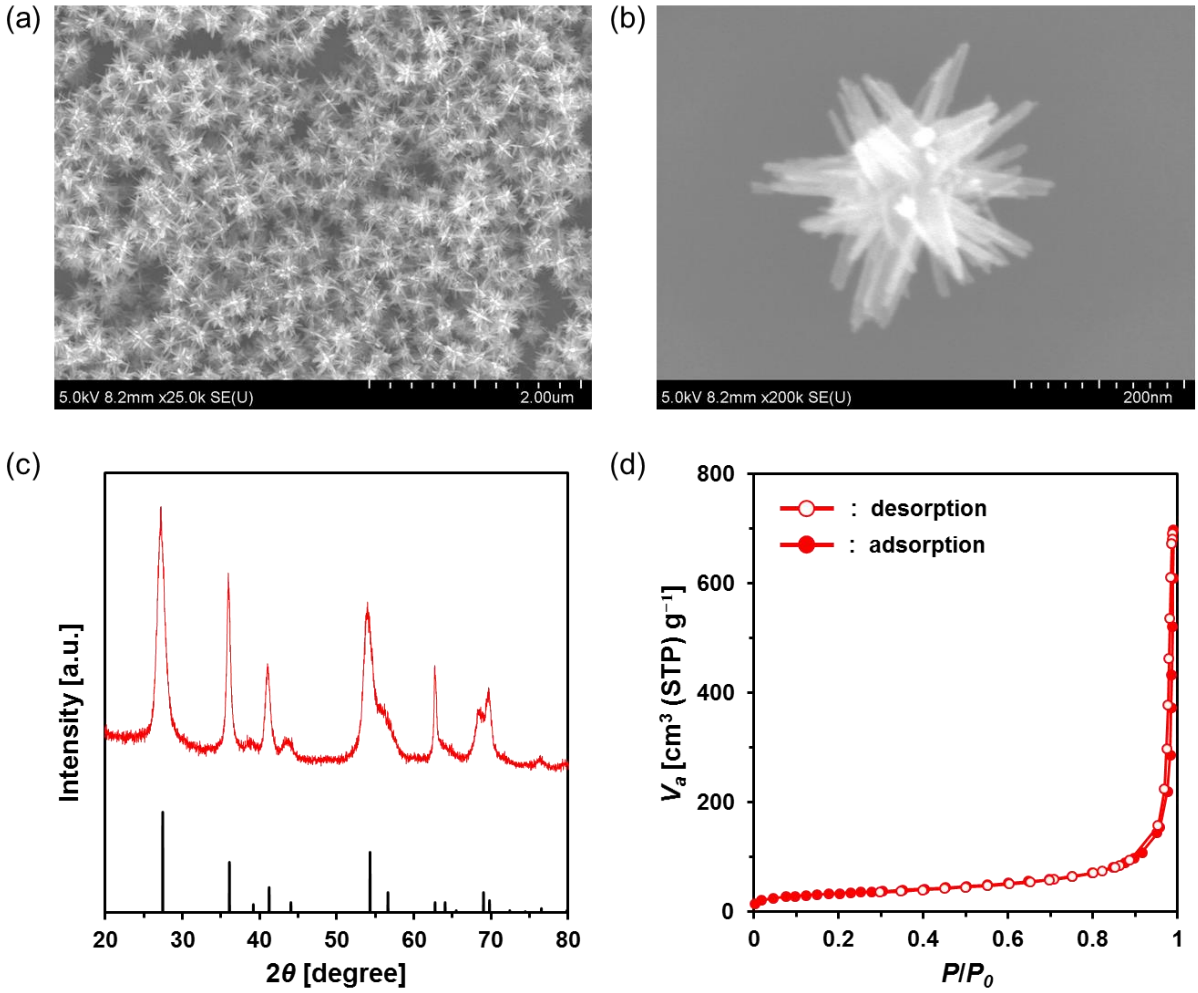

Figure 4–13. SEM images of the obtained urchin-like TiO_2 nanocrystals at (a) low magnification and (b) high magnification. (c) XRD patterns and (d) nitrogen adsorption-desorption isotherms of the obtained urchin-like TiO_2 nanocrystals.

4–3–2. Evaluation of catalytic ability of Ru/TiO_2

CO_2 methanation, so called Sabatier reaction, produces fossilfuel methane from CO_2. CO_2 methanation have attracted much attention as it provides an alternative to renewable electricity storage and is an essential part of the power-to-gas process that promotes industrial decarbonization.[36–39]

$$\mathrm{CO_2 + 4H_2 \rightarrow CH_4 + 4H_2O}, \qquad \Delta H_{298\mathrm{K}} = -165\ \mathrm{kJ/mol}$$

The combination of Ru as a catalytic metal and TiO_2 as a catalytic support is useful as a high activity catalyst for low-temperature methanation reaction.[40–42] Activity of Ru/TiO_2 methanation catalysts strongly depends on its support structure.[43–46] According to the crystallography studies, RuO_2 possesses not only the same crystalline structure to rutile-type TiO_2, but also has a high degree of lattice matching with rutile-type TiO_2 owing to their close lattice parameters. Therefore, strong interaction between RuO_2 and TiO_2 can promote the dispersion of RuO_2 nanoparticles on the TiO_2 support to a great extent and it can prevent aggregation of RuO_2 nanoparticles. Ru/TiO_2 catalysts with Ru amount of 2 wt% were prepared by wet impregnation method using the obtained urchin-like rutile-type TiO_2 nanocrystals (Ru/u-TiO_2, Figure 4–14). Actually CO_2 methanation using Ru/u-TiO_2 as a catalyst showed better performance than the reference standard catalyst, Ru/JRC-TIO-16 (Figure 4–15). The activation energies of the catalysts were obtained by scanning the catalytic activities from 100 to 200 °C, and were found to be 61.9 and 61.3 kJ/mol, for Ru/u-TiO_2 and Ru/JRC-TIO-16, respectively (Figure 4–16). Similar values of activation energies between Ru/u-TiO_2 and Ru/JRC-TIO-16 are found suggests that the active species are the same in all the catalysts. The higher catalytic activity of Ru/u-TiO_2 compared to Ru/JRC-TIO-16 can therefore be attributed to a greater number of active sites. To obtain direct evidence for Ru dispersion on the TiO_2 supports, quantitative evaluation was performed by CO-pulse experiment (Figure 4–17). The

Ru dispersion of Ru/u-TiO_2 and Ru/JRC-TIO-16 were 11.8% and 3.0%, respectively. Thus, Ru/u-TiO_2 obtained by hydrothermal synthesis using squaric acid resulted in highly efficient dispersion of Ru and acceleration of the CO_2 methanation. In addition, by increasing the amount of Ru supported to 5 wt%, the CH_4 yield of CO_2 methanation at 200 °C using Ru/u-TiO_2 was approximately twice (Figure 4–18).

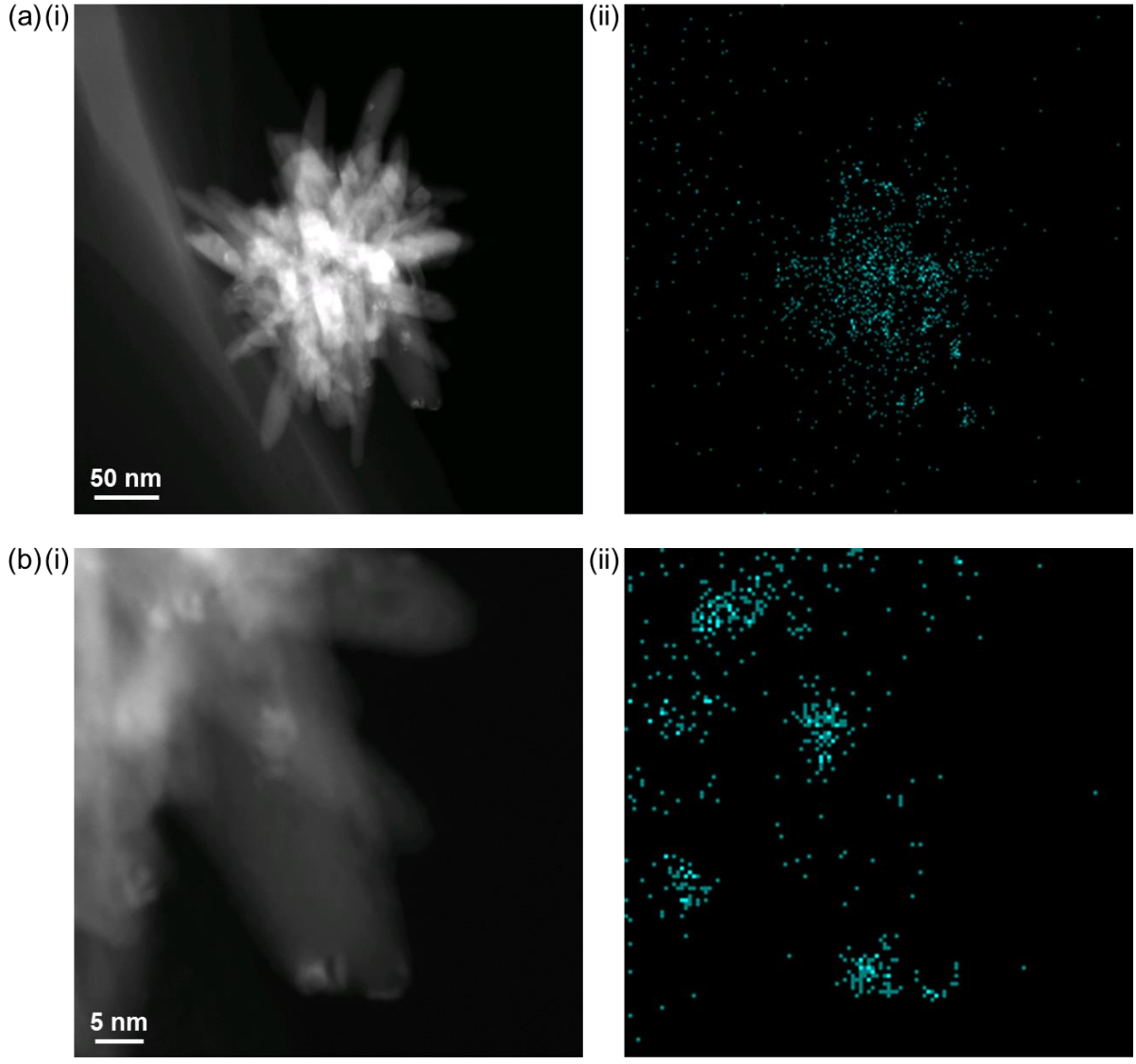

Figure 4–14. HAADF-STEM/EDX analysis of the prepared Ru/u-TiO_2 at (a) low magnification and (b) high magnification; (i) HAADF-STEM image and (ii) Ru mapping image.

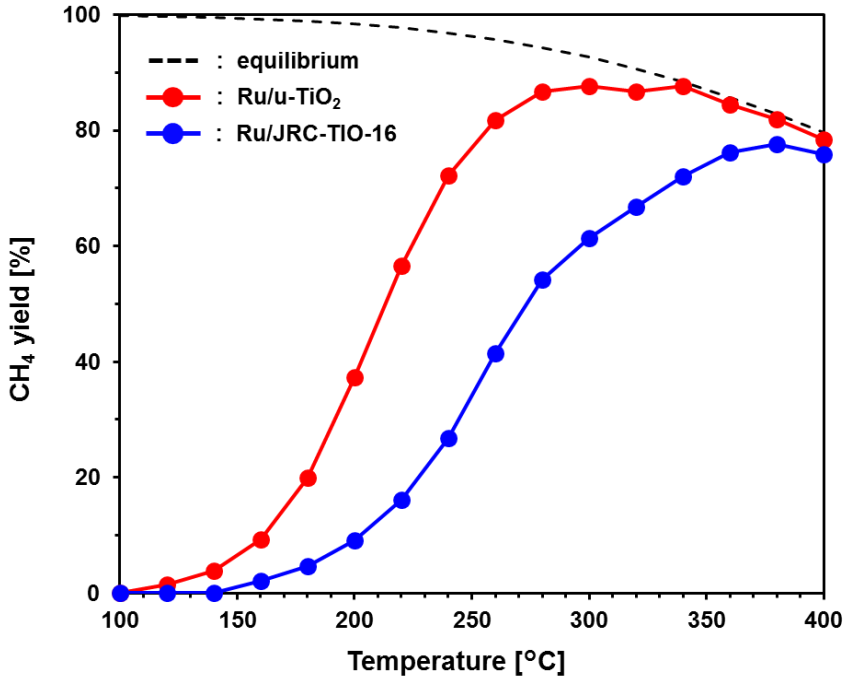

Figure 4–15. CH_4 yield obtained at different reaction temperature of CO_2 methanation using Ru/u-TiO_2 (red line) and Ru/JRC-TIO-16 (blue line).

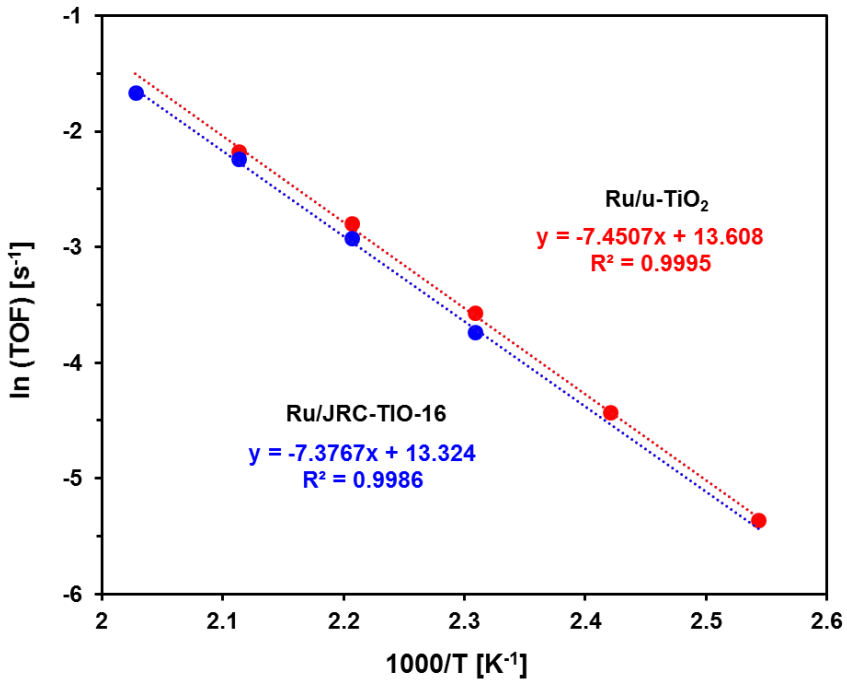

Figure 4–16. Arrhenius plots of CO_2 methanation using Ru/u-TiO_2 (red line) and Ru/JRC-TIO-16 (blue line).

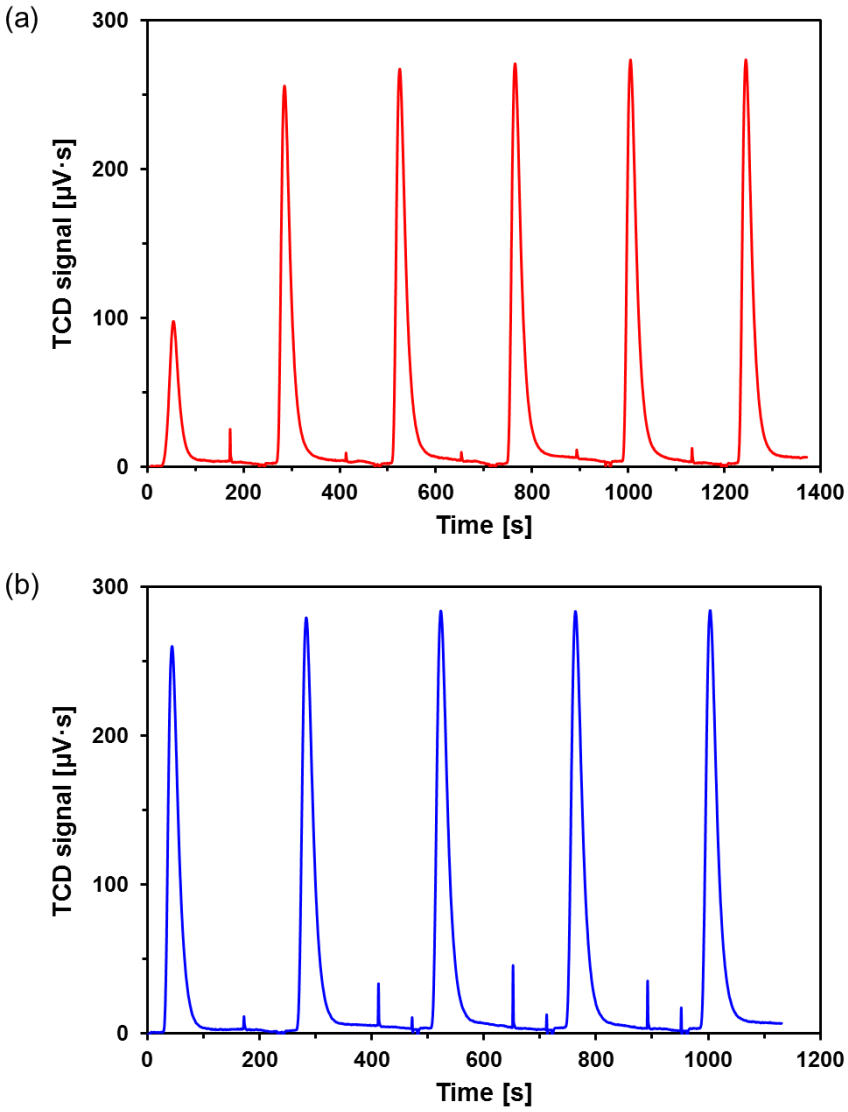

Figure 4–17. CO chemical adsorptions of (a) Ru/u-TiO_2 and (b) Ru/JRC-TIO-16.

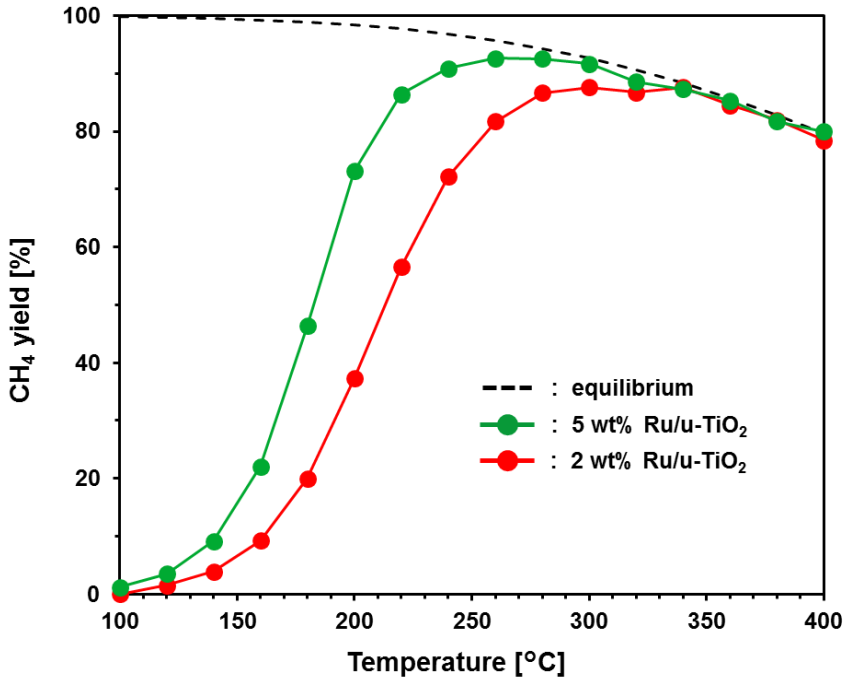

Figure 4–18. CH_4 yield obtained at different reaction temperature of CO_2 methanation using 5 wt% Ru/u-TiO_2 (green line) and 2 wt% Ru/u-TiO_2 (red line).

4–4. Conclusions

A new Ti-based nanocrystals were successfully synthesized by a hydrothermal reaction from $Ti(O^iPr)_4$ and squaric acid in water at 150 °C. The crystal structure of the product can be tuned by adjusting the concentration of squaric acid. In particular, the obtained urchin-like rutile-type TiO_2 nanocrystals showed a high specific surface area. The use of Ru/TiO_2 catalyst prepared from the urchin-like rutile-type TiO_2 nanocrystals afforded higher activity in CO_2 methanation reaction than that of the reference standard catalyst.

References

1. Ding, Y.; Yang, I. S.; Li, Z.; Xia, X.; Lee, W. I.; Dai, S.; Bahnemann, D. W.; Pan, J. H. Nanoporous TiO_2 spheres with tailored textural properties: controllable synthesis, formation mechanism, and photochemical applications. *Prog. Mater. Sci.* **2020**, *109*, 100620.
2. Zu, M.; Zhou, X.; Zhang, S.; Qian, S.; Li, D.-S.; Liu, X.; Zhang, S. Sustainable engineering of TiO_2-based advanced oxidation technologies: from photocatalyst to application devices. *J. Mater. Sci. Technol.* **2021**, *78*, 202–222.
3. Zhang, H.; Banfield, J. F. Structural characteristics and mechanical and thermodynamic properties of nanocrystalline TiO_2. *Chem. Rev.* **2014**, *114*, 9613–9644.
4. Huang, W. Oxide nanocrystal model catalysts. *Acc. Chem. Res.* **2016**, *49*, 520–527.
5. Chen, S.; Xiong, F.; Huang, W. Surface chemistry and catalysis of oxide model catalysts from single crystals to nanocrystals. *Surf. Sci. Rep.* **2019**, *74*, 100471.
6. Li, L.; Yan, J.; Wang, T.; Zhao, Z.-J.; Zhang, J.; Gong, J.; Guan, N. Sub-10 nm rutile titanium dioxide nanoparticles for efficient visible-light-driven photocatalytic hydrogen production. *Nat. Commun.* **2015**, *6*, 5881.
7. Manseki, K.; Saka, K.; Matsui, M.; Vafaei, S.; Sugiura T. Structure identification of Ti(IV) clusters in low temperature TiO_2 crystallization: creating high-surface area brush-shaped rutile TiO_2. *CrystEngComm* **2017**, *19*, 5844–5848.
8. Beyer, J.; Mamakhel, A.; Søndergaard-Pedersen, F.; Yu, J.; Iversen, B.B. Continuous flow hydrothermal synthesis of phase pure rutile TiO_2 nanoparticles with a rod-like morphology. *Nanoscale* **2020**, *12*, 2695–2702.
9. Kinsinger, N. M.; Wong, A.; Li, D.; Villalobos, F.; Kisailus, D. Nucleation and crystal growth of nanocrystalline anatase and rutile phase TiO_2 from a water-soluble precursor.

Cryst. Growth Des. **2010**, *10*, 5254–5261.

10. Tomita, K.; Petrykin, V.; Kobayashi, M.; Shiro, M.; Yoshimura, M.; Kakihana, M. A water-soluble titanium complex for the selective synthesis of nanocrystalline brookite, rutile, and anatase by a hydrothermal method. *Angew. Chem., Int. Ed.* **2006**, *45*, 2378–2381.
11. Yamazaki, Y.; Fujitsuka, M.; Yamazaki, S. Effect of organic additives during hydrothermal syntheses of rutile TiO_2 nanorods for photocatalytic applications. *ACS Appl. Nano Mater.* **2019**, *2*, 5890–5899.
12. Schwartz, L. M.; Howard, L. O. Conductance study of squaric acid aqueous dissociation. *J. Phys. Chem.* **1971**, *75*, 1798–1803.
13. Ghosh, A. K.; Ghoshal, D.; Zangrando, E.; Ribas, J.; Chaudhuri, N. R. Structural diversity in manganese squarate frameworks using N,N-donor chelating/bridging ligands: syntheses, crystal structures and magnetic properties. *Dalton Trans.* **2006**, 1554–1563.
14. Storer, R. I.; Aciro, C.; Jones, L. H. Squaramides: physical properties, synthesis and applications. *Chem. Soc. Rev.* **2011**, *40*, 2330–2346.
15. He, J.; Jo, Y. J.; Sun, X.; Qiao, W.; Ok, J.; Kim, T.; Li, Z. Squaraine dyes for photovoltaic and biomedical applications. *Adv. Funct. Mater.* **2020**, 2008201.
16. Chasak, J.; Slachtova, V.; Urban, M.; Brulikova, L. Squaric acid analogues in medicinal chemistry. *Eur. J. Med. Chem.* **2021**, *209*, 112872.
17. Goswami, S.; Adhikary, A.; Jena, H. S.; Biswas, S.; Konar, S. A 3D Iron (II)-based MOF with squashed cuboctahedral nanoscopic cages showing spin-canted long-range antiferromagnetic ordering. *Inorg. Chem.* **2013**, *52*, 12064–12069.
18. Bueken, B.; Reinsch, H.; Reimer, N.; Stassen, I.; Vermoortele, F.; Ameloot, R.; Stock, N.; Kirschhock, C.; De Vos, D. A zirconium squarate metal-organic framework with modulator-dependent molecular sieving properties. *Chem. Commun.* **2014**, *50*, 10055–10058.

19. Lin, R. B.; Li, L.; Zhou, H. L.; Wu, H.; He, C.; Li, S.; Krishna, R.; Li, J.; Zhou, W.; Chen, B. Molecular sieving of ethylene from ethane using a rigid metal-organic framework. *Nat. Mater.* **2018**, *17*, 1128–1133.
20. Li, L.; Guo, L.; Zhang, Z.; Yang, Q.; Yang, Y.; Bao, Z.; Ren, Q.; Li, J. A robust squarate-based metal–organic framework demonstrates record-high affinity and selectivity for xenon over krypton. *J. Am. Chem. Soc.* **2019**, *141*, 9358–9364.
21. Liu, Z.; Li, Q.; Wang, Y.; Ma, R.; Sun, J.; Deng, J.; Chen, J.; Sun, D.; Xing, X. Facile synthesis of dicelike cobalt squarate cages through a spontaneous sissolution–regrowth process. *Chem. Mater.* **2020**, *32*, 6765–6771.
22. McBride, B. J.; Gordon, S. *Computer program for calculation of complex chemical equilibrium compositions and applications II. User's manual and program description*; Report Number: NASA RP-1311-P2; National Aeronautics and Space Administration, Lewis Research Center: Cleveland, Ohio, 1996.
23. Guo, Y.; Mei, S.; Yuan, K.; Wang, D.-J.; Liu, H.-C.; Yan, C.-H.; Zhang, Y.-W. Low-temperature CO_2 methanation over CeO_2-supported Ru single atoms, nanoclusters, and nanoparticles competitively tuned by strong metal–support interactions and H-spillover effect. *ACS Catal.* **2018**, *8*, 6203–6215.
24. Santos, P. S.; Sala, O.; Noda, L. K.; Gonçalves, N. S. Evidences for a localized chromophore in the Ti(IV)/squarate complex: a resonance Raman investigation. *Spectrochim. Acta A* **2000**, *56*, 1553–1562.
25. Assi, H.; Mouchaham, G.; Steunou, N.; Devic, T.; Serre, C. Titanium coordination compounds: from discrete metal complexes to metal-organic frameworks. *Chem. Soc. Rev.* **2017**, *46*, 3431–3452.
26. Nguyen, H. L. The Chemistry of titanium-based metal-organic frameworks. *New J. Chem.* **2017**, *41*, 14030–14043.

27. Yan, Y.; Li, C.; Wu, Y.; Gao, J.; Zhang, Q. From isolated Ti-oxo clusters to infinite Ti-oxo chains and sheets: recent advances in photoactive Ti-based MOFs. *J. Mater. Chem. A* **2020**, *8*, 15245–15270.

28. Robl, C.; Weiss, A. Alkaline-earth squarates III. $CaC_4O_4 \cdot 2.5H_2O$, a novel polymer complex with zeolitic properties (1). *Mater. Res. Bull.* **1987**, *22*, 373–380.

29. Gutschke, S. O. H.; Molinier, M.; Powell, A. K.; Wood, P. T. Hydrothermal synthesis of microporous transition metal squarates: preparation and structure of $[CO_3(\mu_3\text{-}OH)_2(C_4O_4)_2] \cdot 3H_2O$. *Angew. Chem., Int. Ed. Engl.* **1997**, *36*, 991–992.

30. Neeraj, S.; Noy, M. L.; Rao, C. N. R.; Cheetham, A. K. Sodalite networks formed by metal squarates. *Solid State Sci.* **2002**, *4*, 1231–1236.

31. Lin, X. Y.; Zhao, L. M.; Wang, D. H.; Wang, Y. K.; Li, M.; Li, H. H.; Chen, Z. R. Structural diversities of squarate-based cComplexes: photocurrent responses and thermochromic behaviours enchanced by viologens. *Inorg. Chem. Front.* **2018**, *5*, 189–199.

32. Ito, M.; West, R. New aromatic anions. IV. Vibrational spectra and force constants for $C_4O_4^{-2}$ and $C_5O_5^{-2}$. *J. Am. Chem. Soc.* **1963**, *85*, 2580–2584.

33. Corrêa, C. C.; Diniz, R.; Chagas, L. H.; Rodrigues, B. L.; Yoshida, M. I.; Teles, W. M.; Machado, F. C.; Edwards, H. G.; de Oliveira, L. F. C. Synthesis, vibrational spectroscopy and crystal structures of polymers involving transition metals with squarate ions and 1,3-bis(4-pyridyl)propane. *Vibr. Spectrosc.* **2007**, *45*, 82–88.

34. Liebing, P.; Husien, A. A.; Fischer, A.; Nietzschmann, E.; Edelmann F. T. Macromolecular self-assembly of organotin(IV) squarates and croconates–preparation and crystal structures of $[SnMe_2(H_2O)_2]C_4O_4$, $[SnMe_3]_2C_4O_4$, and $[SnMe_3(H_2O)]_2C_5O_5$. *Z. Anorg. Allg. Chem.* **2017**, *643*, 536–543.

35. Tian, Y.; Zhang, J.; Ma, J. C.; Jia, X. Monodisperse rutile microspheres with ultrasmall nanorods on surfaces: synthesis, characterization, luminescence, and photocatalysis. *J.*

Colloid Interface Sci. **2012**, *385*, 1–7.

36. Li, W.; Wang, H.; Jiang, X.; Zhu, J.; Liu, Z.; Guo, X.; Song, C. A short review of recent advances in CO_2 hydrogenation to hydrocarbons over heterogeneous catalysts. *RSC Adv.* **2018**, *8*, 7651–7669.
37. Mota, F. M.; Kim, D. H. From CO_2 methanation to ambitious long-chain hydrocarbons: alternative fuels paving the path to sustainability. *Chem. Soc. Rev.* **2019**, *48*, 205–259.
38. Ashok, J.; Pati, S.; Hongmanorom, P.; Tianxi, Z.; Junmei, C.; Kawi, S. A review of recent catalyst advances in CO_2 methanation processes. *Catal. Today* **2020**, *356*, 471–489.
39. Wang, Y.; Winter, L. R.; Chen, J. G.; Yan, B. CO_2 hydrogenation over heterogeneous catalysts at atmospheric pressure: from electronic properties to product selectivity. *Green Chem.* **2021**, *23*, 249–267.
40. Abe, T.; Tanizawa, M.; Watanabe, K.; Taguchi, A. CO_2 methanation property of Ru nanoparticle-loaded TiO_2 prepared by a polygonal barrel-sputtering method. *Energy Environ. Sci.* **2009**, *2*, 315–321.
41. Inoue, M.; Miyazaki, K.; Lu, B.; Song, C.; Honda, Y.; Arao, M.; Ohwaki, T.; Matsumoto, M.; Imai, H.; Shima, A.; Sone, Y.; Peng, R. C.; Shibayanagi, T.; Abe, T. Structure-sensitivity factors based on highly active CO_2 methanation catalysts prepared via the polygonal barrel-sputtering method. *J. Phys. Chem. C* **2020**, *124*, 10016–10025.
42. Lee, W.J.; Li, C.; Prajitno, H.; Yoo, J.; Patel, J.; Yang, Y.; Lim, S. Recent trend in thermal catalytic low temperature CO_2 methanation: a critical review. *Catal. Today* **2020** in press.
43. Lin, Q.; Liu, X.; Jiang, Y.; Wang, Y.; Huang, Y.; Zhang, T. Crystal phase effects on the structure and performance of ruthenium nanoparticles for CO_2 hydrogenation. *Catal. Sci. Technol.* **2014**, *4*, 2058–2063.
44. Kim, A.; Sanchez, C.; Patriarche, G.; Ersen, O.; Moldovan, S.; Wisnet, A.; Sassoye, C.; Debecker, D. P. Selective CO_2 methanation on Ru/TiO_2 catalysts: Unravelling the decisive

role of the TiO_2 support crystal structure. *Catal. Sci. Technol.* **2016**, *6*, 8117–8128.

45. Kim, A.; Debecker, D. P.; Devred, F.; Dubois, V.; Sanchez, C.; Sassoye, C. CO_2 methanation on Ru/TiO_2 catalysts: on the effect of mixing anatase and rutile TiO_2 supports. *Appl. Catal., B* **2018**, *220*, 615–625.
46. Wang, D.; Huang, J.; Liu, F.; Xu, X.; Fang, X.; Liu, J.; Xie, Y.; Wang, X. Rutile RuO_2 dispersion on rutile and anatase TiO_2 supports: the effects of support crystalline phase structure on the dispersion behaviors of the supported metal oxides. *Catal. Today* **2020**, *339*, 220–232.

Conclusions

In conclusion, I have developed a new synthetic method of porous nanomaterials with precisely controlled crystal structure by solvothermal/hydrothermal reaction. Submicron-sized Nb_2O_5 porous spheres with a high specific surface area and nano concave–convex surfaces were synthesized *via* a rapid one-pot single-step alcothermal reaction. A similar alcothermal reaction yielded TiO_2–Nb_2O_5 composite porous spheres, whose Ti : Nb molar ratio was controlled by changing the precursor solution component ratios. A two-step synthetic approach for the generation of $TiNb_2O_7$ porous spheres was developed *via* an alcothermal treatment followed by simple calcination. Ultrafine TiO_2 nanocrystals were synthesized by rapid heating solvothermal method using liquid mixtures of titanium alkoxide and oleic acid as precursor solutions. Also, ultrafine TiO_2 nanocrystals were easily converted into porous TiO_2 thin layer transparent film through drop-casting and calcination process. Hydrothermal synthesis of urchin-like TiO_2 nanocrystals with rutile crystal phase was studied using squaric acid. Ru/u-TiO_2 obtained by hydrothermal synthesis using squaric acid resulted in highly efficient dispersion of Ru and acceleration of CO_2 methanation reaction.

List of Publications, Presentations, and Awards

Publications

1. Porous niobia spheres with large surface area: alcothermal synthesis and controlling of their composition and phase transition behaviour

   Yoshitaka Kumabe, Hitomi Taga, Kai Kan, Masataka Ohtani, Kazuya Kobiro

   RSC Adv. **2020**, *10*, 14630–14636.

2. Rapid one-pot synthesis of ultrafine titania nanocrystals and their conversion into transparent mesoporous thin layer films

   Yoshitaka Kumabe, Masataka Ohtani, Kazuya Kobiro

   Microporous and Mesoporous Mater. **2018**, *261*, 207–213.

3. Ce^{3+} -enriched spherical porous ceria with an enhanced oxygen storage capacity.

   Ayano Taniguchi, Yoshitaka Kumabe, Kai Kan, Masataka Ohtani, Kazuya Kobiro

   RSC Adv. **2021**, *11*, 5609–5617.

4. Controllable synthesis of MoS_2/graphene low-dimensional nanocomposites and their electrical properties

   Le Ngoc Long, Pham Tan Thi, Pham Trung Kien, Pham Thanh Trung, Masataka Ohtani, Yoshitaka Kumabe, Hirofumi Tanaka, Shigenori Ueda, Hyoyoung Lee, Phan Bach Thang, Tran Van Khai

   Appl. Surf. Sci. **2020**, *504*, 144193.

5. Highly durable Ru catalysts supported on CeO_2 nanocomposites for CO_2 methanation

   Hien Thi Thu Nguyen, Yoshitaka Kumabe, Shigenori Ueda, Masataka Ohtani, Kazuya Kobiro

   Appl. Catal., A **2019**, *577*, 35–43.

Published books

1. Masataka Ohtani, Yoshitaka Kumabe, Kai Kan, and Kazuya Kobiro、「ナノ凹凸多孔体の一段階大量合成と耐熱触媒担体への応用」、『Chemical engineering』、化学工学社、VOL. 64、NO. 5、pp.319–325、2019

Presentations in international conferences

1. Yoshitaka Kumabe, Masataka Ohtani, and Kazuya Kobiro、「Size and Crystal System Controlled Synthesis of Metal Oxide Nanoparticles via Solvothermal Reaction」、『6th International Solvothermal and Hydrothermal Association Conference』、Miyagi, Japan、August 2018、Oral Presentation.
2. Yoshitaka Kumabe, Masataka Ohtani, and Kazuya Kobiro、「Synthesis of Nb_2O_5 Nanoparticles with Different Morphology and Crystal Structures using Solvothermal Reaction」、『6th International Solvothermal and Hydrothermal Association Conference』、Miyagi, Japan、August 2018、Poster Presentation.
3. Yoshitaka Kumabe, Masataka Ohtani, and Kazuya Kobiro、「Effect of Acid Additives on Methanol Solvothermal Reaction of Titanium Tetraalkoxide」、『The 10th International Conference on Supercritical Fluids Supergreen 2017』、Aichi, Japan、December 2017、Poster Presentation.
4. Yoshitaka Kumabe, Masataka Ohtani, and Kazuya Kobiro、「Synthesis of Titania Nanocrystals with Sub-5 nm Size and Conversion into Porous Thin Layer Transparent Films」、『The 6th International Symposium on Frontier Technology』、Kochi, Japan、November 2017、Oral Presentation.

5. Yoshitaka Kumabe, Masataka Ohtani, and Kazuya Kobiro、「Rapid One-pot Synthesis of Titania Nanocrystals with Sub-5 nm Size」、『The 17th Congress of Asian Pacific Confederation of Chemical Engineering』、Hong Kong、August 2017、Oral Presentation.

Presentations in domestic conferences/symposiums

1. Yoshitaka Kumabe, Kai Kan, Masataka Ohtani, and Kazuya Kobiro、「Selective synthesis of Ti-based nanocrystals using squaric acid」、『SCEJ 85th Annual Meeting』、Osaka、March 2020、Poster Presentation.
2. Yoshitaka Kumabe, Kai Kan, Masataka Ohtani, and Kazuya Kobiro、「高表面積ウニ状 TiO_2 の生成メカニズム」、『Nanotechnology Symposium 2019』、Kochi、December 2019、Poster Presentation.
3. Yoshitaka Kumabe, Kai Kan, Masataka Ohtani, and Kazuya Kobiro、「スクアリン酸と難水溶性金属原料を用いた均一形状ナノ粒子の水熱合成」、『9th CSJ Chemistry Festa』、Tokyo、October 2019、Oral and Poster Presentation.
4. Yoshitaka Kumabe, Kai Kan, Masataka Ohtani, and Kazuya Kobiro、「スクアリン酸を用いた Ti 系ナノ結晶材料のワンポット水熱合成」、『Kochi Chemistry Symposium 2019』、Kochi、October 2019、Poster Presentation.
5. Yoshitaka Kumabe, Kai Kan, Masataka Ohtani, and Kazuya Kobiro、「One-pot alcothermal synthesis of spherical porous TiO_2–Nb_2O_5 composites —morphology and property control by elemental composition—」、『The 99th CSJ Annual Meeting』、Kobe、March 2019、Oral Presentation.
6. Yoshitaka Kumabe, Kai Kan, Masataka Ohtani, and Kazuya Kobiro、「One-pot alcothermal synthesis of TiO_2–Nb_2O_5 composite spherical porous nanomaterials producing solid or

hollow morphology」、『SCEJ 84th Annual Meeting』、Tokyo、March 2019、Poster Presentation.

7. Yoshitaka Kumabe, Kai Kan, Masataka Ohtani, and Kazuya Kobiro、「ニオブ系複合ナノ粒子多孔体の簡便な合成法の開発」、『Nanotechnology Symposium 2018』、Kochi、November 2018、Poster Presentation.
8. Yoshitaka Kumabe, Kai Kan, Masataka Ohtani, and Kazuya Kobiro、「スニオブ系金属酸化物球状ナノ粒子多孔体のソルボサーマル合成」、『Kochi Chemistry Symposium 2018』、Kochi、October 2018、Poster Presentation.
9. Yoshitaka Kumabe, Masataka Ohtani, and Kazuya Kobiro、「Rapid heating solvothermal synthesis of ultrafine nanoparticles and formation of their porous thin layer films」、『The 98th CSJ Annual Meeting』、Chiba、March 2018、Poster Presentation.
10. Yoshitaka Kumabe, Masataka Ohtani, and Kazuya Kobiro、「透明 TiO_2 薄膜調製のための極小ナノ粒子ワンポット合成」、『Nanotechnology Symposium 2017』、Kochi、November 2017、Poster Presentation.
11. Yoshitaka Kumabe, Masataka Ohtani, and Kazuya Kobiro、「スクアリン酸-チタンナノ構造体の合成とその光触媒活性の評価」、『The 5th Kochi University and Kochi University of Technology Joint Seminar』、Kochi、June 2017、Oral Presentation.
12. Yoshitaka Kumabe, Masataka Ohtani, and Kazuya Kobiro、「極小酸化チタンナノロッドを用いた透明半導体薄膜の形成」、『Nanotechnology Symposium 2016』、Kochi、November 2016、Poster Presentation.
13. Yoshitaka Kumabe, Masataka Ohtani, and Kazuya Kobiro、「High-temperature and High-pressure Synthesis of Extremely Small Titanium Dioxide Nanorods using Unsaturated Fatty Acids」、『SCEJ 48th Autumn Meeting』、Tokushima、September 2016、Oral Presentation.
14. Yoshitaka Kumabe, Masataka Ohtani, and Kazuya Kobiro、「極小酸化チタンナノロッ

ドの合成と薄膜形成」、『The 29th Workshop of the chemical society of Kochi』、Kochi、August 2016、Poster Presentation.

Awards

1. Poster Award、Kochi Chemistry Symposium 2019 (2019)
2. ISHA 2018 Graduate Student Awards、6th International Solvothermal and Hydrothermal Association Conference (2018)
3. Branch Director Prize、The Chugoku-Shikoku Branch of the Chemical Society of Japan for Fiscal Year 2017 (2018)
4. Student Award、SCEJ 48th Autumn Meeting (2016)

Acknowledgements

It is with immense gratitude that I acknowledge the support and help of all those who have been beside me during doctor course.

I would to express the deepest appreciation to my academic supervisor, Professor Kazuya Kobiro, for constant guidance, helpful comments and warm encouragement throughout my course. This dissertation could not have been completed without my academic advisor.

I would also be grateful to Professor Nagatoshi Nishiwaki, Associate Professor Masataka Ohtani, Assistant Professor Akito Ito, Professor Hisao Makino, and Assistant Professor Kai Kan. Thank you very much for the valuable comments and suggestions on my researches. In particular, I would like to express my sincere gratitude to Associate Professor Masataka Ohtani and Assistant Professor Akito Ito for teaching me many experimental skills and for useful advices.

I would like to offer my special thanks to other members of research group of Professor Kazuya Kobiro and Associate Professor Masataka Ohtani for their cooperation and academic support.

I wish to thank all IRC staff members for helping my school life support.

Most of all, I would like to express my deepest gratitude to my family who always pay attention to me all the times, I could not have a chance to do what I am doing without them. The most success of the graduation is devoted to my family.